ulm university universität ulm

Annual Report 2013

Institute of Optoelectronics

Cover photo:
Scanning electron micrograph (courtesy of T. Aschenbrenner et al., Univ. of Bremen) of position-controlled GaN nanotubes with coaxial GaInN quantum wells on their side facets. The structures are realized using ZnO nanopillars as sacrificial templates. Single ZnO nanowires are grown on top of GaN pyramids using chemical vapor deposition (CVD). Subsequently, the structures are transferred to our metal organic vapor phase epitaxy (MOVPE) reactor and overgrown with coaxial Ga(In)N heterostructures. The ZnO nanowires are etched during this process and allow the fabrication of GaN tubes with inner diameters of some hundred nanometers and integrated coaxial InGaN quantum wells.

Contents

Articles

Lists of Publications

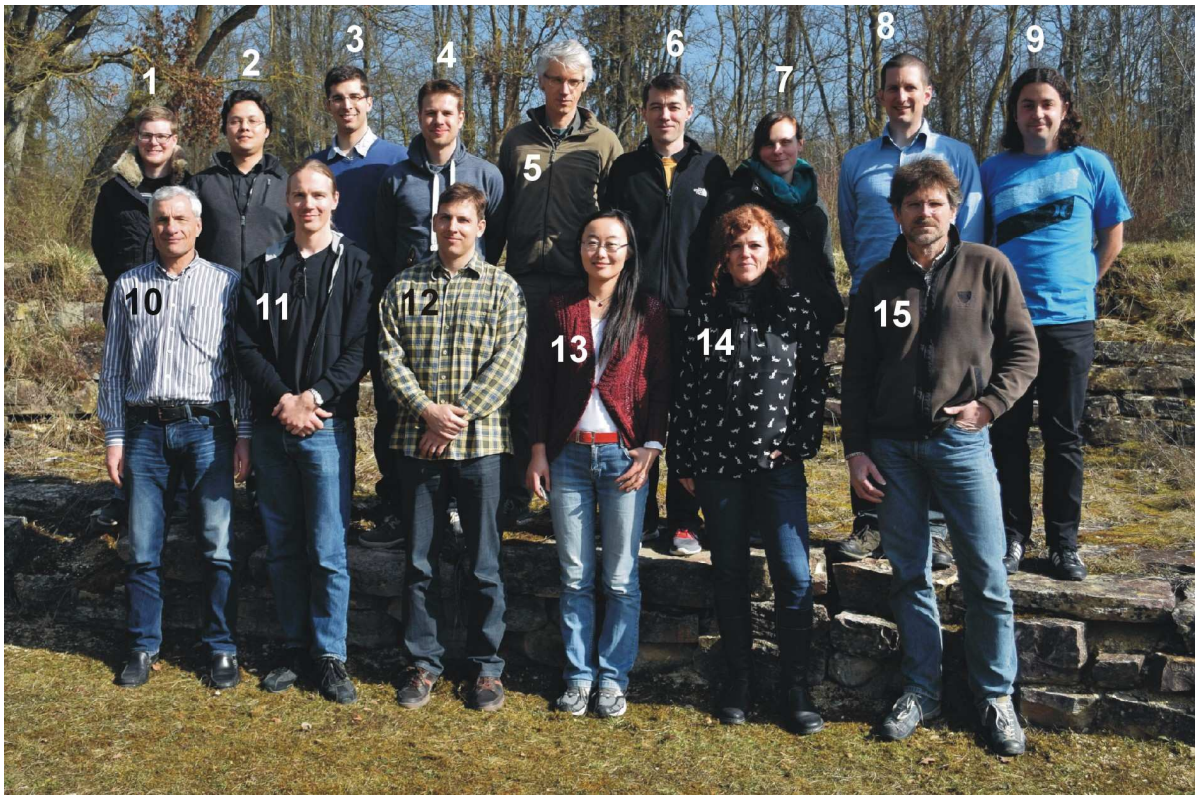

1:	Sven Bader	2:	Marian Caliebe	3:	Dominik Heinz
4:	Tobias Pusch	5:	Rainer Michalzik	6:	Alexander Hein
7:	Anna Bergmann	8:	Markus Daubenschüz	9:	Tobias Meisch
10:	Ferdinand Scholz	11:	Robert Leute	12:	Benedikt Westenfelder
13:	Junjun Wang	14:	Friederike Winter	15:	Peter Unger

Not on the photo:

Ahmed Al-Samaneh, Rainer Blood, Karl Joachim Ebeling, Mohamed Fikry, Alexander Kern, Sükran Kilic, Martin Klein, Hildegard Mack, Jürgen Mähnß, Gerlinde Meixner, Susanne Menzel, Eva Nüßle, Rudolf Rösch, Marcel Sattler, Ilona Schwaiger

Ulm University
Institute of Optoelectronics

Albert-Einstein-Allee 45, 89081 Ulm, Germany
URL: http://www.uni-ulm.de/opto
Fax: +49–731/50–2 60 49
Phone: +49–731/50–

Head of Institute			
Prof. Dr.	Peter Unger	–2 60 54	peter.unger@uni-ulm.de
Deputy Head			
Prof. Dr.	Ferdinand Scholz	–2 60 52	ferdinand.scholz@uni-ulm.de
Group Leader			
apl. Prof. Dr.-Ing.	Rainer Michalzik	–2 60 48	rainer.michalzik@uni-ulm.de
President of Ulm University			
Prof. Dr.	Karl Joachim Ebeling	–2 20 00	karl.ebeling@uni-ulm.de
Cleanroom Management			
Dr.-Ing.	Jürgen Mähnß	–2 60 53	juergen.maehnss@uni-ulm.de
Secretaries			
	Sükran Kilic^{+}	–2 60 59	suekran.kilic@uni-ulm.de
	Hildegard Mack	–2 60 60	hildegard.mack@uni-ulm.de
	Eva Nüßle	–2 60 50	eva.nuessle@uni-ulm.de
Research Staff			
M. Sc.	Ahmed Al-Samaneh*	–2 60 37	ahmed.al-samaneh@uni-ulm.de
Dipl.-Ing.	Anna Bergmann*	–2 60 38	anna.bergmann@uni-ulm.de
M. Sc.	Sven Bader	–2 60 37	sven.bader@uni-ulm.de
Dipl.-Ing.	Marian Caliebe	–2 60 39	marian.caliebe@uni-ulm.de
M. Sc.	Markus Daubenschüz	–2 60 38	markus.daubenschuez@uni-ulm.de
M. Sc.	Mohamed Fikry*	–2 61 95	mohamed.fikry@uni-ulm.de
Dipl.-Ing.	Alexander Hein	–2 60 46	alexander.hein@uni-ulm.de
Dipl.-Phys.	Dominik Heinz	–2 64 53	dominik.heinz@uni-ulm.de
Dipl.-Ing.	Alexander Kern*	–2 60 37	alexander.kern@uni-ulm.de
Dipl.-Ing.	Martin Klein	–2 60 44	martin.klein@uni-ulm.de
Dipl.-Phys.	Robert Leute	–2 60 56	robert.leute@uni-ulm.de
Dipl.-Phys.	Tobias Meisch	–2 60 56	tobias.meisch@uni-ulm.de
M. Sc.	Tobias Pusch	–2 60 37	tobias.pusch@uni-ulm.de
Dipl.-Inf.	Marcel Sattler*	–2 60 46	marcel.sattler@uni-ulm.de
M. Sc.	Junjun Wang	–2 61 95	junjun.wang@uni-ulm.de
Dipl.-Phys.	Benedikt Westenfelder*	–2 64 54	benedikt.westenfelder@uni-ulm.de
B. Inf. Com.	Friederike Winter*	–2 60 35	friederike.winter@uni-ulm.de

Technical Staff

Rainer Blood	–2 60 44	rainer.blood@uni-ulm.de
Gerlinde Meixner	–2 60 41	gerlinde.meixner@uni-ulm.de
Susanne Menzel	–2 60 41	susanne.menzel@uni-ulm.de
Rudolf Rösch	–2 60 57	rudolf.roesch@uni-ulm.de
Ilona Schwaiger^{+}	–2 60 56	ilona.schwaiger@uni-ulm.de

* Is an alumnus of the Institute meanwhile

$^{+}$ Currently on parental leave

Preface

In the year 2013, the three research groups of the Institute of Optoelectronics fruitfully continued their projects on vertical-cavity surface-emitting lasers (VCSELs) and systems, GaN-based optoelectronic devices, and semiconductor disk lasers. Results have been published extensively. Moreover, a number of students have completed their theses, as listed in the rear part of this Report.

The VCSELs and Optical Interconnects Group has brought its project on microfluidic-integrated particle sorting systems based on custom-designed laser arrays to a successful end. A new generation of Ph.D. students was hired and current projects focus on high-speed lasers for optical interconnect applications and novel VCSEL designs. The new VCSEL book edited by Rainer Michalzik was received well by the scientific community.

Studies of the GaN group continued to concentrate on semipolar heterostructures. A big step forward to sub-micrometer structured facet light emitting devices was done by implementing nano-imprint as a novel, simple lithographic technology. On the other hand, planar semipolar structures on patterned sapphire wafers could be significantly improved. First steps towards N-polar GaN helped to establish the direct growth of coaxial GaN-GaInN nano-structures without ZnO templates.

In the High-Power Semiconductor Laser Group, an optically-pumped semiconductor disk laser has been further improved, generating an output power of 25 W at the fundamental wavelength of 1040 nm. The frequency-doubled output power exceeds 11 W and shows an overall power conversion efficiency of nearly 25 % at 519 nm wavelength. Moreover, a laser system for optical trapping experiments on the barium ion, requiring high-power, stable single-frequency operation, and a narrow spectral linewidth, was realized in collaboration with the Institute of Quantum Matter.

During the Open Day of the Faculty on Nov. 7, the Institute presented a rich selection of research samples and cleanroom tours were offered to the interested public.

Rainer Michalzik
Ferdinand Scholz
Peter Unger Ulm, March 2014

VCSELs for Atomic Clock Demonstrators

Ahmed Al-Samaneh

We illustrate the output characteristics of two types of 895 nm vertical-cavity surface-emitting lasers (VCSELs) for use in miniaturized Cs-based atomic clocks and report on measurements that indicate the successful operation of clock demonstrators.

1. Introduction

Miniaturized atomic clocks (MACs) [1] are key elements for many applications such as communication systems, remote sensing, and global positioning. Such clocks use the principle of all-optical coherent population trapping (CPT) excitation which does not require a microwave cavity and VCSELs are the ideal light sources. They must feature strictly polarization-stable single-mode emission, have a narrow linewidth at a center wavelength of about 894.59 nm, and be suited for efficient harmonic current modulation at about 4.6 GHz in order to employ the CPT effect at the cesium D1 line [2, 3].

In this article we report some results obtained within the joint European MAC-TFC project [4]. Two different top-emitting oxide-confined VCSEL designs based on the AlGaAs–GaAs material system and InGaAs quantum wells have been utilized, as described in the next two sections.

2. Standard VCSELs

So-called standard VCSELs with a GaAs-substrate-side n-contact and a top annular p-contact (with an associated bondpad) have a circular light output aperture and are not polarization-stabilized. Several such VCSELs have been mounted in TO-46 cans for convenient testing and handling by project partners. The laser chips were fixed on silicon submounts by conductive glue. The anode of the TO can is wire-bonded to the top p-bondpad while the cathode is wire-bonded to the Au-metallized top surface of the Si submount. An external lens is employed for laser beam collimation. A thermoelectric cooler (TEC) and a thermistor are fixed in proximity of the VCSEL package for temperature control. Having no surface gratings, the polarization of the light emitted from standard VCSELs is a priori undefined. Devices with stable polarization in the operation range of interest have been selected. The polarization-resolved light–current–voltage (PR-LIV) characteristics of such a laser are shown in Fig. 1 (left). The threshold currents is around 0.3 mA and has a weak dependence on temperature, namely less than 2 µA/K in a range of 15 to 25°C (not illustrated here). Single-mode emission polarized parallel to the [011] GaAs reference crystal axis is maintained up to a current of 4.4 mA. Over this

range, the orthogonal polarization suppression ratio (OPSR) is greater than 20 dB. It is calculated according to

$$\mathrm{OPSR} = 10 \cdot \log\left(\frac{P_{\mathrm{par}}}{P_{\mathrm{orth}}}\right) \mathrm{dB}\ , \tag{1}$$

where P_{par} and P_{orth} are the optical powers measured behind a Glan–Thompson polarizer whose transmission direction is oriented parallel and orthogonal to the [011] crystal axis, respectively.

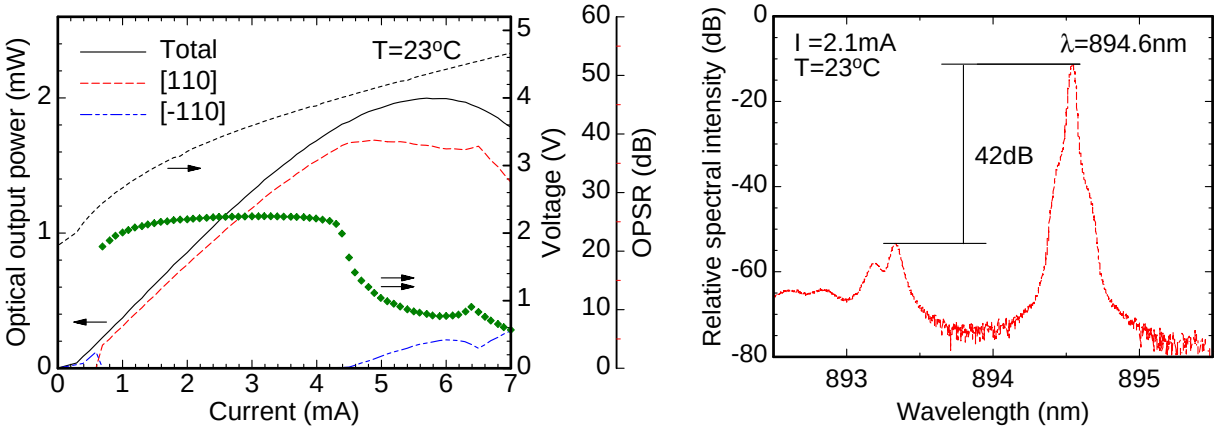

Fig. 1: Polarization-resolved operation characteristics of a standard VCSEL with $D_{\mathrm{a}} = 3\,\mu\mathrm{m}$ at $T = 23°\mathrm{C}$ (left) and its spectrum at $I = 2.1\,\mathrm{mA}$ (right).

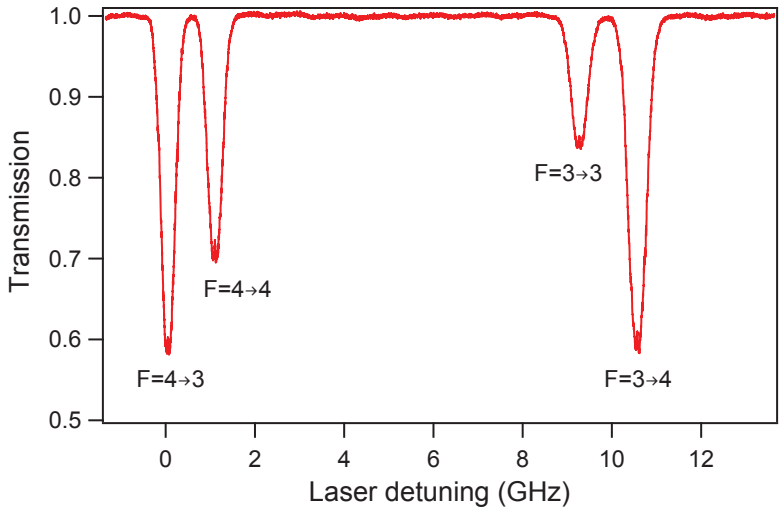

Fig. 2: Cs D_1 absorption lines observed when transmitting the light of the VCSEL from Fig. 1 through a Cs vapor cell (from [5]).

Figure 1 (right) depicts the optical spectrum at 23°C. The Cs D_1 line wavelength of 894.6 nm is reached at a current of 2.1 mA. The output power is 910 µW and the side-mode suppression ratio (SMSR) is about 42 dB. This laser was utilized to resolve all four hyperfine components of the Cs D_1 line, which are clearly separated in Fig. 2. Cs atomic

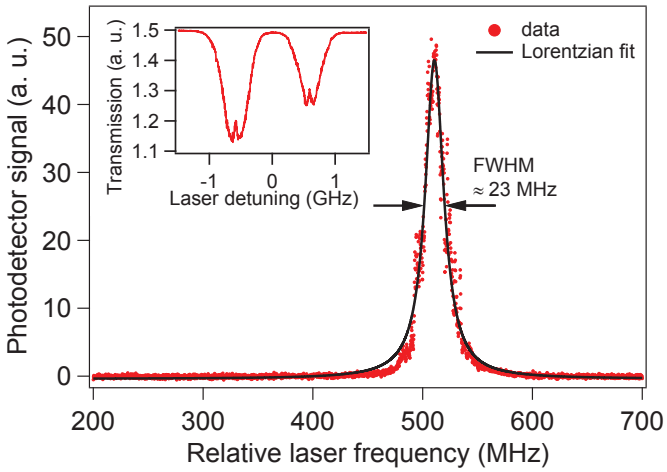

Fig. 3: Emission linewidth spectrum of the VCSEL from Fig. 1 operating at the Cs D_1 line. The Fabry–Pérot linewidth is 5 MHz and the total sweep time for this graph is 30 ms. The inset shows narrow saturated absorption features for the hyperfine transitions $|F = 4\rangle \rightarrow |F' = 3\rangle$ and $|F = 4\rangle \rightarrow |F' = 4\rangle$ of the Cs D_1 line, which were recorded for an evacuated Cs vapor cell (from [5]).

transitions are indicated using the quantum number F associated with the total atomic angular momentum **F**. The laser frequency is detuned over a 14 GHz span at a rate of $\approx$ 300 MHz/µA by sweeping the laser current. The VCSEL was operated at the bias current and temperature from Fig. 1 (right). The Cs absorption maxima appearing at detuning frequencies of 0, 1.2, 9.2, and 10.4 GHz correspond to the $|F = 4\rangle \rightarrow |F' = 3\rangle$, $|F = 4\rangle \rightarrow |F' = 4\rangle$, $|F = 3\rangle \rightarrow |F' = 3\rangle$, and $|F = 3\rangle \rightarrow |F' = 4\rangle$ atomic transitions, respectively, as indicated in Fig. 2. F is designated for the hyperfine structure of the $6^2S_{1/2}$ ground level and F' is assigned to the hyperfine structure of the $6^2P_{1/2}$ excited level. Not well-resolved saturated absorption features can be seen in the four lines. The resolution is improved below in Fig. 3.

2.1 Emission linewidth and modulation sidebands

Figure 3 shows an emission linewidth spectrum of the VCSEL from Fig. 1. The spectrum is measured using a scanning Fabry–Pérot interferometer with 5 MHz intrinsic linewidth and 1 GHz free spectral range. Typical measured full-width-at-half-maximum (FWHM) linewidths are around 20–25 MHz, by which narrow saturated absorption lines can be resolved, as depicted in the inset of Fig. 3. Similar saturated absorption features were reported for the Cs D_2 line at 852 nm wavelength [6]. Such details show that the emission linewidth of the VCSEL is narrower than the linewidths of the Cs absorption lines. Therefore, VCSELs are suitable laser sources for CPT-based atomic clocks in spite of their relatively large linewidths compared to other semiconductor lasers with distributed feedback (DFB) resonator or with an external cavity.

For atomic clock operation, the bias current of the VCSEL from Fig. 1 is modulated by a harmonic signal with a frequency of 4.596 GHz, equal to half the Cs hyperfine ground

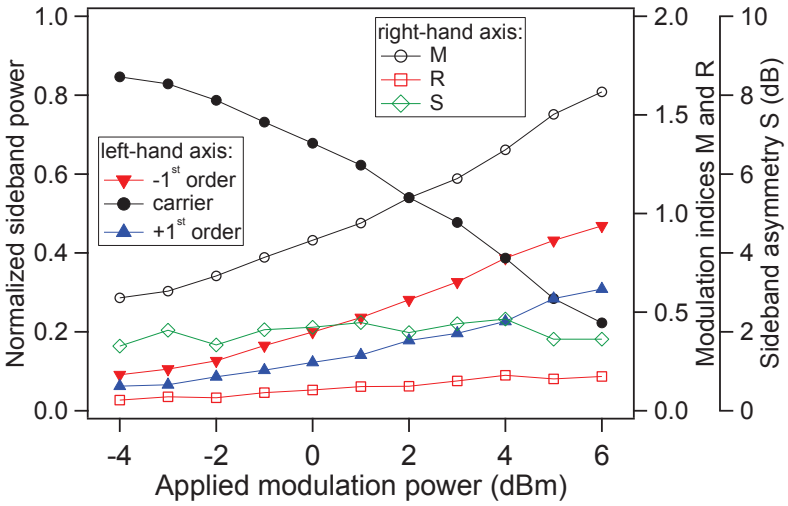

Fig. 4: Normalized power of the carrier and the first-order sidebands (filled symbols, left-hand axis) and corresponding modulation indices M and R and sideband asymmetry factor S (open symbols, right-hand axis) versus the modulation power with, where the 4.596 GHz signal is applied to the VCSEL from Fig. 1 (from [5]).

splitting frequency. This creates modulation sidebands separated by 9.192 GHz, as required for the CPT interaction to take place. Figure 4 shows the relative strengths of the carrier and the first-order sidebands in dependence of the modulation power, measured using a scanning Fabry–Pérot interferometer.

Neglecting any noise contributions, the time-dependent electric field $E(t)$ of light emission from a harmonically intensity-modulated VCSEL can be expressed as

$$E(t) = E_0 \cdot (1 + R\sin(2\pi f t + \phi)) \cdot \cos(2\pi\nu t + M\sin(2\pi f t)) \ , \tag{2}$$

where E_0 is a constant amplitude, ν is the optical carrier frequency, f is the modulation frequency, $R > 0$ and $M > 0$ are the amplitude and phase modulation indices, respectively, and ϕ is the relative phase between both modulations [7]. The modulation indices M and R extracted by fitting the sideband intensities resulting from (2) to the experimental data are depicted in Fig. 4. Also plotted is the asymmetry factor $S = 10 \cdot \log(I_{-1}/I_{+1})$ dB that is the ratio between the intensities in the -1 (lower frequency) and $+1$ (higher frequency) sidebands. As can be seen, $S \approx 2$ dB remains almost constant with applied modulation power, while R slightly changes from 0.05 to nearly 0.18. Both first-order sidebands become stronger than the carrier at modulation powers of $\geq +5$ dBm, and M increases but does not exceed 1.65. According to [8] $\alpha_{\mathrm{H}} = -M/R$, the Henry factor α_{H} increases from -11 to -8.5 over the applied range of modulation powers. The magnitude of α_{H} determined by this method is higher than usually expected. The optimum value of M for the CPT interaction is 1.8, at which most of the modulation modulation power is transferred to the first-order sidebands [9]. Limitations in modulation efficiency can be attributed to imperfect coupling of the modulation signal caused by impedance mismatch between the high-frequency source and the TO-46 can, which was evidenced by approximately 40 % power reflection [5]. Nevertheless, a CPT signal with a narrow linewidth is obtained, as will be shown in Fig. 8.

3. Inverted Grating Relief VCSELs

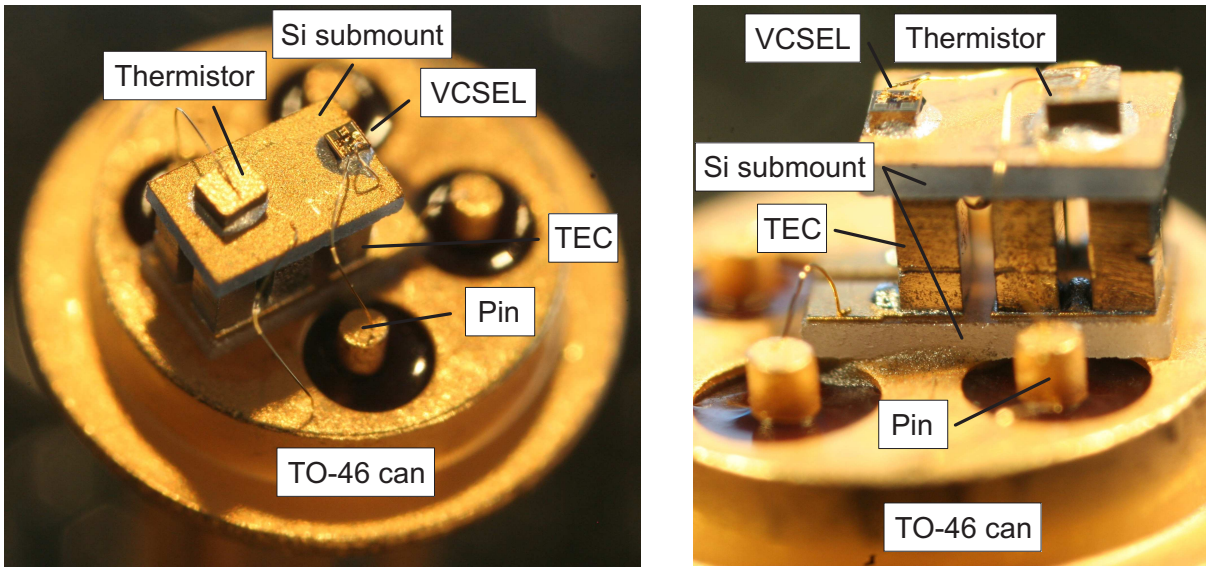

Fig. 5: VCSEL mounted along with a thermistor and a TEC in a TO-46 can (left). Close-up of the assembly taken at a different angle (right). The can has five pins: one for the thermistor, one for the p-pad of the VCSEL, two for operation of the TEC and one as a common ground for all elements. The ground pin is hidden below the lower Si submount.

The second type of VCSELs employed for the clock demonstrators has a flip-chip bondable layout with a top n-contact. In addition, it incorporates an inverted grating relief (IGR) etched into an extra topmost GaAs quarter-wave anti-phase layer of the output facet. In this way, favorable single-mode and polarization-stable laser emission is achieved [2]. Several such lasers have been mounted in TO-46 cans. Having top n-contacts, they were glued on silicon submounts. The anode and cathode of the TO-46 can were wire-bonded to the top p-type and n-type bondpads of the VCSEL. For temperature control, a TEC and a thermistor are placed inside the can, as displayed in Fig. 5.

PR-LIV characteristics of an IGR VCSEL at $T = 30°C$ are shown in Fig. 6 (left). Five times P_{par} is plotted here for better clarity. The device remains polarization-stable up to thermal roll-over with a maximum magnitude of the OPSR of 22.7 dB. The polarization of inverted grating VCSELs with optimum design is always orthogonal to the grating lines, resulting in an opposite sign of the OPSR in Fig. 6 (left) compared to Fig. 1 (left). Figure 6 (right) depicts polarization-resolved spectra at 30°C. The target wavelength is reached at a current of 1.4 mA with SMSR $\approx$ 40 dB and a peak-to-peak difference between the dominant and the suppressed polarization modes of almost 29 dB.

3.1 CPT resonance signal measurements

Figure 7 shows a simplified schematic of an experimental atomic clock setup. For the experiments in this section, the grating relief VCSEL from Fig. 6 in the mount from Fig. 5 is used. It is operated at 1.4 mA and 30°C to reach the Cs D_1 line wavelength, as can be

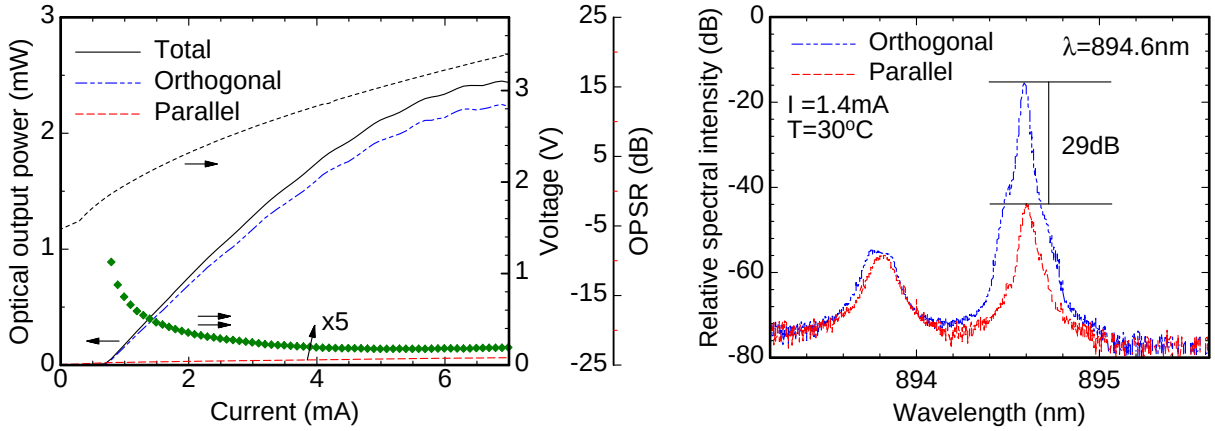

Fig. 6: Polarization-resolved operation characteristics of an IGR VCSEL with 3.6 µm active diameter at $T = 30°C$ (left) and its polarization-resolved spectra at $I = 1.4\,\mathrm{mA}$ (right). The grating relief has a diameter of 3 µm, a grating period of 0.6 µm and an etch depth of 70 nm.

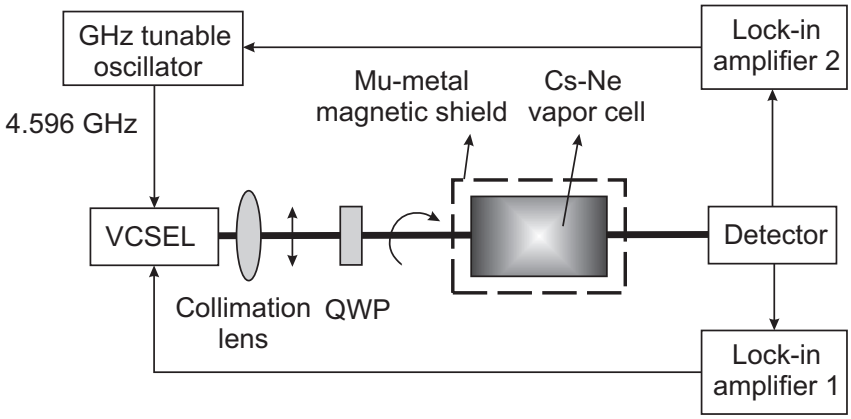

Fig. 7: Simplified schematic drawing of an experimental atomic clock demonstrator.

seen in Fig. 6 (right). The linewidth of the IGR VCSEL is measured to be approximately 25 MHz, which is close to the value of the standard VCSELs.

The optical output of the laser is collimated to a 2 mm diameter beam. The collimated laser beam is then circularly polarized using a quarter-wave plate (QWP) and transmitted through a microfabricated vapor cell. The laser power incident to the cell is about 22 µW. The injection current of the laser is modulated at 4.596 GHz using a commercial frequency synthesizer to produce two modulation sidebands separated by 9.192 GHz, as required for the CPT interaction. The modulation power is set to −2 dBm for a maximum amplitude of the CPT signal. The Cs cell is filled with Ne buffer gas for high short- and long-term frequency stability of the clock. The cell is stabilized to a temperature of ≈ 80°C, at which the sensitivity of the clock frequency to temperature variations is canceled [10, 11]. A static magnetic field of a few µT parallel to the laser beam is applied to split the Zeeman sublevels and enable a so-called σ^+–σ^+ CPT clock scheme on the Cs D_1 line. To prevent the influence of earth or environmental magnetic field perturbations, the cell is placed in a single-layer mu-metal magnetic shield. The σ^+–σ^+ CPT scheme line employs

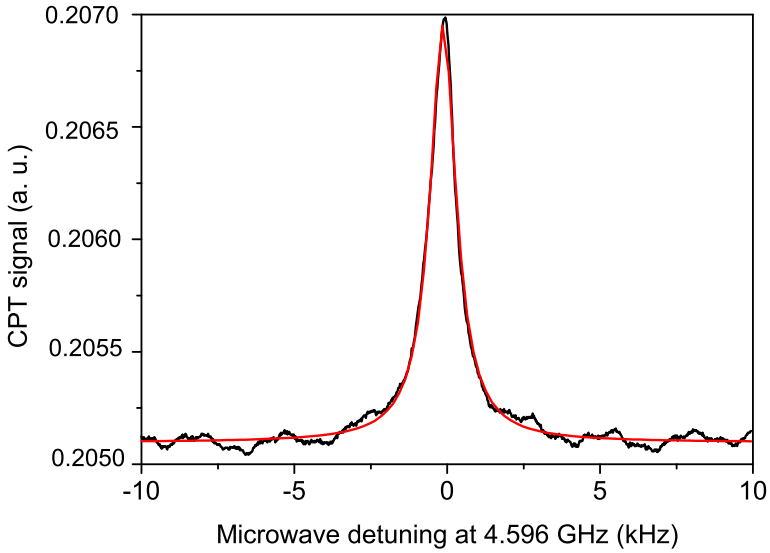

Fig. 8: Measured CPT resonance signal (black line) of a Cs–Ne microfabricated cell along with a Lorentzian curve fit (red line). The temperature of the cell is 80°C (after [5]).

$|F = 3, m_F = 0\rangle$ and $|F = 4, m_F = 0\rangle$ Zeeman sublevels as the two ground energy levels in the Λ-system. The σ^+ optical transition requires circularly polarized light, hence the necessity of the QWP.

The transmitted laser power is detected with a photodiode that provides signals for two lock-in amplifiers. The first one serves to stabilize the laser emission frequency at the Cs D_1 line, while the second provides the CPT signal, which is used to stabilize the GHz tunable oscillator at half of the Cs hyperfine ground splitting frequency. Figure 8 displays a CPT resonance signal obtained at the output of the second lock-in amplifier. The CPT signal is fit by a Lorentzian function. It has a linewidth of 1.04 kHz FWHM and a contrast of 0.93 % (ratio between signal amplitude and background) at 80°C cell temperature [5]. The linewidth does not vary significantly in the 70–90°C temperature range. The expected short-term instability of the clock from the CPT signal is $\sigma(\tau) = 2.9 \times 10^{-11}(\tau/\mathrm{s})^{-0.5}$ at $\tau \approx 1\,\mathrm{s}$ averaging times. The result proves that the developed VCSELs are very good candidates for the realization of high-performance Cs-based MACs [5].

Acknowledgment

We thank D. Setz for help with the processing of an early VCSEL generation and Philips U-L-M Photonics in Ulm for performing most of the VCSEL mounting steps. We acknowledge our MAC-TFC project partners at the Time and Frequency Laboratory (LTF), Physics Department, University of Neuchâtel, Neuchâtel, Switzerland for the characterization of the standard VCSELs (Figs. 2–4) and at FEMTO-ST, CNRS, Besançon, France for the CPT experiments (Fig. 8).

References

[1] S. Knappe, V. Shah, P.D.D. Schwindt, L. Hollberg, J. Kitching, L.A. Liew, and J. Moreland, "A microfabricated atomic clock", *Appl. Phys. Lett.*, vol. 85, pp. 1460–1462, 2004.

[2] A. Al-Samaneh, M. Bou Sanayeh, M.J. Miah, W. Schwarz, D. Wahl, A. Kern, and R. Michalzik, "Polarization-stable vertical-cavity surface-emitting lasers with inverted grating relief for use in microscale atomic clocks", *Appl. Phys. Lett.*, vol. 101, pp. 171104-1–4, 2012.

[3] M.J. Miah, A. Al-Samaneh, A. Kern, D. Wahl, P. Debernardi, and R. Michalzik, "Fabrication and characterization of low-threshold polarization-stable VCSELs for Cs-based miniaturized atomic clocks", *IEEE J. Select. Topics Quantum Electron.*, vol. 19, 1701410, 10 pages, 2013 (error in the caption of Fig. 6: 20°C must be 80°C).

[4] Web page: http://www.mac-tfc.eu; last visited Mar. 2014.

[5] F. Gruet, A. Al-Samaneh, E. Kroemer, L. Bimboes, D. Miletic, C. Affolderbach, D. Wahl, R. Boudot, G. Mileti, and R. Michalzik, "Metrological characterization of custom-designed 894.6 nm VCSELs for miniature atomic clocks", *Opt. Express*, vol. 21, pp. 5781–5792, 2013.

[6] C. Affolderbach, A. Nagel, S. Knappe, C. Jung, D. Wiedenmann, and R. Wynands, "Nonlinear spectroscopy with a vertical-cavity surface-emitting laser", *Appl. Phys. B*, vol. 70, pp. 407–413, 2000.

[7] R. Wynands and A. Nagel, "Inversion of frequency-modulation spectroscopy line shapes", *J. Opt. Soc. Am. B*, vol. 16, pp. 1617–1622, 1999.

[8] C. Harder, K. Vahala, and A. Yariv, "Measurement of the linewidth enhancement factor α of semiconductor lasers", *Appl. Phys. Lett.*, vol. 42, pp. 328–330, 1983.

[9] S. Kobayashi, Y. Yamamoto, M. Ito, and T. Kimura, "Direct frequency modulation in AlGaAs semiconductor lasers", *IEEE J. Quantum Electron.*, vol. 30, pp. 428–441, 1982.

[10] D. Miletic, P. Dziuban, R. Boudot, M. Hasegawa, R.K. Chutani, G. Mileti, V. Giordano, and C. Gorecki, "Quadratic dependence on temperature of Cs 0–0 hyperfine resonance frequency in single Ne buffer gas microfabricated vapour cell", *Electron. Lett.*, vol. 46, pp. 1069–1071, 2010.

[11] R. Boudot, P. Dziuban, M. Hasegawa, R.K. Chutani, S. Galliou, V. Giordano, and C. Gorecki, "Coherent population trapping resonances in Cs–Ne vapor microcells for miniature clocks applications", *J. Appl. Phys.*, vol. 109, pp. 014912-1–11, 2011.

Optical Multiple-Particle Manipulation With a Rectangular-Shaped VCSEL

Anna Bergmann and Marwan Bou Sanayeh

Optical manipulation of cells and particles is an efficient non-destructive technique for isolation and sorting in the field of biophotonics. For several years, vertical-cavity surface-emitting lasers (VCSELs) have been investigated as light sources for particle manipulation inside microfluidic channels, where their small dimension and low power consumption enable direct integration with the channels. In such an integrated module, however, the simultaneous manipulation of multiple particles requires the use of densely packed VCSEL arrays with very small device pitch, making the fabrication process more expensive and complicated. We show efficient single as well as multiple polystyrene particle trapping and sorting inside polydimethylsiloxane (PDMS) microfluidic channels using one rectangular-shaped top-emitting AlGaAs–GaAs VCSEL with an active aperture area of about 100 × 14 μm^2. The VCSEL emission wavelength is around 850 nm, which is suitable for usage in biophotonics, as biological materials present little absorption in the near-infrared spectral range. Furthermore, the oblong-shaped VCSELs can potentially be integrated with PDMS microfluidic channels to form miniaturized optofluidic chips for ultra-compact particle handling and manipulation.

1. Introduction

The first transverse two-dimensional optical trap was demonstrated in 1970 by Arthur Ashkin [1]. Later he extended this concept to a three-dimensional trap [2]. The working principle is based on the momentum transfer from an incident laser beam to a transparent particle. The particle is pushed forward by light radiation pressure, an effect commonly known as scattering force. For a laser beam with a transverse intensity gradient, the resulting net force pulls the particle towards the maximum of light intensity, creating a two-dimensional optical trap. In the three-dimensional trap, also known as optical tweezers, the forward scattering force is compensated by a longitudinal gradient force when the laser beam is tightly focused. For transparent particles in water, some milliwatts of optical power are sufficient to exert trapping forces in the piconewton regime [3].

Optical tweezers offer the possibility to manipulate microparticles and cells without any mechanical contact, greatly reducing the risk of contamination and mechanical damage [4]. This unique advantage has made them very attractive in the field of biophotonics. Using infrared-emitting lasers greatly reduces the risk of thermal damage, because biological materials show minor absorption in the near-infrared spectral region [3, 4]. The handling of biological samples in microfluidic channel structures with widths below 100 µm enables

the drastic reduction of the used sample volume, parallel cycling, and exact timing [5, 6]. Combining microfluidics and optical trapping in an integrated module is the ultimate tool to efficient manipulation of particles and cells without the usage of extensive equipment [7, 8].

In recent years, VCSELs have proven to be excellent light sources for optical trapping, especially due to their small dimension, low price, ease of fabrication, and high-quality output beam [8–13]. Furthermore, due to their vertical emission, VCSELs can be arranged in two-dimensional arrays, which can be employed for simultaneous optical trapping and movement of several cells [10, 12], as well as stacking of polystyrene particles [11]. In all experiments, the optical VCSEL traps were created by focusing the laser beam with a high numerical aperture objective.

Commercial VCSEL arrays used in optical communication typically have a large device pitch of 250 µm. For miniaturized optical trapping without external optics, however, these arrays need to be densely packed, with a center-to-center distance in the range of 25 µm [14]. This makes their fabrication process more expensive as well as complicated. In this article, a different type of VCSEL has been used to demonstrate simultaneous optical trapping of several particles, namely a rectangular top-emitting 850 nm AlGaAs–GaAs VCSEL having an active aperture area of around $100 \times 14\,\mu m^2$. A brief description and characterization of the VCSEL is presented. The results of single as well as multiple trapping and sorting of polystyrene particles inside PDMS microfluidic channels are demonstrated.

2. Rectangular-Shaped VCSEL – Device Description

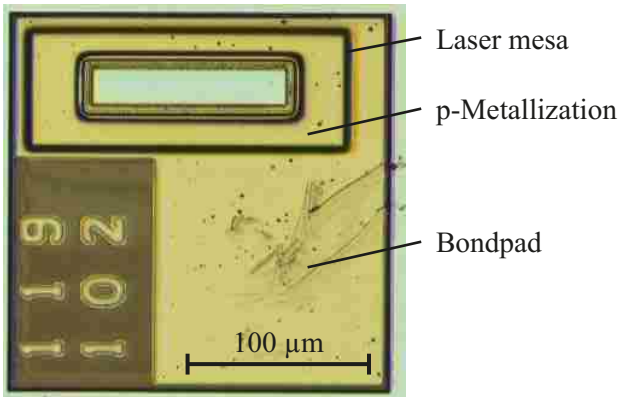

Fig. 1: Top view of a fully processed rectangular-shaped VCSEL. The oxide aperture is around $100 \times 14\,\mu m^2$. The rectangular laser mesa as well as the bondpad are clearly visible.

Rectangular top-emitting VCSELs have been provided by Philips Technologie GmbH U-L-M Photonics (www.ulm-photonics.com). The electrically pumped, oxide-confined VCSELs consist of 37 Si-doped AlGaAs n-type distributed Bragg reflector (DBR) pairs, a cavity with 3 GaAs quantum wells and an oxide aperture for current confinement, and 21 C-doped AlGaAs p-DBR pairs. The wafer is designed for laser emission at around

850 nm. Figure 1 shows the top view of a fully processed rectangular-shaped VCSEL with an active area of $100 \times 14\,\mu m^2$. The operation characteristics of the VCSEL used in this work are depicted in Fig. 2. All measurements were done at room temperature. As visible in Fig. 2 (left), the VCSEL has a threshold current of about 20 mA and a roll-over current of about 90 mA, at which a maximum output power of about 39 mW is achieved. The optical spectra displayed in Fig. 2 (right) were measured at three different currents between threshold and roll-over. The red-shift in wavelength is due to increased internal temperature with increasing current. Near threshold, only a few modes oscillate, whereas far above threshold the laser is strongly multimode.

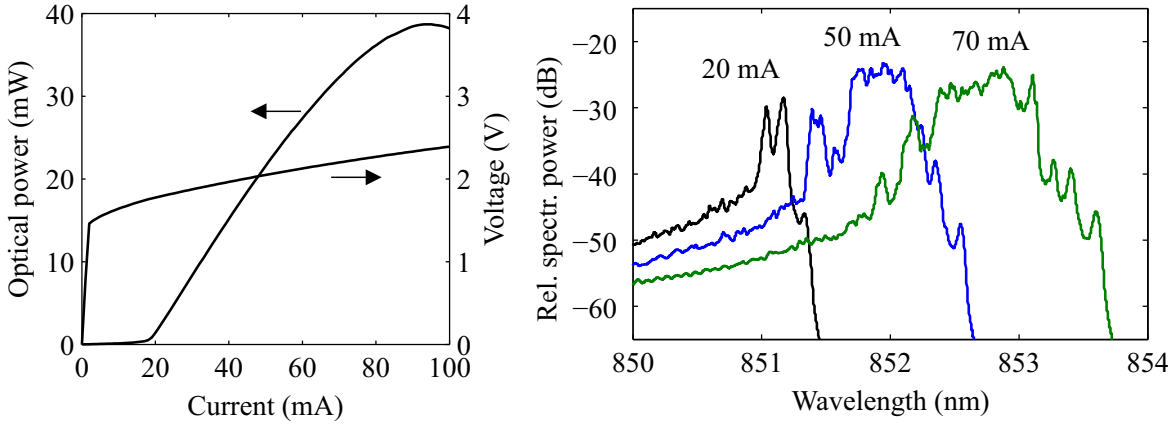

Fig. 2: Light–current–voltage characteristics (left) and optical spectra (right) of the rectangular VCSEL used for optical manipulation. The spectra are measured at three different currents between threshold and roll-over.

The near- and far-field profiles of the VCSEL are depicted in Fig. 3. The near-field intensity was measured at an operating current of 85 mA or an output power of 35 mW. It is stronger at the border of the laser but exhibits a relatively homogeneous distribution along the surface. The far-field was measured parallel to the long axis of the VCSEL at three operating currents and is dominated by two peaks with angles between about $\pm 10°$ with respect to the optical axis. A theoretical analysis of the modal properties of similar rectangular VCSELs is presented in [15].

3. Particle Manipulation Experiments

The microfluidic channels are made of polydimethylsiloxane, a transparent and inert polymer. It is often used for prototyping due to straightforward fabrication based on a molding technique [5]. In the so-called soft lithography technique, the material is poured over a master wafer containing the inverse channel structure. Afterwards, the PDMS is cured and peeled off the master wafer.

In the experimental setup [16], the VCSEL is placed on a copper mount and electrically connected to a current source. The VCSEL output beam is collimated and then tightly focused into the sample stage by two objectives. To achieve a strong intensity gradient, an objective with a high numerical aperture of 1.25 is used. Thus, an optical trap is generated

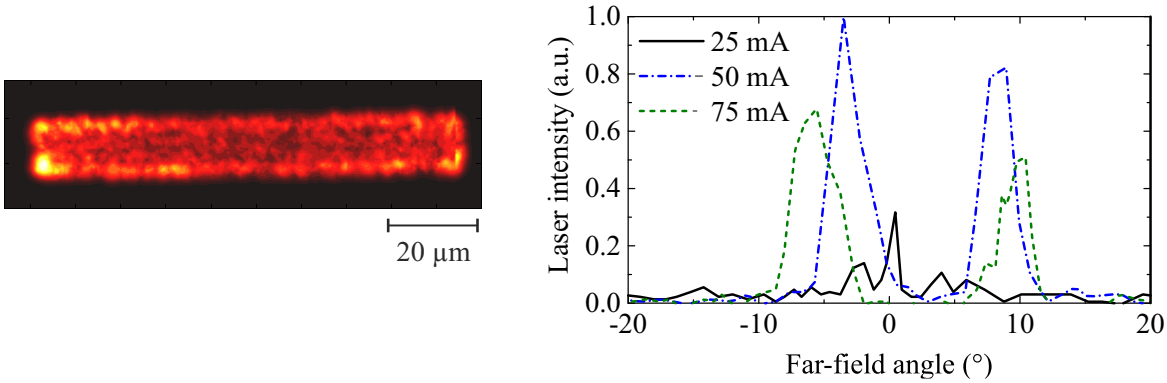

Fig. 3: Near-field (left) and long-axis far-field (right) of the rectangular VCSEL used for optical manipulation. The near-field was measured at 85 mA and the far-field at three different currents between threshold and roll-over.

inside the microfluidic channel, which is placed on a computer-controlled positioning system and filled with polystyrene particles in water solution. With the positioning system, a precise relative movement between channel and laser can be realized.

Using this setup, successful trapping of single and multiple polystyrene particles inside PDMS microfluidic channels with widths of 60 and 75 µm was achieved. After trapping with the rectangular VCSEL, the particle can be moved to any desired position in the channel. The tested particles have sizes between 1 and 10 µm. Figure 4 shows a 10 µm particle flowing down a 75 µm wide microchannel. The laser is positioned in the flow track of the particle (1). The particle is trapped by the laser (2), which is then moved from the lower to the upper part of the channel (3,4). Afterwards, the particle is released and the flow track was successfully manipulated (5). As another approach, the particle can be fixed by the laser and thus separated from the other particles while they are flowing by. Another experiment for potential particle sorting is depicted in Fig. 5. Here, there was no flow in the 60 µm wide channel. It is shown how the laser traps two 10 µm particles in the upper part of the channel (1) and moves them to the lower branch of the Y-junction (2–4). With this technique, two types of particles can be separated from each other for sorting applications.

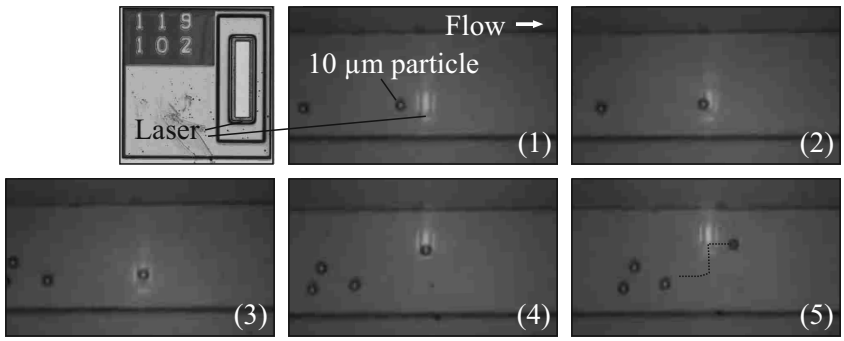

Fig. 4: Optical manipulation of a single 10 µm polystyrene particle under flow inside a 75 µm microfluidic channel. In this experiment, the flow track of the particle is manipulated.

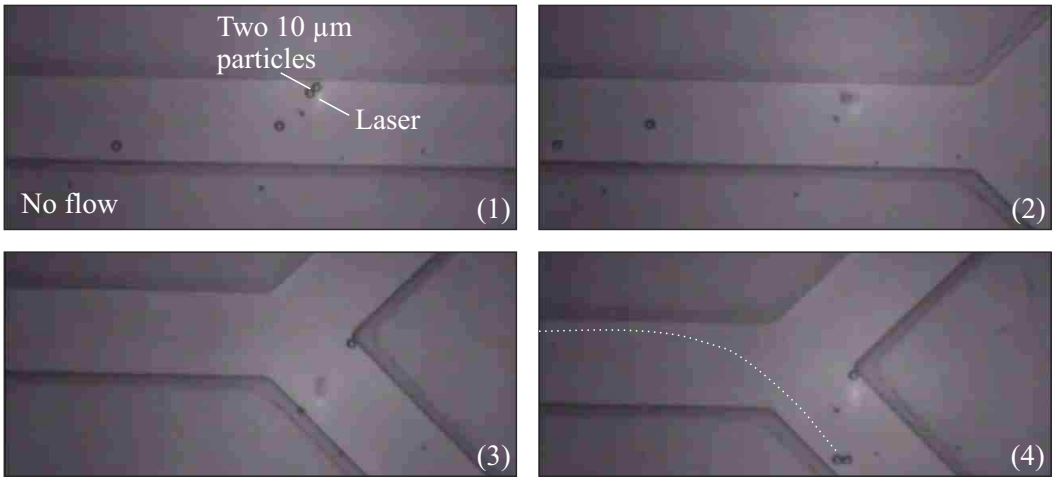

Fig. 5: Simultaneous optical trapping of two 10 µm polystyrene particles without flow inside a 60 µm microfluidic channel. In this experiment, particle sorting is achieved by placing them in the desired branch of the Y-junction.

4. Conclusion

In this paper, successful optical particle manipulation using a rectangular-shaped VCSEL was demonstrated. Unlike circular VCSELs, this laser has a rectangular 100 × 14 µm^2 active aperture area and shows rather homogeneous lasing over the entire large aperture. The device dimensions can easily be adapted to the specific application. Being oblong, this VCSEL can replace the linear arrangement of circular VCSELs which is typically used to simultaneously trap more than one particle, and it has the advantages of being cheaper and easier to fabricate. The results show the excellent multi-particle trapping ability of this VCSEL. Moreover, this VCSEL, like its VCSEL array predecessors [14], can be integrated directly underneath the microfluidic channel without the need of external optics. Therefore, portable and inexpensive microfluidic chips for biological particle manipulation can potentially be designed.

References

[1] A. Ashkin, "Acceleration and trapping of particles by radiation pressure", *Phys. Rev. Lett.*, vol. 24, pp. 156–159, 1970.

[2] A. Ashkin, J.M. Dziedzic, J.E. Bjorkholm, and S. Chu, "Observation of a single-beam gradient force optical trap for dielectric particles", *Opt. Lett.*, vol. 11, pp. 288–290, 1986.

[3] K.C. Neumann and S.M. Block, "Optical trapping", *Rev. Sci. Instrum.*, vol. 75, pp. 2787–2809, 2004.

[4] K. Dholakia, P. Reece, and M. Gu, "Optical manipulation", *Chem. Soc. Rev.*, vol. 37, pp. 42–55, 2008.

[5] J.C. McDonald and G.M. Whitesides, "Poly(dimethylsiloxane) as a material for fabricating microfluidic devices", *Acc. Chem. Res.*, vol. 35, pp. 491–499, 2002.

[6] N.-T. Nguyen, *Mikrofluidik*. Wiesbaden: Teubner Verlag, 2004.

[7] R.W. Applegate Jr., J. Squier, T. Vestad, J. Oakey, D.W.M. Matt, P. Bado, M.A. Dugan, and A.A. Said, "Microfluidic sorting system based on optical waveguide integration and diode laser bar trapping", *Lab Chip*, vol. 6, pp. 422–426, 2006.

[8] M. Wang, M. Ozkan, E. Ata, P. Wen, M. Sanchez, C. Ozkan, O. Kibar, and S. Esener, "Integration of optoelectronic array devices for cell transport and sorting", in *Optical Diagnostics of Living Cells*, D.L. Farkas, R.C. Leif (Eds.), Proc. SPIE 4260, pp. 68–73, 2001.

[9] A. Kroner, J.F. May, I. Kardosh, F. Rinaldi, H. Roscher, and R. Michalzik, "Novel concepts of vertical-cavity laser-based optical traps for biomedical applications", in *Biophotonics and New Therapy Frontiers*, R. Grzymala, O. Haeberlé (Eds.), Proc. SPIE 6191, pp. 619112-1–12, 2006.

[10] B. Shao, S. Zlatanovic, M. Ozkan, A.L. Birkbeck, and S.C. Esener, "Manipulation of microspheres and biological cells with multiple agile VCSEL traps", *Sensors and Actuators B*, vol. 113, pp. 866–874, 2006.

[11] F. Sumiyama, Y. Ogura, and J. Tanida, "Fabrication of three-dimensional microscopic structure by VCSEL array trapping", in *Optical Trapping and Optical Micromanipulation*, K. Dholakia, G.C. Spalding (Eds.), Proc. SPIE 5514, pp. 379–386, 2004.

[12] A.L. Birkbeck, R.A. Flynn, M. Ozkan, D. Song, M. Gross, and S.C. Esener, "VCSEL arrays as micromanipulators in chip-based biosystems", *Biomedical Microdevices*, vol. 5, pp. 47–54, 2003.

[13] Y. Ogura, T. Beppu, F. Sumiyama, and J. Tanida, "Toward photonic DNA computing: developing optical techniques for parallel manipulation of DNA", in *Photonics for Space Environments X*, E.W. Taylor (Ed.), Proc. SPIE 5897, pp. 34–43, 2005.

[14] A. Bergmann, N.I. Khan, J.A. Martos Calahorro, D. Wahl, and R. Michalzik, "Hybrid integration approach of VCSELs for miniaturized optical deflection of microparticles", in *Semiconductor Lasers and Laser Dynamics V*, K. Panajotov, M. Sciamanna, A. Valle, R. Michalzik (Eds.), Proc. SPIE 8432, pp. 843204-1–12, 2012.

[15] S. Gronenborn, T. Schwarz, P. Pekarski, M. Miller, H. Mönch, and P. Loosen, "Optical modes in a rectangular VCSEL resonator with properties of both Gaussian and Fourier modes", *IEEE J. Quant. Electron.*, vol. 48, pp. 1040–1044, 2012.

[16] A. Kroner, C. Schneck, F. Rinaldi, R. Rösch, and R. Michalzik, "Application of vertical-cavity laser-based optical tweezers for particle manipulation in microfluidic channels", in *Nanophotonics II*, D.L. Andrews, J.-M. Nunzi, A. Ostendorf (Eds.), Proc. SPIE 6988, pp. 69881R-1–12, 2008.

Establishing a Two Step FACELO Process in HVPE

Martin Klein

In order to reduce the effort needed to create self-separated, freestanding gallium nitride (GaN) layers by thick growth in hydride vapor phase epitaxy (HVPE), we established a two-step facet-controlled lateral overgrowth (FACELO) process in HVPE. Just as for the metalorganic vapor phase epitaxy (MOVPE) FACELO process, the template is produced by MOVPE growth directly on sapphire. This initial GaN layer is masked with 200 nm of silicon nitride (SiN_x), hexagonally structured by optical lithography. Instead of a previously used second MOVPE growth step, the masked sample is directly overgrown in HVPE to create a network of inverse pyramidal structures, before being planarized in a second growth step within the same growth run. Separation of a full 2 inch wafer could be achieved by adding a third, long growth step in HVPE which produced the necessary GaN layer thickness.

1. Introduction

Becoming an increasingly common material, gallium nitride (GaN) still suffers from the lack of suitable substrates. This leads to the need for heteroepitaxy in mid and low price applications. Although homoepitaxy is used for producing blue and green laser diodes, available GaN substrates are much too costly for growing LEDs and transistors on them. To achieve affordable homoepitaxial substrates, great efforts have been made in the field of ammonothermal growth [1]. Yet, thick layers grown by HVPE are still a good candidate to provide GaN wafers for future industrial processes [2, 3]. Although being researched for some time, producing such layers is still no trivial task. Differences in the thermal expansion coefficients of GaN and sapphire and the large mismatch in their respective lattice constants result in strain and defects in the GaN layer and in big curvatures of the respective samples. In order to cope with these problems, several methods have been developed to remove the GaN layer from the substrate such as laser-lift-off (LLO) [4], mechanical polishing [5] or growth on etchable substrates like ZnO [6]. Our approach is to use the difference in thermal expansion coefficients to induce a self separation of layer and substrate during cooldown. With our self-fabricated MOVPE templates, we create weak interlayers which define a breaking point for the separation at a predetermined position. In the last years, our institute has developed a standardized procedure to create suitable templates [7].

However, with two MOVPE growth steps and one subsequent long HVPE growth step for self separation, this procedure is complicated and tedious. To simplify the process, we intend to move the second MOVPE growth step, a FACELO overgrowth of the separation mask, to the HVPE process. The FACELO process contains at least two growth stages,

which needed to be established in the HVPE. The first stage consists of a 3D growth of pyramidal structures, starting from the masked template. This is necessary to bend the defects that protrude from the template through the mask openings. In consequence these defects are expected to run parallel to the wafer surface when the second step of the FACELO growth is applied. In this second step the sample is planarized by growing in a 2D growth mode. Using such a FACELO process, it is possible to reduce the amount of defects in the following epitaxial layers considerably [8]. FACELO has been established for HVPE before [9], however in our case the mask additionally serves as the above mentioned predetermined breaking point for self separation of the thick HVPE layer.

2. Growth Start and 3D Growth Step

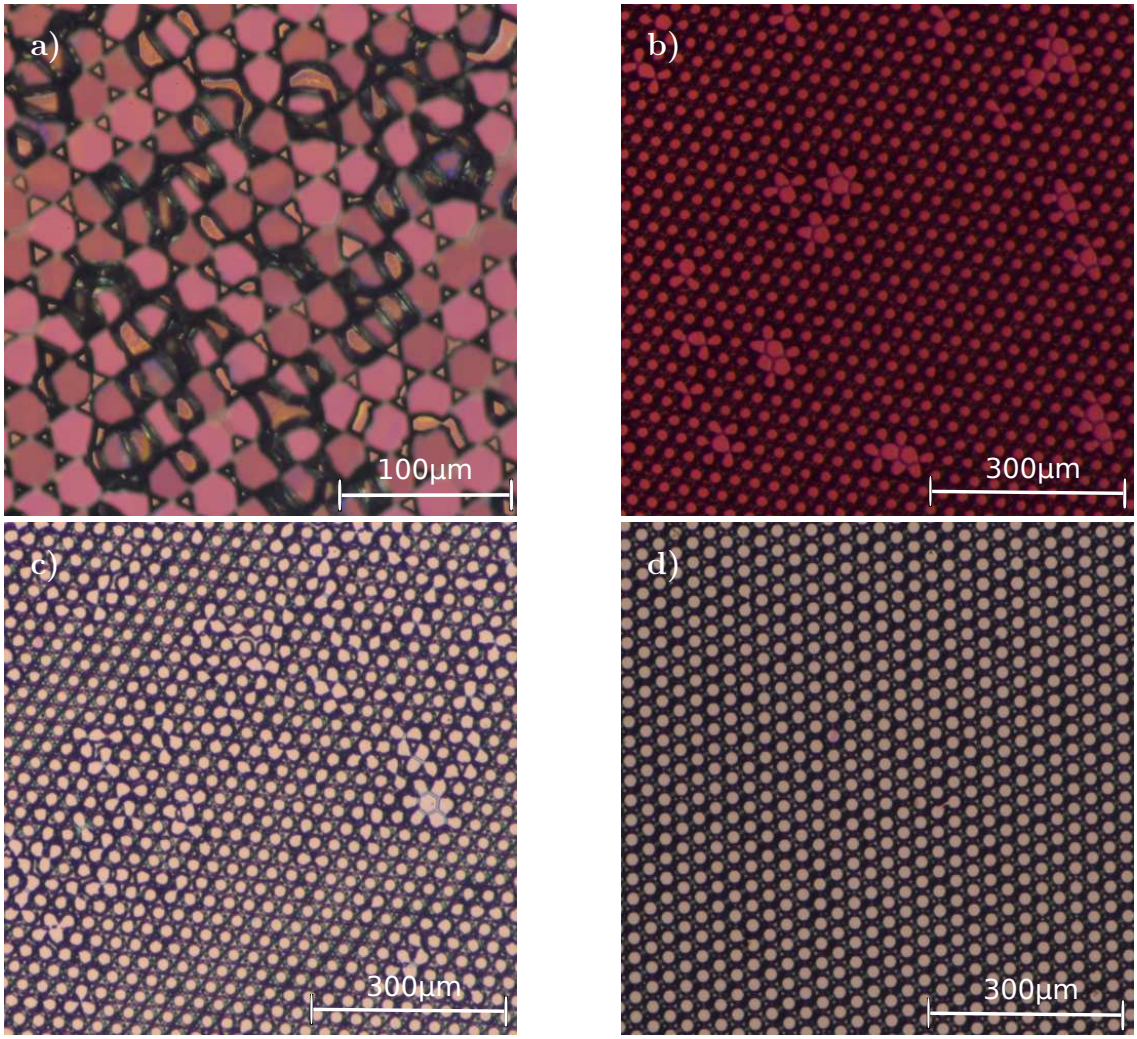

Fig. 1: Nomarski microscopic image, 10 minutes growth on masked template at a) 1050 °C, b) 1000 °C, c) 980 °C and d) 950 °C.

Following the guidelines from a work of Chelda-Gourmala et al. [10], we found suitable

growth conditions for the 3D-mode growth. When comparing the results of this work to our growth result, we see that the V-III ratios can't be taken one to one. Apparently in our reactor a large amount of ammonia doesn't reach the growth zone so that we have to increase the V-III ratio roughly by a factor of 10 for our growth. This brought us to the conclusion that the V-III ratio of 77 which we typically use for thick layer growth (see table 1) would be a good starting point. In order to achieve more homogenous growth at low growth rates and to overcome the design problems of a horizontal reactor with type III showerheads, we increased the V-III ratio to 100. As the first experiment delivered very nicely developed shapes in some spots all over the wafer, we concluded that the V-III ratio was chosen correctly. However, Fig. 1 a) shows a microscopic image of a part of this sample where the growth result was not yet satisfactory. As we can see, growth is limited to some small areas, mainly in the junctions of the mask openings. This indicates high mobility of the source atoms on the wafer, resulting in too strong selectivity.

To decrease the mobility we decreased the growth temperature of the first growth step in three consecutive samples from 1050 °C to 950 °C. Figure 1 b) shows a microscopic image of a typical part of the sample grown at 1000 °C. Growth is now a lot more uniform than at a growth temperature of 1050 °C. However, we still see areas where no growth occured, typically around a small flaw in the mask or template, visible at higher magnifications.

In the next step we decreased the growth temperature to 980 °C (Fig. 1 c)). Now, the amount of spots with no growth has been vastly reduced. Even so, some areas still show distorted features.

Reducing the temperature further down to 950 °C, removes these distortions. Growth is now very homogenous on the whole wafer. A typical microscopic image of such sample can be seen in Fig. 1 d).

3. 2D Growth Step and Planarization

In order to planarize the GaN-layer, we need to enhance the growth parallel to the substrate surface. According to Chelda-Gourmala et al. [10] decreasing the V-III ratio further could highly favor lateral over vertical growth on the $\{1\bar{1}00\}$ facets while favoring vertical over lateral growth on $\{11\bar{2}0\}$ facets. If we increase the V-III ratio, this publication predicts that we get no growth at all on $\{11\bar{2}0\}$ facets while equalizing growth speeds of lateral and vertical growth on $\{1\bar{1}00\}$ facets. As we have a mixture of both facets we couldn't be sure which growth will dominate. Therefore we started two experiments, one growth run reducing the V-III ratio to 50 (Fig. 2 a)), one increasing it to 230 (Fig. 2 b)). As can easily be seen, with the V-III ratio of 50 the inverted pyramids show almost no coalescence. With a V-III ratio of 230, however, we achieve a closed layer with some remaining holes.

To push the growth even stronger into 2D-mode, we increased the V-III ratio to 300 (Fig. 2 c)). Now, at least in the center of the wafer almost all holes are closed after 60 minutes of growth.

The next challenge was to find the right lenght of time to have the top-layer coalesced on the whole wafer with minimal top-layer thickness. From earlier experiments we know that

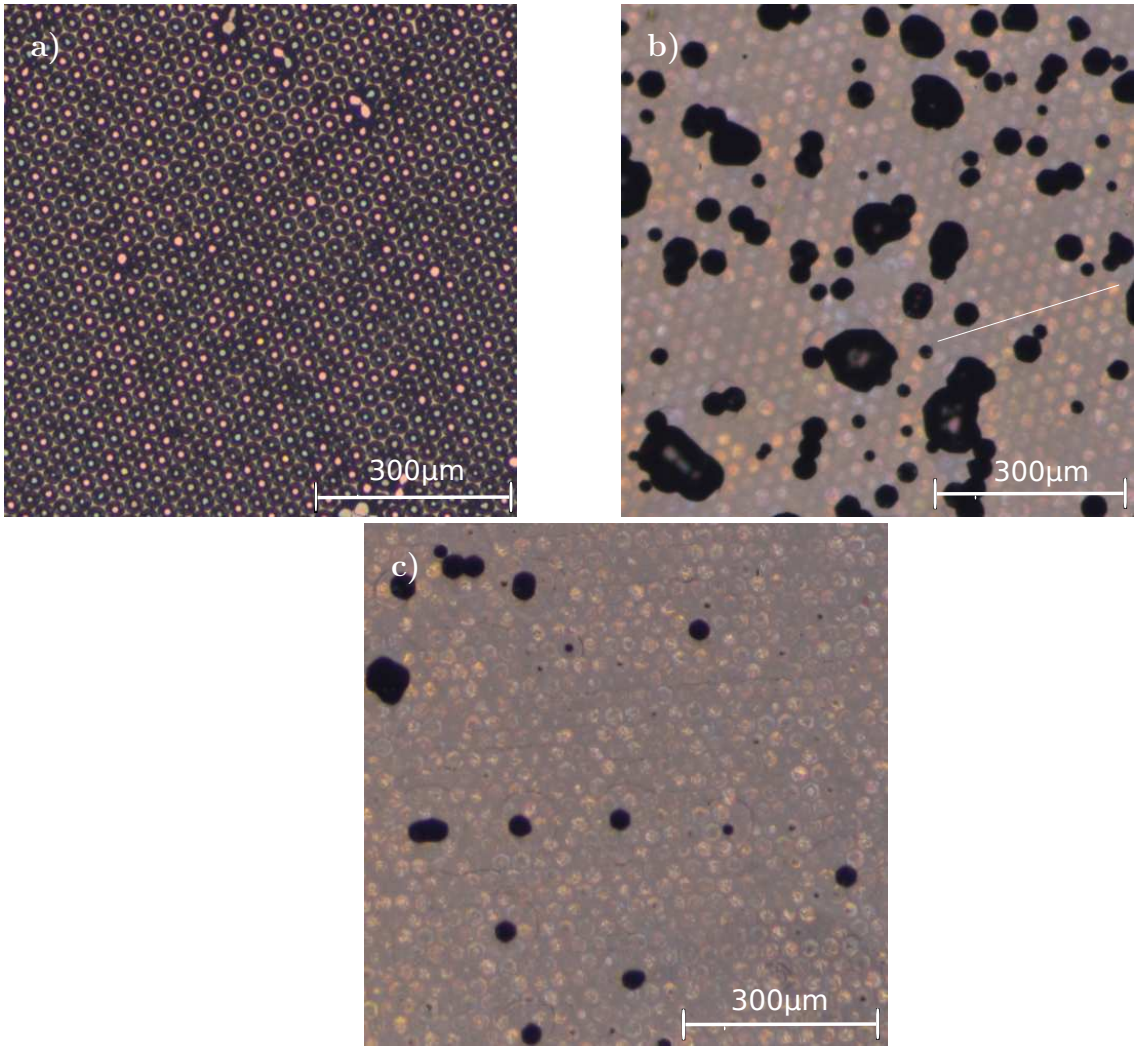

Fig. 2: Nomarski microscopic image, 60 minutes growth on inverted pyramids, wafer center, V-III ratio of a) 50, b) 230 and c) 300.

thick layers grown with this V-III ratio tend to crack. On the other hand the growth-speed is lower at the wafer edge, so this growth has to be applied long enough to coalesce the layer even at the wafer edges. In our experiments, coalescence of the hexagonally shaped mask with 30 µm period and 2 µm openings can be achieved after about 70 µm of vertical growth.

In Figs. 3 a) and 3 b) we can see microscopic images taken from the edge of the wafer after 60 minutes and 90 minutes of growth with a V-III ratio of 230. To be sure that the sample is properly planarized before thick layer growth, we extended the growth in 2D mode to 105 minutes at a V-III ratio of 300.

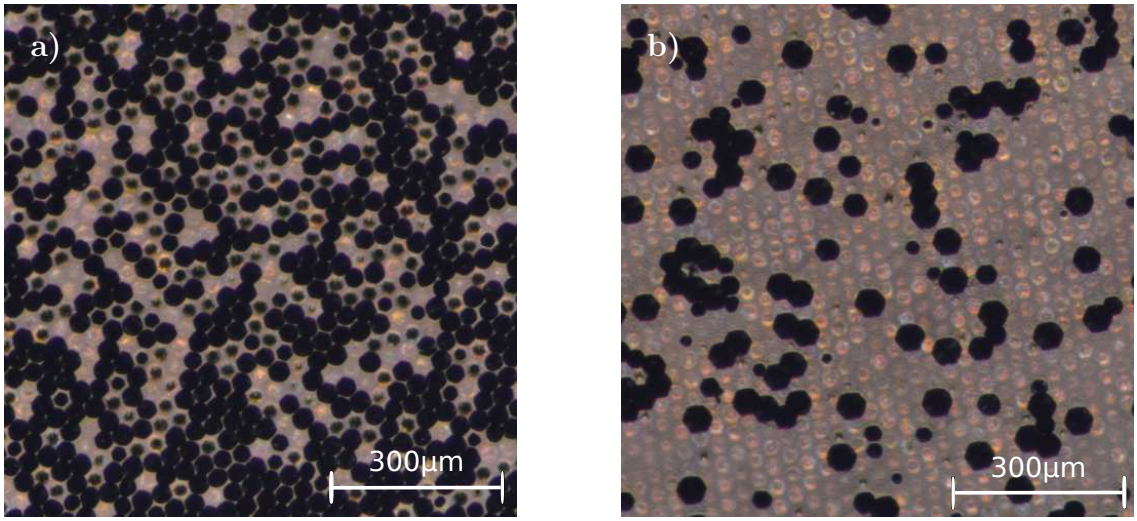

Fig. 3: Nomarski microscopic image, V-III ratio of 230 on inverted pyramids, wafer edge, growthtime a) 60 and b) 90 minutes.

4. Thick Growth and Self-Separation

Applying our standard growth parameters (see table 1), we increased the total layer thickness to enable self-separation during the cool-down-phase of the process. The maximum achievable thickness in our reactor is about 1.5 mm before the sample surface deteriorates. The minimum thickness for samples to separate is about 300 µm. In order to guarantee separation and controle material wear in the reactor we targeted a total thickness of about 700 µm. With a top-layer growth time of 5 h, we achieved a total thickness of 670 µm.

Fig. 4: Photography of whole self-separated, freestanding GaN-wafer.

The thick GaN layer separated in one piece as can be seen in Fig. 4. During growth, some cracks appeared in the material, but could be overgrown in the following process. The

sapphire substrate broke into pieces after separation of the top layer.

Table 1: Growth parameters.

Growth step	Temp. (°C)	NH_3 (sccm)	HCl over Ga (sccm)	Time (min)
3D Growth	950	1000	10	10
2D Growth	1050	3000	10	105
Standard Growth	1050	2300	30	300

In Fig. 5, we see a curvature profile, measured by x-ray diffraction on a line parallel to the wafer flat, through the wafer center. Here we can see the effect of the curvature controle in the template as described in [11]. The minimum curvature measured is 230 km^{-1}, which is well below the value for non curvature controlled samples with a thickness of 670 µm, which lies at about 650 km^{-1}.

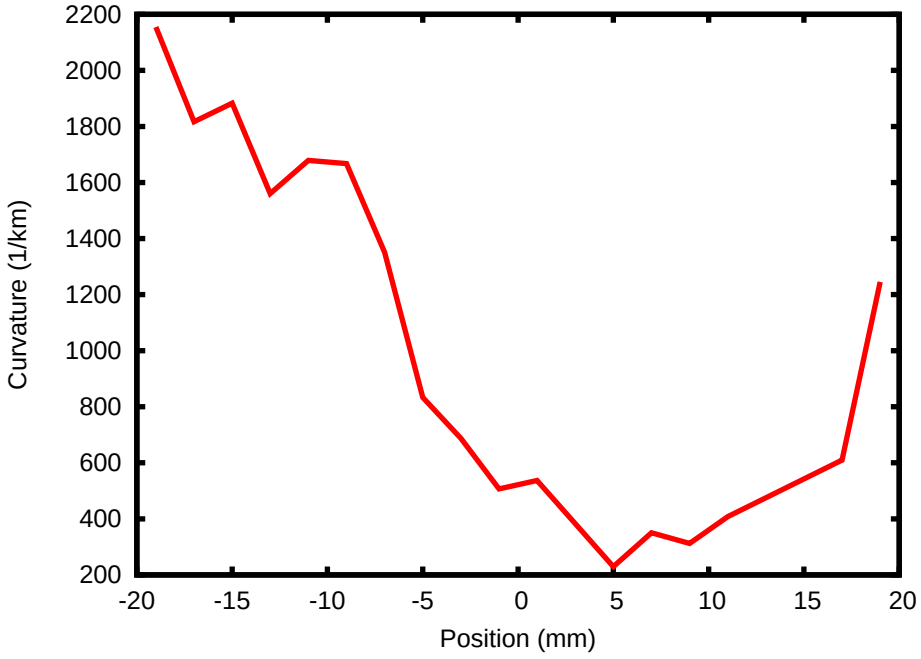

Fig. 5: Curvature profile of whole self-separated, freestanding GaN-wafer.

Low temperature photoluminescence (PL) of a samples grown with this technique shows a full width at half maximum (FWHM) of the D^0X emission of 1.6 meV (Fig. 6). X-ray diffraction (XRD) rocking curve FWHM of the 002 GaN peak can be fitted to 16 arcseconds at the point of the lowest curvature for the full 2 inch freestanding sample shown in Fig. 5. The XRD measurement has been carried out with an open detector and an incoming beam size of 1 mm by 0.05 mm.

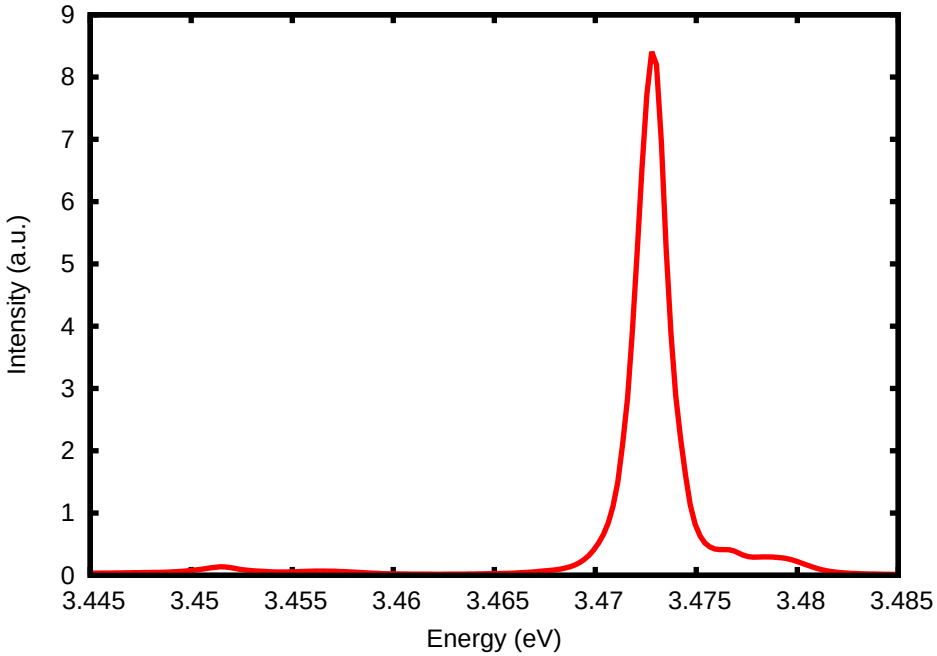

Fig. 6: Low temperature photoluminescence at 14 K of self-separated, freestanding GaN-layer.

5. Summary

We were able to find working growth conditions to overgrow a silicon nitride mask with 3D structures in the HVPE process. Next, we established a process to planarize these three-dimensional structures to regain a flat surface with a low defect density. By increasing the thickness of this template, we were able to get a self-separated, freestanding GaN-layer. With this process we are able to reduce the complexity of the self-separation process as only one MOVPE step is remaining to create the template. Additionally, stable self-separation could be achieved, which has not been the case with the intermediate MOVPE growth-step.

Acknowledgment

I thank R. Gull, R. Leute and D. Heinz for preparing the templates, T. Meisch for fruitful discussions concerning growth and B. Neuschl for measuring PL. This work was financially supported by the german Federal Ministry of Education and Research (BMBF) within the “TeleGaN” project.

References

[1] R. Dwilinski, R. Doradzinski, J. Garczynski, L. Sierzputowski, R. Kucharski, M. Zajac, M. Rudzinski, R. Kudrawiec, J. Serafinczuk, and W. Strupinski, “Recent

achievements in AMMONO-bulk method", *J. Cryst. Growth*, vol. 312, pp. 2499–2502, 2009.

[2] S. Nakamura and M.R. Krames, "History of gallium-nitride-based light-emitting diodes for illumination", *Proc. IEEE*, vol. 101, pp. 2211–2220, 2013.

[3] D.J. Meyer, D.A. Deen, D.F. Storm, M.G. Ancona, D.S. Katzer, R. Bass, J.A. Roussos, B.P. Downey, S.C. Binari, T. Gougousi, T. Paskova, E.A. Preble, and K.R. Evans, "High electron velocity submicrometer AlN/GaN MOS-HEMTs on freestanding GaN substrates", *IEEE Electron Dev. Lett.*, vol. 34, pp. 199–201, 2013.

[4] C.R. Miskys, M.K. Kelly, O. Ambacher, and M. Stutzmann, "Freestanding GaN substrates and devices", *Phys. Status Solidi C*, vol. 0, pp. 1627–1650, 2003.

[5] S. Nakamura, M. Senoh, S. Nagahama, N. Iwasa, T. Yamada, T. Matsushita, H. Kiyoku, Y. Sugimoto, T. Kozaki, H. Umemoto, M. Sano, and K. Chocho, "InGaN/GaN/AlGaN-based laser diodes with cleaved facets grown on GaN substrates", *Appl. Phys. Lett.*, vol. 73, pp. 832–834, 1998.

[6] F. Lipski, S.B. Thapa, J. Hertkorn, T. Wunderer, S. Schwaiger, F. Scholz, M. Feneberg, M. Wiedenmann, K. Thonke, H. Hochmuth, M. Lorenz, and M. Grundmann, "Studies towards freestanding GaN in hydride vapor phase epitaxy by in-situ etching of a sacrificial ZnO buffer layer", *Phys. Status Solidi C*, vol. 6, pp. 352–355, 2009.

[7] F. Lipski, T. Wunderer, S. Schwaiger, and F. Scholz, "Fabrication of freestanding 2"-GaN wafers by hydride vapour phase epitaxy and self-separation during cooldown", *Phys. Status Solidi A*, vol. 207, pp. 1287–1291, 2010.

[8] K. Hiramatsu, K. Nishiyama, M. Onishi, H. Mizutani, M. Narukawa, A. Motogaito, H. Miyake, Y. Iyechika, and T. Maeda, "Fabrication and characterization of low defect density GaN using facet-controlled epitaxial lateral overgrowth (FACELO)", *J. Cryst. Growth*, vol. 221, pp. 316–326, 2000.

[9] Y. André, A. Trassoudaine, J. Tourret, R. Cadoret, E. Gil, D. Castelluci, O. Aoude, and P. Disseix, "Low dislocation density high-quality thick hydride vapour phase epitaxy (HVPE) GaN layers", *J. Cryst. Growth*, vol. 306, pp. 86–93, 2007.

[10] O. Chelda-Gourmala, A. Trassoudaine, Y. André, S. Bouchoule, E. Gil, J. Tourret, D. Castelluci, and R. Cadoret, "Complete HVPE experimental investigations: Cartography of SAG GaN towards quasi-substrates or nanostructures", *J. Cryst. Growth*, vol. 312, pp. 1899–1907, 2010.

[11] M. Klein, "Influencing the bow of thick hydride vapor phase epitaxial GaN by prestraining MOVPE templates", *Annual Report 2012*, pp. 83–90. Ulm University, Institute of Optoelectronics, 2012.

Improvement of MOVPE Grown (11$\bar{2}$2) Oriented GaN on Pre-Structured Sapphire Substrates Using a SiN_x Interlayer and HVPE Overgrowth

Marian Caliebe

In this article two methods for improvements of (11$\bar{2}$2) *oriented semipolar GaN grown by MOVPE on pre-structured sapphire substrates are investigated. The integration of a* SiN_x *interlayer helps to obtain a better crystal quality. Also the overgrowth of the MOVPE samples by HVPE is a way to obtain a smoother GaN surface. A high incorporation of oxygen on* (11$\bar{2}$2) *oriented GaN compared to* (0001) *oriented GaN grown by HVPE was observed.*

1. Introduction

Despite longtime research on solid state lighting, there are still a lot of challenges for highly efficient, bright LEDs in the green region of the optical spectrum. In literature, this problem is referred to as the green gap. The high indium concentrations that are required for long-wavelength emission of GaN based devices give rise to strain in the piezoelectric material. This is caused by the significant lattice mismatch between GaN and the active GaInN quantum wells. This results in defects that increase the nonradiative recombination rate and high internal electric fields that lead to the so-called quantum-confined Stark effect (QCSE). Using semipolar crystal planes with reduced internal polarization fields, the impact of the QCSE might be reduced [1–5].

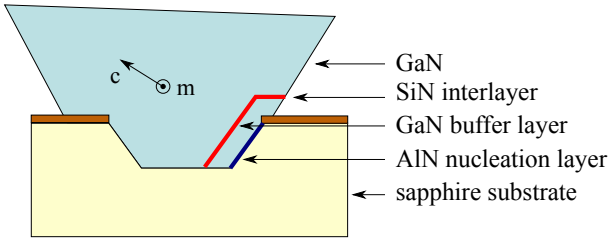

Fig. 1: Schematic structure of a single GaN stripe nucleating on the c-plane-like side facet of the etched trench. Structures grown on r-plane pre-structured sapphire wafers eventually coalesce to a closed layer with a (11$\bar{2}$2) semipolar surface.

This article [6] concentrates on our studies of semipolar (11$\bar{2}$2) oriented GaN grown by MOVPE on r-plane (10$\bar{1}$2) pre-structured sapphire substrates (r-PSS). The growth of a semipolar (11$\bar{2}$2) GaN layer on the sidewall of an r-PSS was first demonstrated by Okada

et al. [7]. The investigated approach is sketched in Fig. 1: At first, a SiO_2 mask is deposited for selective epitaxy. Trenches are etched along a-direction into the sapphire substrates. One facet of the trenches is c-plane like. On these facets, GaN stripes grow in c-direction and finally coalesce to a closed semipolar layer.

A known method for the reduction of defects in conventional c-plane GaN is the in-situ integration of SiN_x interlayers [8–12]. This method is a special case of epitaxial lateral overgrowth (ELOG) [13] and has been studied extensively by our group on c-oriented GaN [14, 15] and AlGaN layers [16, 17]. It has been adopted successfully also to the structures described above [18]. Further investigations are presented in this article.

In another experiment, the MOVPE samples have been overgrown by hydride vapor phase epitaxy (HVPE).

2. Template Preparation and MOVPE Growth Conditions

The r-plane sapphire substrates are structured as described by S. Schwaiger [19]. At first the growth mask, a 200 nm thick SiO_2 layer, is deposited with PECVD on the bare r-plane sapphire wafer. By conventional photolithography, resist stripes with a period of 6 µm and a width of 3 µm are manufactured and an etch mask containing Ni is deposited. After lift-off, the trenches are etched by RIE using the gases Ar, BCl_3 and Cl_2. The remains of the metal mask are removed wet chemically.

GaN growth by MOVPE is carried out in a commercial Aixtron-200/4 RF-S HT reactor with the precursors TMGa, NH_3 and TMAl. Growth starts with the deposition of an AlN:O nucleation layer. A GaN buffer layer follows at 1105°C and a V/III ratio of 650. After 10 min, at a distance of approximately 1.2 µm from the c-facet, GaN growth is paused for the deposition of an in-situ SiN_x interlayer that is formed with the precursor SiH_4. The main GaN layer grows at 1025°C for 110 minutes at a V/III ratio of 647.

3. SiN_x Interlayer

In order to investigate the influence of different parameters for SiN_x deposition on the final GaN layer quality, the following experiments have been conducted:

At first, one sample without SiN_x interlayer and three samples with SiN_x interlayer, deposited at 1005°C, 1025°C and 1045°C, for 3 min, at a molar SiH_4 flux of 0.1 µmol min^{-1}, were produced. For all samples, the GaN growth temperature was unchanged. It is assumed that these conditions result in a submonolayer thickness of SiN_x.

In a next step, we have studied various thicknesses of the SiN_x interlayer by varying the deposition time between 2 and 7 minutes at a deposition temperature of 1025°C.

To eliminate the influence of variations of the sapphire templates that are caused by variations at processing, this study was performed on quarters of two 2” wafers. Here, samples from the same wafer are labeled series S1 and series S2, respectively.

Finally the influence of the position of the SiN_x interlayer was surveyed by varying the growth time of the subjacent GaN buffer layer. On one quarter of the used sapphire

wafer, the SiN_x was deposited directly on the nucleation layer. Then the SiN_x interlayer was deposited after 5 min, 7.5 min and, as a reference, again after 10 min. Here, a SiN_x deposition time of 5 min at 1025°C was chosen.

3.1 Results

To compare the crystal quality, the full width at half maximum (FWHM) of high-resolution X-ray diffraction rocking curves (HRXRD RCs) was evaluated (Fig. 2 (left)). The smallest FWHM of this series was found for the symmetric $(11\bar{2}2)$ reflection, measured parallel to the sapphire trenches, at a deposition temperature of 1005 °C. However, its $(11\bar{2}4)$ rocking curve is the broadest of all. If the SiN_x interlayer is deposited at 1025°C, a clear improvement is visible compared to the sample without SiN_x. For higher temperatures an increase of the FWHMs is measured. Low temperature PL spectra (Fig. 5 (left)) show a slight decrease of the intensity of the peak related to basal plane stacking faults (BSF) at 3.42 eV for the SiN_x interlayer deposited at 1025°C. The curves have been normalized with respect to the peak of the donor bound exciton (D^0X) at 3.485 eV. Out-of-plane X-ray diffraction measurements performed at the synchrotron ANKA at Karlsruhe Institute of Technology revealed that similar samples of our group have an excellent stacking fault density with values down to $4.4 \cdot 10^3\,\mathrm{cm}^{-1}$ [20]. We assume that the stacking fault density of the samples investigated in this article is equal or even better. The results of atomic force microscopy (AFM) measurements show that the sample without SiN_x has the lowest roughness (Fig. 2 (right)). Its root mean square (RMS) value is 42 nm on an area of $50 \times 50\,\mu\mathrm{m}^2$. The sample with a deposition temperature of 1025°C has a comparable or only slightly increased RMS value of 53 nm. For higher and lower SiN_x deposition temperatures the surface quality is heavily reduced.

In Fig. 3, the results of the SiN_x deposition time series are depicted. For the FWHMs of HRXRD rocking curves, a minimum can be found at $t = 5$ min. There is no significant change in the surface roughness between 2 and 5 min, but the surface degrades heavily for longer deposition times. Regarding the PL spectra (Fig. 5 (right)), there is no clear relation for the BSF related peak to the deposition time for series S1. However, for series S2 a distinct increase of the BSF related peak with the deposition time is observed.

As can be seen in Fig. 4 a), decreasing the GaN buffer layer thickness leads to an improvement of the FWHM of the $(11\bar{2}2)$ reflection. While the $(11\bar{2}4)$ reflections seems to be unaffected, the here also investigated (0006) reflection has a minimum at 7.5 min and increases again for 5 min. There is no clear change in the AFM RMS value between 5 min and 10 min (Fig. 4 b)). Direct deposition on the nucleation layer leads to both broad RCs and a rough surface.

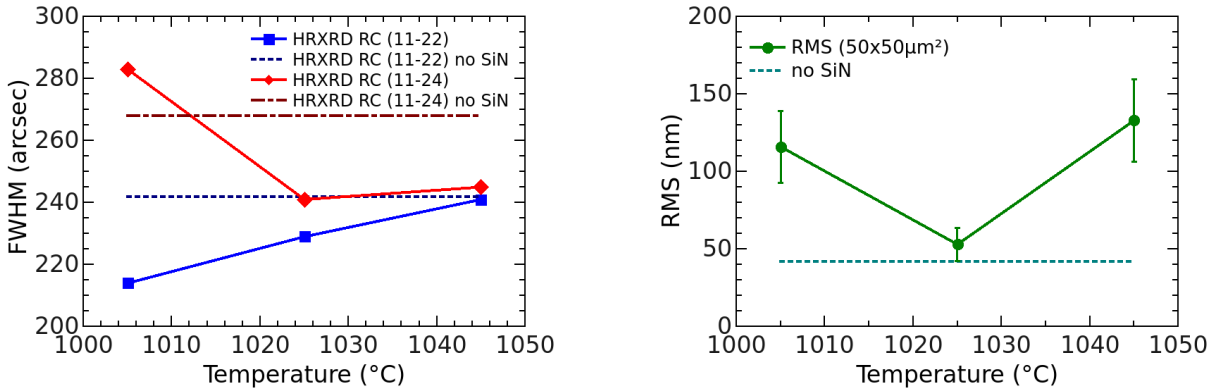

Fig. 2: HRXRD and AFM results of samples with SiN_x interlayer deposited at different temperatures compared to the sample without SiN_x.

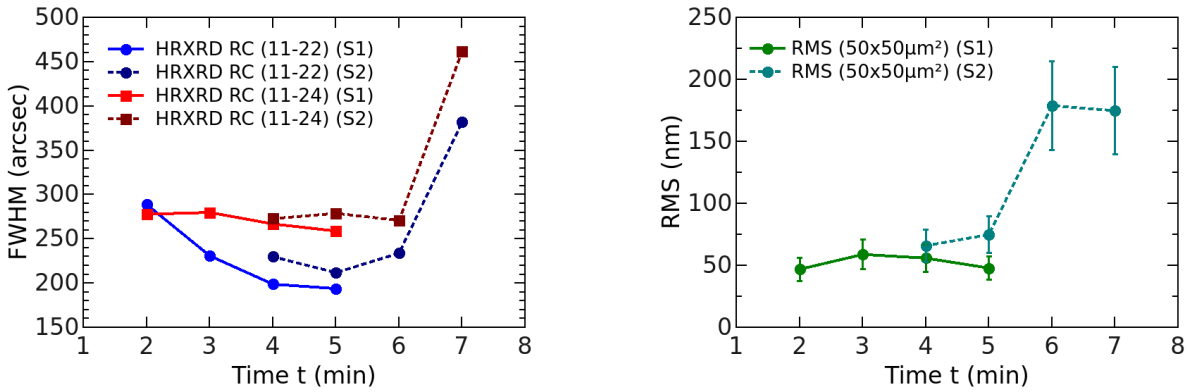

Fig. 3: HRXRD and AFM curves of samples with different deposition time of the SiN_x interlayer. Each series S1 and S2 is from one wafer that has been quartered before epitaxy, respectively.

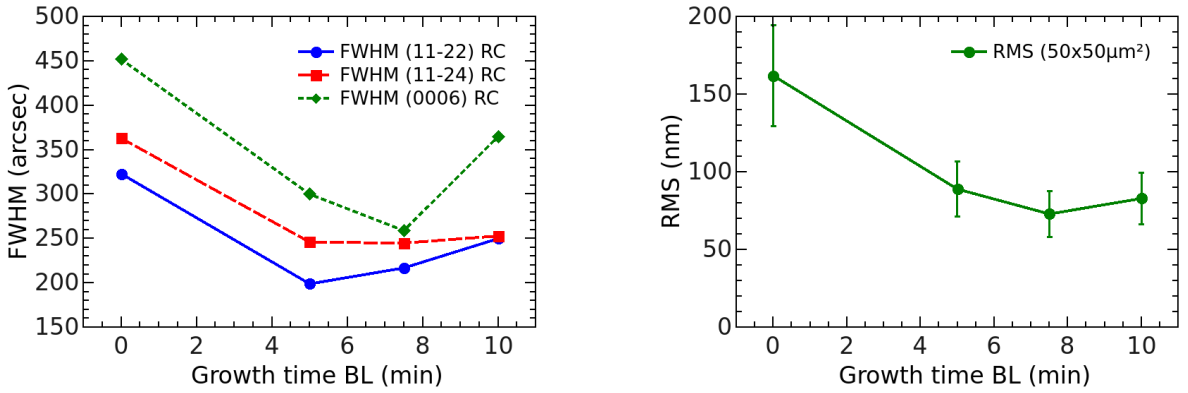

Fig. 4: HRXRD and AFM curves of samples with different positions of the SiN_x interlayer. The time indicates the growth time of the GaN buffer layer below.

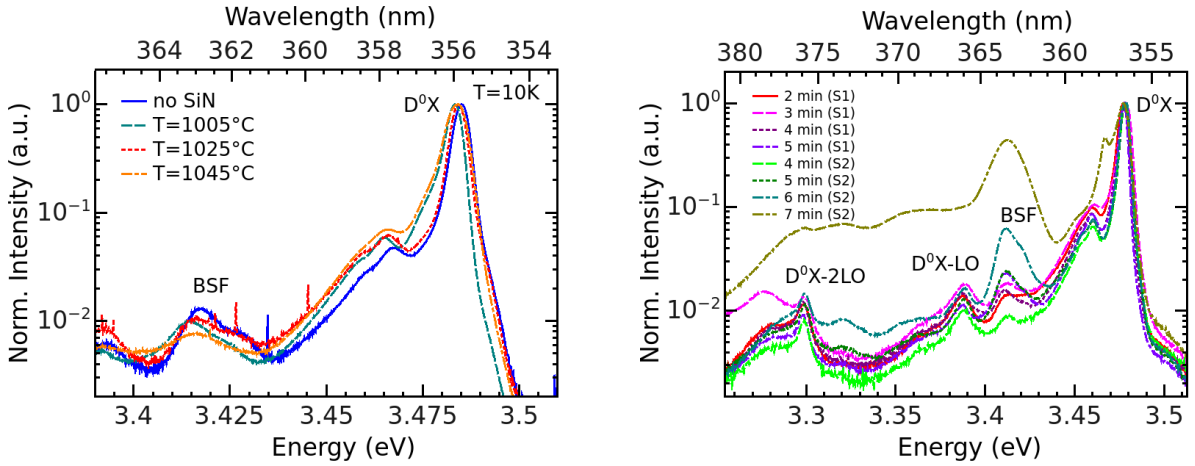

Fig. 5: PL spectra of samples with SiN_x interlayer deposited at different temperatures (left) and different time (right).

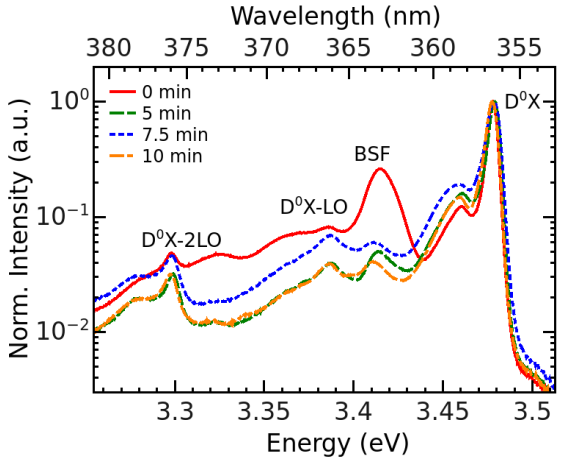

Fig. 6: PL spectra of samples with different positions of the SiN_x interlayer. The time indicates the growth time of the GaN buffer layer below.

Regarding the intensity of the BSF related peak in the PL spectra (Fig. 6), the sample with the interlayer deposited after 10 min is the best. The samples with 5 min and 7.5 min of buffer layer growth seem to have a slightly higher BSF density. Accordant to the HRXRD and AFM results, the sample with SiN_x deposited directly on the nucleation layer leads to the lowest crystal quality. In total, a growth time of 5 min of the GaN buffer layers seems to be the optimum.The AFM image of this sample is shown in Fig. 7.

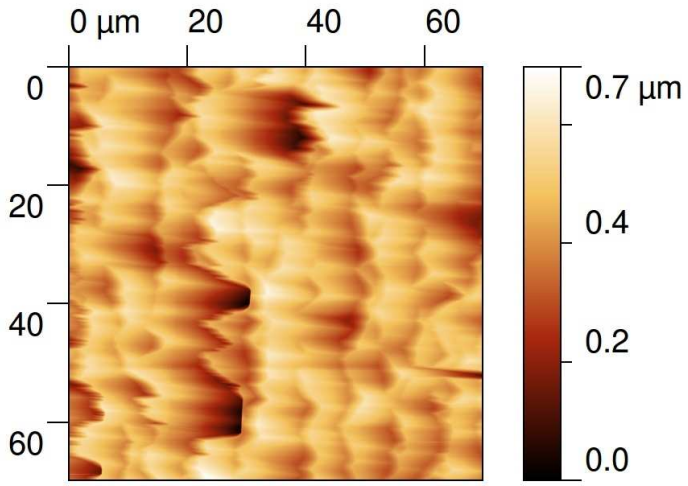

Fig. 7: AFM image of MOVPE grown sample with SiN_x interlayer deposited at 1025 °C, for 5 min after 5 min of buffer layer growth. The individual stripes have coalesced to a closed layer.

4. HVPE Overgrowth

Subsequently, we have overgrown a $(11\bar{2}2)$ MOVPE sample by hydride vapor phase epitaxy (HVPE) at our optimized c-plane conditions at a temperature of $T = 1069$°C. The growth starts at a V/III ratio of 1150 for 30 s. The main HVPE layer is deposited at a V/III ratio of 77 for 30 min. Then, for the last 10 min, the V/III ratio is increased to 230. At the end the V/III ratio is increased to promote 2D growth on a microscopic scale. The thickness of the obtained HVPE layer was approximately 46 µm. The FWHM of HRXRD rocking curves are 215" for the $(11\bar{2}2)$ and 236" for the $(11\bar{2}2)$ reflection, respectively. The surface roughness, measured by AFM (Fig. 9), dropped considerably to 14 nm on a measured area of $50 \times 50\,\mu m^2$.

By van der Pauw Hall experiments, a high carrier density of $n \approx 3 \cdot 10^{19}\,cm^{-3}$ was measured in such HVPE layers, whereas c-oriented samples grown under identical conditions show a carrier density of only $n \approx 2 \cdot 10^{16}\,cm^{-3}$. Secondary ion mass spectrometry (SIMS), performed on the $(11\bar{2}2)$ oriented sample, reveals a high oxygen concentration of $1 \cdot 10^{19}\,cm^{-3}$ similar as observed by M. Amilusik et al. on other semipolar planes [22] hence confirming the results of the van der Pauw measurement. In Fig. 8 the normalized PL spectra of the two HVPE grown samples are depicted. The high-energy shoulder at the $(11\bar{2}2)$ sample is the result of the high carrier concentration, and is caused by the free electron recombination band (FERB) [23].

5. Conclusions

The studies presented here have shown that the integration of an in-situ deposited SiN_x interlayer helps to improve the crystal quality of our semipolar $(11\bar{2}2)$ GaN layers deposited on patterned sapphire substrates on the possible cost of a slight increase of the

surface roughness. PL measurements reveal a small decrease of the basal plane stacking fault density. We obtained best results at a deposition temperature of 1025°C and a deposition time of 5 min after 5 min growth time of the GaN buffer layer.

Overgrowing the MOVPE samples by HVPE results in a heavy reduction of the surface roughness. Compared to c-plane GaN, $(11\bar{2}2)$ oriented samples show a favored incorporation of oxygen during growth that results in a high n-carrier concentration and a considerable signal above 3.5 eV in PL measurements that is induced by the free electron recombination band.

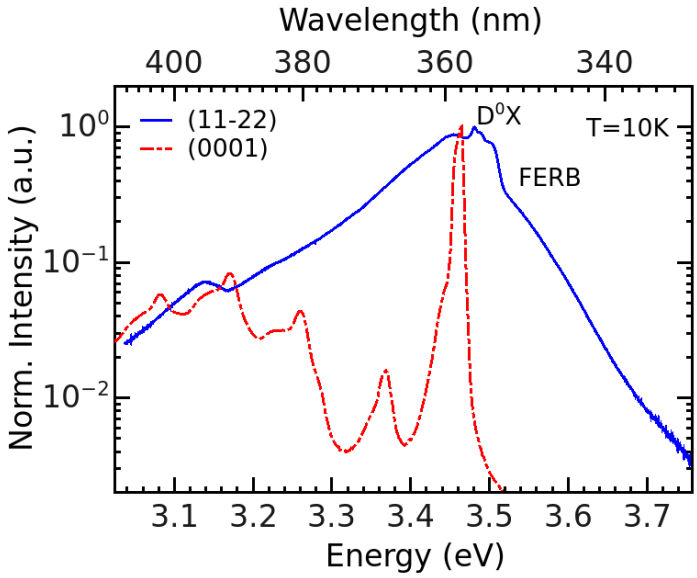

Fig. 8: Normalized low temperature PL spectra of a $(11\bar{2}2)$ and a (0001) oriented HVPE grown GaN sample.

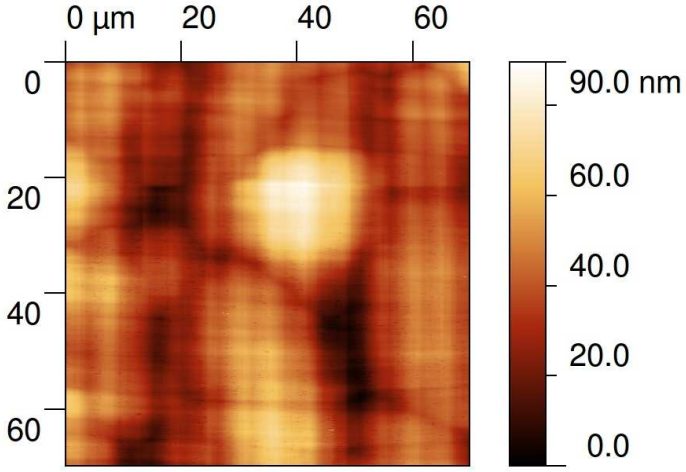

Fig. 9: AFM image of HVPE grown sample. The surface is much smoother and more homogenous compared to the MOVPE grown sample.

Acknowledgment

I gratefully acknowledge the scientific contribution of the coauthors of this article: Tobias Meisch, Martin Klein, Dominik Heinz, and Ferdinand Scholz of the Institute of Optoelectronics, as well as Benjamin Neuschl, Sebastian Bauer, Jeffrey Helbing, Dominik Beck, and Klaus Thonke of the Institute of Quantum Matter, Semiconductor Physics Group at Ulm University. Also we acknowledge the technical contributions of R. Rösch and I. Schwaiger of the Institute of Optoelectronics, and we thank M. Mohr and B. Riedmüller of the Institute of Micro and Nanomaterials at Ulm University for their support in AFM measurements. For out-of-plane X-ray diffraction measurements we thank S. Lazarev and S. Bauer of the Synchrotron Facility ANKA at Karlsruhe Institute of Technology (KIT). We also like to thank L. Kirste of Fraunhofer Institute for Applied Solid State Physics (IAF) for SIMS measurements. Further we would like to thank R. A. R. Leute for fruitful discussions.

This work was financially supported by the European Commission (FP7) within the framework of the project "AlGaInN materials on semi-polar templates for yellow emission in solid state lighting applications" (ALIGHT) and by the Deutsche Forschungsgemeinschaft (DFG) within the framework of the project "Polarization Field Control in Nitride Light Emitters" (PolarCoN).

References

[1] F. Bernardini, V. Fiorentini, and D. Vanderbilt, "Spontaneous polarization and piezoelectric constants of III-V nitrides", *Phys. Rev. B*, vol. 56, pp. R10024–R10027, 1997.

[2] O. Ambacher, "Growth and applications of group III-nitrides", *J. Phys. D: Appl. Phys.*, vol. 31, pp. 2653–2710, 1998.

[3] T. Takeuchi, H. Amano, and I. Akasaki, "Theoretical study of orientation dependence of piezoelectric effects in wurtzite strained GaInN/GaN heterostructures and quantum wells", *Jpn. J. Appl. Phys.*, vol. 39, pp. 413–416, 2000.

[4] A.E. Romanov, T.J. Baker, S. Nakamura, and J.S. Speck, "Strain-induced polarization in wurtzite III-nitride semipolar layers", *J. Appl. Phys.*, vol. 100, pp. 023522-1–10, 2006.

[5] F. Scholz, T. Wunderer, B. Neubert, F. Feneberg, and K. Thonke, "GaN-based light-emitting diodes on selectively grown semipolar crystal facets", *MRS Bulletin*, vol. 34, pp. 328–333, 2009.

[6] M. Caliebe, T. Meisch, B. Neuschl, S. Bauer, J. Helbing, D. Beck, K. Thonke, M. Klein, D. Heinz, and F. Scholz, "Improvements of MOVPE grown $(11\bar{2}2)$ oriented GaN on pre-structured sapphire substrates using a SiN_x interlayer and HVPE overgrowth", *Phys. Status Solidi C*, 2013, DOI: 10.1002/pssc.201300527.

[7] N. Okada, A. Kurisu, K. Murakami, and K. Tadatomo, "Growth of semipolar (11-22) GaN layer by controlling anisotropic growth rates in r-plane patterned sapphire substrate", *Appl. Phys. Express*, vol. 2, pp. 091001-1–3, 2009.

[8] P. Vennégues, B. Beaumont, S. Haffouz, M. Vaille, and P. Gibart, "Influence of in situ sapphire surface preparation and carrier gas on the growth mode of GaN in MOVPE", *J. Cryst. Growth*, vol. 187, pp. 167–177, 1998.

[9] S. Sakai, T. Wang, Y. Morishima, and Y. Naoi, "A new method of reducing dislocation density in GaN layer grown on sapphire substrate by MOVPE", *J. Cryst. Growth*, vol. 221, pp. 334–337, 2000.

[10] S. Tanaka, M. Takeuchi, and Y. Aoyagi, "Anti-surfactant in III-nitride epitaxy — quantum dot formation and dislocation termination—", *Jpn. J. Appl. Phys.*, vol. 39, pp. L831–L834, 2000.

[11] O. Contreras, F.A. Ponce, J. Christen, A. Dadgar, and A. Krost, "Dislocation annihilation by silicon delta-doping in GaN epitaxy on Si", *Appl. Phys. Lett.*, vol. 81, pp. 4712–4714, 2002.

[12] K.J. Lee, E.H. Shin, and K.Y. Lim, "Reduction of dislocations in GaN epilayers grown on Si(111) substrate using Si_xN_y inserting layer", *Appl. Phys. Lett.*, vol. 85, pp. 1502–1504, 2004.

[13] B. Beaumont, P. Vennégues, and P. Gibart, "Epitaxial lateral overgrowth of GaN", *Phys. Status Solidi B*, vol. 227, pp. 1–43, 2001.

[14] J. Hertkorn, P. Brückner, S. Thapa, T. Wunderer, F. Scholz, M. Feneberg, K. Thonke, R. Sauer, M. Beer, and J. Zweck, "Optimization of nucleation and buffer layer growth for improved GaN quality", *J. Cryst. Growth*, vol. 308, pp. 30–36, 2007.

[15] J. Hertkorn, F. Lipski, P. Brückner, T. Wunderer, S. Thapa, F. Scholz, A. Chuvilin, U. Kaiser, M. Beer, and J. Zweck, "Process optimization for the effective reduction of threading dislocations in MOVPE grown GaN using in situ deposited SiN_x masks", *J. Cryst. Growth*, vol. 310, pp. 4867–4870, 2008.

[16] K. Forghani, M. Klein, F. Lipski, S. Schwaiger, J. Hertkorn, R.A.R. Leute, F. Scholz, M. Feneberg, B. Neuschl, K. Thonke, O. Klein, U. Kaiser, R. Gutt, and T. Passow, "High quality AlGaN epilayers grown on sapphire using SiN_x interlayers", *J. Cryst. Growth*, vol. 315, pp. 216–219, 2011.

[17] K. Forghani, M. Gharavipour, M. Klein, F. Scholz, O. Klein, U. Kaiser, M. Feneberg, B. Neuschl, and K. Thonke, "In-situ deposited SiN_x nanomask for crystal quality improvement in AlGaN", *Phys. Status Solidi C*, vol. 8, pp. 2063–2065, 2011.

[18] T. Meisch, S. Schörner, S. Metzner, M. Caliebe, P. Schustek, and F. Scholz, "Optimization studies on semipolar GaN layers grown on 2" wafers", *Int. Workshop on Nitride Semicond., Sapporo, Japan, Poster MoP-GR-9*, 2012.

[19] S. Schwaiger, *Gasphasenepitaxie und Eigenschaften von nicht- und semipolarem GaN*, Ph.D. Thesis, Ulm University, Ulm, Germany (Cuvillier, Göttingen) 2011.

[20] S. Lazarev, S. Bauer, T. Meisch, M. Bauer, I. Tischer, M. Barchuk, K. Thonke, V. Holy, F. Scholz, and T. Baumbach, "Three-dimensional reciprocal space mapping of diffuse scattering for the study of stacking faults in semipolar $(11\bar{2}2)$ GaN layers grown from the sidewall of an r-patterned sapphire substrate", *J. Appl. Cryst.*, vol. 46, pp. 1425–1433, 2013.

[21] P. Brückner, F. Habel, and F. Scholz, "HVPE growth of high quality GaN layers", *Phys. Status Solidi C*, vol. 3, pp. 1471–1474, 2006.

[22] M. Amilusik, T. Sochacki, B.L. Lucznik, M. Bockowski, M. Fijałkowski, and I. Grzegory, "Homoepitaxial HVPE-GaN growth on non-polar and semi-polar seeds", poster at *17th International Conference on Crystal Growth and Epitaxy, ICCGE*, Warsaw, Poland, Aug. 2013.

[23] E.M. Goldys, T. Paskova, I.G. Ivanov, B. Arnaudov, and B. Monemar, "Direct observation of large-scale nonuniformities in hydride vapor-phase epitaxy-grown gallium nitride by cathodoluminescence", *Appl. Phys. Lett.*, vol. 73, pp. 3583–3585, 1998.

Crystal Quality Improvement of Semipolar ($20\bar{2}1$) GaN on Patterned Sapphire Substrates by In-Situ Deposited SiN Mask

Tobias Meisch

We present our results of ($20\bar{2}1$) *GaN growth on* ($22\bar{4}3$) *patterned sapphire substrates. The substrates are patterned by etching trenches with c-plane-like side-facets. On these facets, the metalorganic vapor phase epitaxy (MOVPE) GaN growth starts in c-direction and forms triangularly shaped stripes eventually coalescing to a* ($20\bar{2}1$) *oriented layer. X-ray rocking curves measured parallel to the stripes of the symmetric* ($20\bar{2}1$) *reflection show a full width at half maximum of 675 arcsec. Well known from epitaxy of c-plane GaN, an in-situ-deposited SiN mask could help to reduce the defect density further. Systematic investigations of the deposition time and position of the SiN interlayer resulted in a significant improvement of crystal quality confirmed by X-ray and low temperature photoluminescence measurements. Additionally, MOVPE GaN templates with and without SiN mask were overgrown by hydride vapor phase epitaxy. Also now, the SiN interlayer improves the crystal and especially the surface quality of the HVPE layer.*

1. Introduction

Most of the common optoelectronic devices based on group III nitrides emitting in the visible and ultraviolet range are grown in the well-known c-direction. Lots of techniques are investigated already to achieve excellent crystal quality and smooth surfaces. Nevertheless, the crystal symmetry of the group III nitrides causes strong piezoelectric fields in heterostructures like InGaN/GaN, leading to a bending of the valence and conduction band. The wave functions of electrons and holes get spatially separated and the recombination probability is significantly reduced [1]. Furthermore, the effective band gap decreases resulting in a redshift of the emission spectrum. This behavior is known as Quantum Confined Stark Effect (QCSE). To reduce or even avoid these internal piezoelectric fields, the growth in non-c-directions has been proposed. The epitaxy of nonpolar GaN (perpendicular to the c-axis) is typically dominated by a poor crystal quality. Choosing semipolar directions like ($11\bar{2}2$), ($10\bar{1}1$) or ($20\bar{2}1$) seems to be a good compromise between a reasonable crystal quality and a reduced QCSE. For these particular directions, the amount of the piezoelectric field is reduced to a quarter as compared to c-plane and additionally, the field direction is inverted. Therefore, an externally applied voltage counteracts the internal field and hence reduces the band bending. In particular, the ($20\bar{2}1$) orientation has been found to be most appropriate for such optoelectronic devices [2]. However, the epitaxy of ($20\bar{2}1$) GaN seems to be a big challenge. Typically, ($20\bar{2}1$) GaN

templates are produced by cutting thick c-plane wafers grown by HVPE, which results in wafers limited in size to just a few square mm [3]. This limitation can be overcome by growing such GaN layers on foreign substrates like sapphire or silicon with uncommon orientations. Similar as reported by Okada et al. [4], we are able to grow $(20\bar{2}1)$ GaN layers on $(22\bar{4}3)$ patterned sapphire substrates with a reasonable crystal quality. By etching trenches into these wafers, c-plane-like sidewalls are formed on which the growth of GaN starts developing triangular shaped stripes. After a suitable growth time, these stripes hopefully coalesce and form a planar $(20\bar{2}1)$ oriented surface (Fig. 1). By this procedure, we make use of the well-established growth in c-direction, eventually resulting in a semipolar surface. This approach offers some essential advantages: First, the growth of a full LED or laser diode structure in a single epitaxy run is possible. Moreover, the diameter of the template is just limited by the reactor size. In our studies, 2“ diameter sapphire wafers were used. Well-known from the growth of c-plane GaN, a SiN mask can

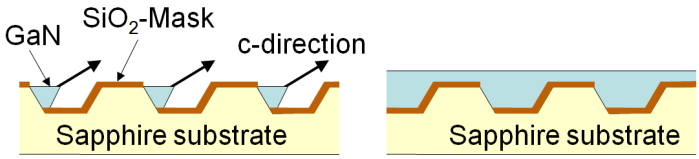

Fig. 1: Patterned sapphire substrate, schematically. All non-c-plane facets are covered with SiO_2 (brown) avoiding parasitic growth. The GaN nucleates on the c-plane sidewall, forms triangular-shaped stripes (left) and coalesces after a suitable growth time to a closed semipolar surface (right).

help to stop defects penetrating to the surface and therefore reduce the defect density in the subsequent layers significantly. This SiN layer can be deposited in-situ in the MOVPE reactor. Silane (SiH_4) reacts with ammonia (NH_3) to a SiN layer, less than an atomic layer thick. As a result, the layer is not completely closed and thereby acts as a mask. As shown in Fig. 2, the top of a GaN layer gets covered with this SiN layer. Some defects are stopped by the mask itself. By pushing the GaN growth in c-direction (3D growth), the residual defects get bent to the side. The subsequent coalescence of the three-dimensional structures leads to a closed layer with a drastically reduced defect density. Based on the excellent results of this in-situ deposited interlayer during the growth of c-plane GaN [5], we transferred this technique to the epitaxy of semipolar $(20\bar{2}1)$ GaN. In order to achieve an optimal crystal quality, the position and deposition time of the SiN interlayer are varied systematically. Additionally, we studied the overgrowth of such layers by hydride vapor phase epitaxy (HVPE) to improve the layer quality further and to observe the influence of the SiN mask on these thick layers.

2. Experimental

2.1 Metal organic chemical vapor phase epitaxy

At the beginning of the structuring process, a nickel reflection layer for the subsequent photolithography steps is evaporated onto the sapphire wafer. A stripe mask with an

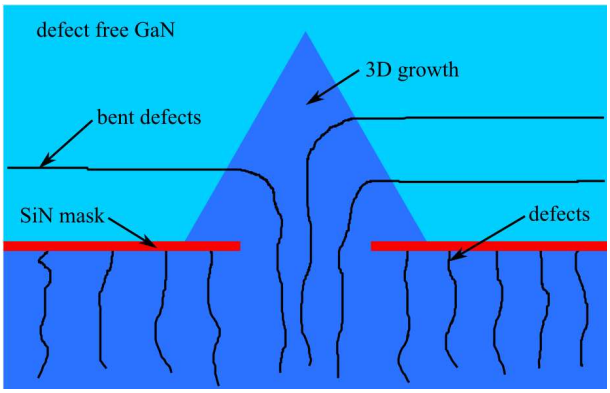

Fig. 2: Schematic illustration of the action of a SiN mask reducing the defect density in the subsequent GaN overgrowth.

opening of 3 µm and a period of 6 µm patterns the positive photoresist accordingly. By evaporation of an about 500 nm thick nickel layer and a subsequent lift-off process, a relatively stable etching mask is formed. Via reactive ion etching, the stripes get transferred into the sapphire substrate. Covering all non-c-plane-like facets with SiO_2 (Fig. 1) prevents parasitic growth.

The MOVPE growth was done in a commercial Aixtron-200/4 RF-S HT reactor using the standard precursors ammonia (NH_3), trimethylgallium (TMGa) and trimethylaluminum (TMAl). The growth starts with our about 20 nm thick standard AlN nucleation layer at relatively low temperatures. Choosing higher temperatures at the beginning of GaN growth improves the selectivity. A subsequent reduction of the reactor temperature pushes the growth in c-direction and the GaN stripes can grow out of the sapphire trenches.

The crystal quality of the GaN layers was investigated by high-resolution X-ray diffraction (HRXRD) with a Bruker D8 Discover diffractometer. From low temperature photoluminescence (PL) measurements in a helium cryostat, using a 1000 mm monochromator and a 1200 mm^{-1} grid, we obtained more detailed information about defects close to the crystal surface.

First investigations [6] were done at growth conditions close to the ones suitable for c-plane growth. A poor selectivity of the AlN and the GaN layer on the patterned and masked sapphire wafer was observed. By increasing the growth temperature, the diffusion velocity of the molecules can lead to an enhanced selectivity. Indeed, by setting the temperature of the AlN layer to 1020 °C and the GaN growth temperature to about 1145 °C, we achieved well-formed GaN stripes without any islands (Fig. 3, left). The very top part of the GaN layer was grown at a lower temperature (about 1050 °C) to push the growth rate in c-direction leading to a more lateral growth in order to improve the coalescence. X-ray rocking curve (RC) measurements of the symmetric $(20\bar{2}1)$ reflection indicate a reasonable crystal quality. With the X-ray beam parallel to the stripes, the signal has a full width at half maximum (FWHM) of just 675 arcsec. Perpendicular to the stripes, the FWHM increases to 1470 arcsec. This may be due to a slight statistical tilt of each individual stripe. Surprisingly, the (0002) reflection measured in skew geometry with the X-ray beam parallel to the stripes gives a very narrow peak of just 70 arcsec. As shown in Fig.

3 (right), low temperature PL measurements indicate a defect-dominated crystal surface. Just a very weak signal at 3.459 eV related to D^0X [7] recombination is detectable.

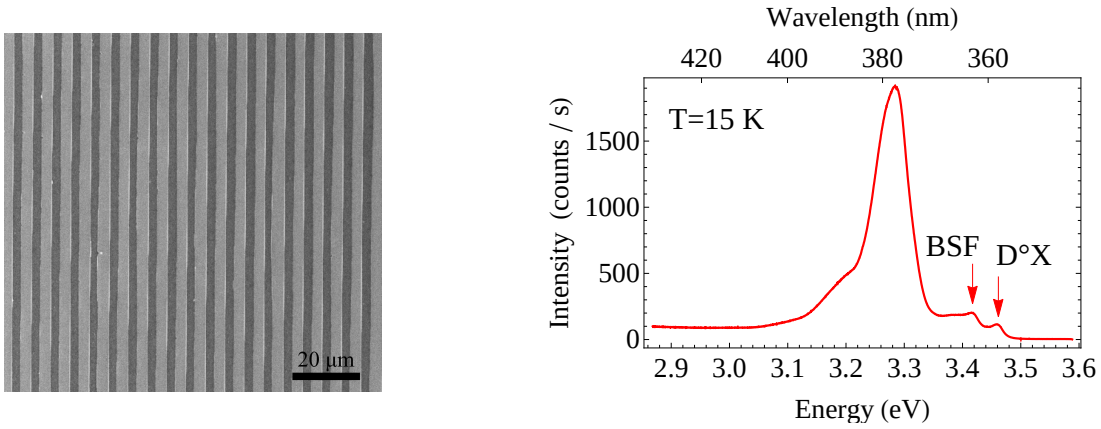

Fig. 3: Left: SEM micrograph of $(20\bar{2}1)$ GaN on $(22\bar{4}3)$ patterned sapphire substrate. High reactor temperature leads to a high selectivity of GaN and results in homogeneous GaN stripes, free of any island growth. Right: Low temperature PL measurements indicate a defect-dominated GaN stripes [8].

As described in the introduction, a SiN interlayer was deposited on top of an about 1 µm thick GaN layer (9:50 min growth, before coalescence of the stripes) to improve the crystal quality further. The deposition time of the SiN mask was systematically varied from 4:30 min to 6:00 min. Subsequently, an about 2 µm thick GaN layer was grown. As shown in Fig. 4 (left), a mask deposited for 4:30 min already seems to improve the crystal quality. X-ray RC measurements of the symmetric $(20\bar{2}1)$ reflection show a peak with a FWHM of 453 arcsec. Increasing the deposition time maskes the SiN mask less porous eventually blocking the nucleation in the pores, which may lead to enhanced polycrystalline nucleation on the SiN mask (Fig. 5). An optimal deposition time was found at 5:00 min. RC measurements of the $(20\bar{2}1)$ reflection give a fairly narrow peak with a FWHM of just 320 arcsec. Low temperature PL measurements confirm an improved crystal quality (Fig. 4, right). The ratio of the D^0X (3.467 eV) and BSF (I_1) (3.405 eV) peak intensities is decreased, compared to the sample without SiN layer. Additionally, the defect related signal at 3.288 eV seem to be significantly suppressed.

The position of the SiN interlayer determines, where the defects running to the surface get stopped. By depositing it far away from the nucleation layer, the defects can already lead to a rough surface (e.g. V-pits). Choosing a position close to the start of the epitaxy, the GaN buffer layer could be strained, which causes new defects after the SiN interlayer again. Therefore, the position of the mask seems to be an important parameter. Consequently, we varied the growth time of the buffer layer systematically from 6:50 to 9:50 min. The deposition time of the SiN layer itself was fixed to 5:30 min. As shown in Fig. 6 (left), the reduction of the buffer layer thickness leads to an improved crystal quality, obviously saturating at about 7–8 min. PL investigations (Fig. 6, right) indicate a clear decrease of the BSF density. Both the intensity of the signal related to BSF (I_1) and the peak related to BSF (E) became weaker as compared to the D^0X intensity.

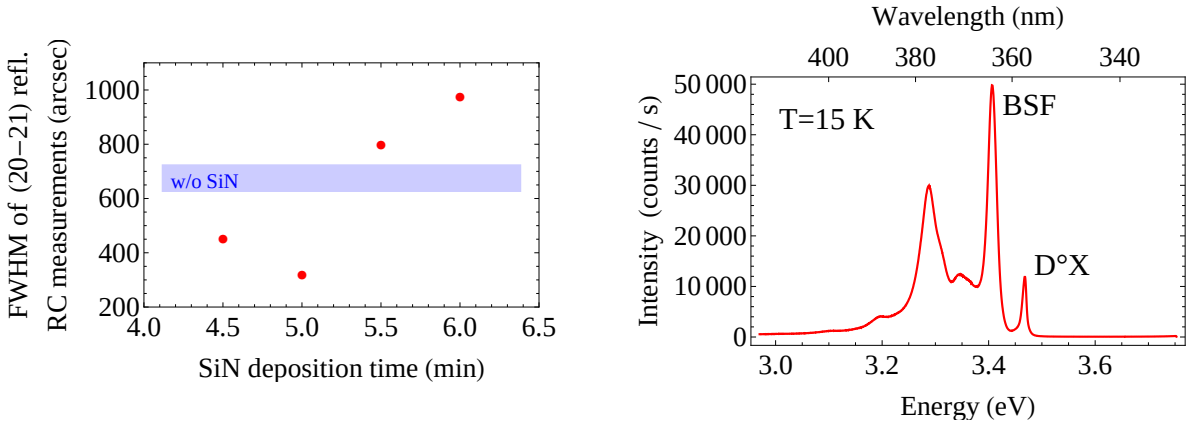

Fig. 4: FWHM of X-ray (20$\bar{2}$1) reflection RC measurements as a function of SiN deposition time. Right: Low temperature PL spectrum of (20$\bar{2}$1) GaN with a SiN deposition time of 5:00 min.

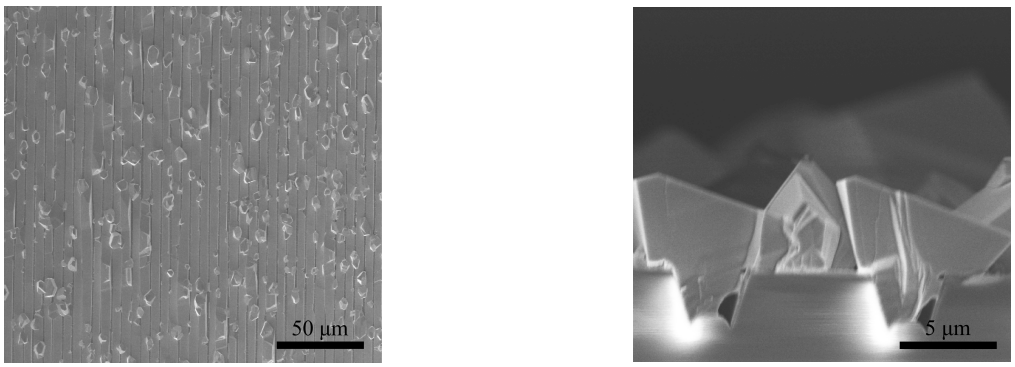

Fig. 5: SEM top-view (left) and cross-section (right) micrograph of (20$\bar{2}$1) GaN with a SiN interlayer, deposited for 6 min showing parasitic polycrystals growing on the surface.

2.2 HVPE overgrowth

Next, we investigated the influence of the SiN interlayer on HVPE overgrowth. The temperature of the hot wall reactor was set to 1070 °C. The GaN HVPE layer was grown for 15 min with a V/III ratio of 77, similar to our c-plane growth conditions [9]. SEM investigations confirm the expected high growth rate of about 160 µm/h (Fig. 7, left) leading to a total layer thickness of about 40 µm. The GaN stripes, still separate after the MOVPE growth, seem to coalesce at the very beginning of the overgrowth process. The surface of the sample without SiN shows flaky structures with a height of about 2 µm (Fig. 7, right). Such structures could be caused by defects penetrating through the surface leading to strong step-bunching effects. The X-ray RC (20$\bar{2}$1) reflection has a FWHM of about 700 arcsec, indicating similar crystal quality as in the MOVPE template. However, PL investigations show a significant decrease of the BSF related signal (Fig. 8, left). At 3.472 eV, an extremely intense and narrow donor-bound excitonic signal with a FWHM of just 5.9 meV is detectable.

In the second run, the MOVPE template with 9:50 min GaN buffer layer growth and 5:00 min SiN deposition time was chosen. The growth conditions were unchanged. SEM

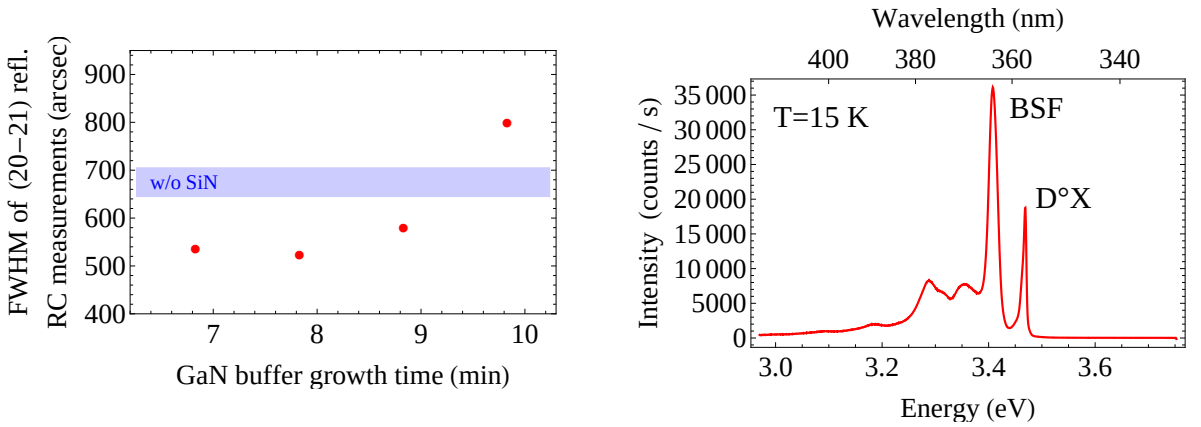

Fig. 6: Left: FWHM of X-ray (20$\bar{2}$1) reflection RC measurements as a function of the GaN buffer layer growth time. Right: Low temperature PL spectrum of (20$\bar{2}$1) GaN with 7:50 min buffer layer growth time and a SiN deposition time of 5:30 min.

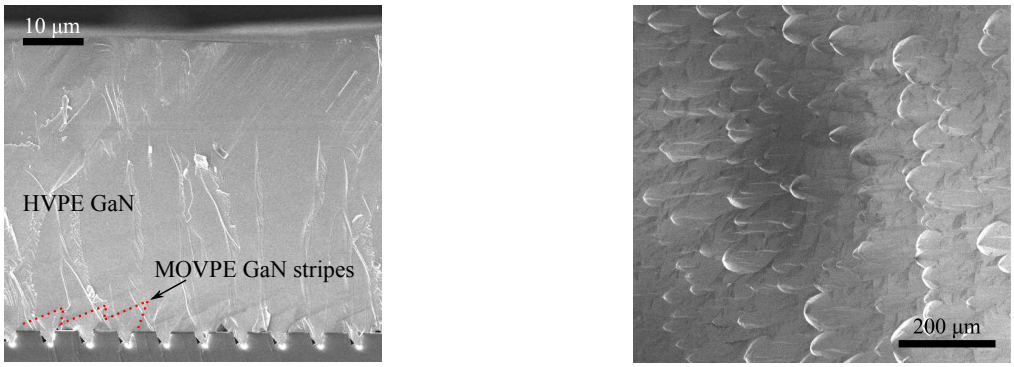

Fig. 7: Left: SEM cross section of (20$\bar{2}$1) HVPE GaN on MOVPE template without SiN interlayer. The MOVPE GaN stripes are marked with a red dashed line (left). The surface shows flaky structures, with a height of about 2 µm (right).

investigations show a clear improvement of the surface quality (Fig. 9). The flakes mentioned above are much less developed. Moreover, the FWHM of the symmetric (20$\bar{2}$1) reflection considerably decreased to 545 arcsec. Low temperature PL measurements confirm a further improvement of crystal quality as compared to the HVPE sample without SiN (Fig. 8, right). The signal at 3.429 eV, related to BSF (I_1), decreases as compared to the D^0X related peak. Therefore, we conclude, that a SiN interlayer in the MOVPE template can help to improve the crystal quality and, in addition, the surface morphology of the HVPE overgrown layer, although the FWHM of the D^0X related signal is slightly increased to 16 meV.

3. Conclusion

Using (22$\bar{4}$3) patterned sapphire substrates, we are able to grow semipolar (20$\bar{2}$1) GaN stripes with a reasonable crystal quality. By inserting a SiN mask as a defect blocking layer, the BSF density in the subsequent GaN layer can be reduced significantly. We

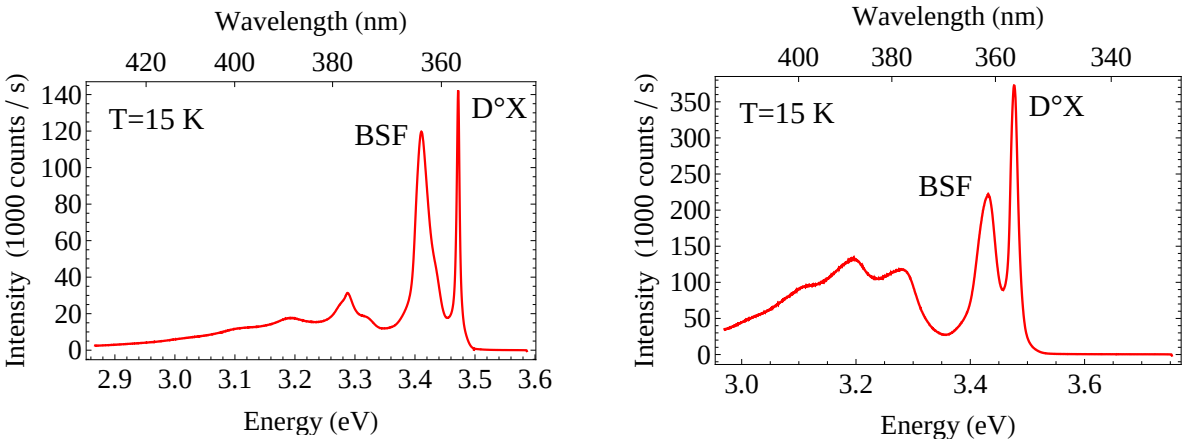

Fig. 8: Low temperature photoluminescence measurements of (20$\bar{2}$1) HVPE GaN without (left) and with (left) SiN interlayer in the MOVPE template.

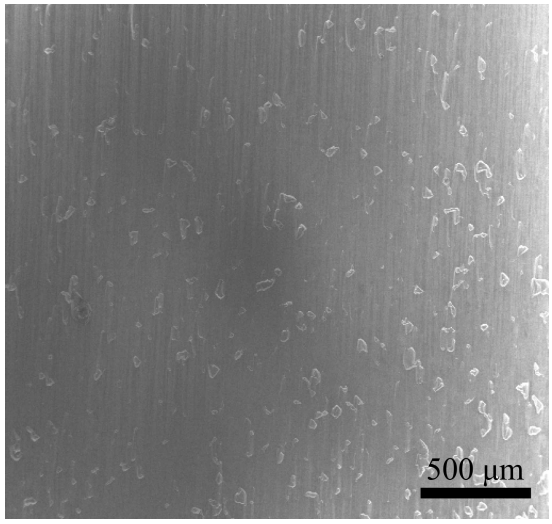

Fig. 9: SEM top-view of (20$\bar{2}$1) HVPE GaN grown on a MOVPE template with SiN interlayer.

investigated the position and the deposition time of the SiN interlayer systematically and found an optimum achieving an excellent crystal quality. X-ray RC measurements of the symmetric (20$\bar{2}$1) reflection show a narrow peak of just 320 arcsec. Low temperature PL measurements confirm the improvements using the SiN mask. By overgrowing the MOVPE sample with a 40 µm HVPE layer, the crystal quality could be further increased. A SiN layer in the corresponding MOVPE template helps to suppress the flaky surface structures of the subsequent HVPE overgrowth.

Acknowledgment

I thank Maryam Alimoradi-Jazi, Benjamin Neuschl, Martin Klein, Ingo Tischer and Klaus Thonke for the intensive cooperation. Furthermore, I thank Ilona Schwaiger, Rudolf Rösch, Johannes Wagner and Rainer Blood for the technical support. All the fruitful

discussions with Robert Leute and Junjun Wang are gratefully acknowledged.

References

[1] J.S. Im, H. Kollmer, J. Off, A. Sohmer, F. Scholz, and A. Hangleiter, "Reduction of oscillator strength due to piezoelectric fields in GaN/$Al_xGa_{1-x}N$ quantum wells", *Phys. Rev. B*, vol. 57, pp. R9435–R9438, 1998.

[2] Y. Yoshizumi, M. Adachi, Y. Enya, T. Kyono, S. Tokuyama, T. Sumitomo, K. Akita, T. Ikegami, M. Ueno, K. Katayama, and T. Nakamura,"Continuous-wave operation of 520 nm green InGaN-based laser diodes on semi-polar {20-21} GaN substrates", *Appl. Phys. Express*, vol. 2, pp. 092101–092104, 2009.

[3] K. Fujito, S. Kubo, and I. Fujimura, "Development of bulk GaN crystals and nonpolar/semipolar substrates by HVPE", *MRS Bull.*, vol. 34, pp. 313–317, 2009.

[4] N. Okada, H. Oshita, K. Yamane, and K. Tadatomo, "High-quality (20-21) GaN layers on patterned sapphire substrate with wide-terrace", *Appl. Phys. Lett.*, vol. 99, pp. 242103–242105, 2011.

[5] J. Hertkorn, F. Lipski, P. Brückner, T. Wunderer, S.B. Thapa, F. Scholz, A. Chuvilin, U. Kaiser, M. Beer, and J. Zweck, "Process optimization for the effective reduction of threading dislocations in MOVPE grown GaN using in situ deposited SiN_x masks", *J. Cryst. Growth*, vol. 310, pp. 4867–4870, 2008.

[6] T. Meisch, M. Alimoradi-Jazi, M. Klein, and F. Scholz, "(20-21) MOVPE and HVPE GaN grown on 2" patterned sapphire substrates", *Proc. ICNS Washington 2013, accepted for publication in Phys. Status Solidi C*, 2014.

[7] B. Monemar, P.P. Paskov, J.P. Bergman, A.A. Toropov, T.V. Shubina, T. Malinauskas, and A. Usui, "Recombination of free and bound excitons in GaN", *Phys. Status Solidi B*, vol. 245, pp. 1723–1740, 2008.

[8] J. Lähnemann, O. Brandt, U. Jahn, C. Pfüller, C. Roder, P. Dogan, F. Grosse, A. Belabbes, F. Bechstedt, A. Trampert, and L. Geelhaar, "Direct experimental determination of the spontaneous polarization of GaN", *Phys. Rev. B*, vol. 86, pp. 081302–081306, 2012.

[9] F. Lipski, T. Wunderer, S. Schwaiger, and F. Scholz, "Fabrication of freestanding 2"-GaN wafers by hydride vapor phase epitaxy and self-separation during cooldown", *Phys. Status Solidi A*, vol. 207, pp. 1287–1291, 2010.

Mg Doping of 3D Semipolar InGaN/GaN-Based Light Emitting Diodes

Junjun Wang

The effects of different Mg doping concentrations in the main p-GaN layer and the p-GaN capping layer on the electroluminescence (EL) property of three-dimensional (3D) stripe semipolar InGaN/GaN based light emitting diodes (LEDs) were investigated. Secondary ion mass spectrometry (SIMS) analysis revealed the Mg concentration of the 3D semipolar p-GaN, indicating a higher Mg incorporation efficiency on the $\{10\bar{1}1\}$ *facet compared to the* $\{11\bar{2}2\}$ *facet. Low-temperature* μ*-photoluminescence was measured on a series of 3D LED structures varying the Mg doping concentration. For the LEDs with the* $\{10\bar{1}1\}$ *facet, pronounced donor-acceptor-pair (DAP) luminescence at 3.24 eV with characteristic LO-replicas was observed with the molar flow ratio between* Cp_2Mg *and TMGa (*Cp_2Mg*/TMGa) of 0.04 % and 0.06 %. With further increasing* Cp_2Mg*/TMGa of 0.10 % and 0.21 %, the DAP band shifts to a broad band emission at a lower energy presenting the emergence of self-compensation. In contrary, self-compensation was not observed up to* Cp_2Mg*/TMGa of 0.21 % for the LEDs with the* $\{11\bar{2}2\}$ *facet. Thus, the Mg incorporation efficiency on the* $\{10\bar{1}1\}$ *facet is concluded to be higher than that on the* $\{11\bar{2}2\}$ *facet, consistent with the SIMS data. The EL output power is low with a too low* Cp_2Mg*/TMGa of 0.04 % due to the inferior hole injection efficiency and stays almost constant with* Cp_2Mg*/TMGa ranging from 0.06 % until 0.21 % for the 3D LEDs with the* $\{10\bar{1}1\}$ *facet. Since Hall measurement is not applicable and SIMS is difficult on 3D structures, the good range of the hole conductivity for high EL output power could be recorgnized by the line shape of the Mg DAP band. Heavy Mg doping in the p-GaN capping layer is required to achieve good ohmic contact performance.*

1. Introduction

High power InGaN/GaN based green light emitting diodes (LEDs) attract worldwide interest nowadays. However, the efficiency of the InGaN/GaN QWs decreases drastically with increasing emission wavelength. On one hand, this is attributed to the degraded material quality with increasing indium content [1]. On the other hand, owing to the polar character of the nitride semiconductors, the increasing strain in such QWs leads to huge internal electric fields resulting in a local separation of electrons and holes and hence reducing their recombination probability. Consequently, many groups are making efforts to fabricate semipolar/nonpolar InGaN/GaN QW structures following different approaches [2, 3]. Previously, we have demonstrated high quality semipolar LEDs grown on the side-facets of three-dimensional (3D) structures fabricated by selective area growth

(SAG) on c-plane sapphire. This approach yields high material quality and is compatible with large scale production on full 2 inch or even larger wafers [4].

Good p-type GaN conductivity is important to obtain effcient InGaN/GaN LEDs. The p-type conductivity of metalorganic vapor phase epitaxy (MOVPE) grown GaN is achieved by Mg doping following low energy electron irradiation [5] or thermal annealing [6]. The hole concentration is limited to about $2 \times 10^{18}\,\mathrm{cm}^{-3}$ by self-compensation leading to low hole conductivity [7]. Lots of investigations were done for the optimal hole conductivity of c-plane and planar semipolar p-GaN. However, little is known about the 3D semipolar p-GaN since Hall measurement is not applicable and SIMS is difficult on 3D structures. This paper reports the determination of the Mg concentration of 3D semipolar p-GaN – $\{10\bar{1}1\}$ and $\{11\bar{2}2\}$ – via secondary ion mass spectrometry (SIMS) analysis. The line shape of the donor-acceptor-pair (DAP) luminescence measured by low-temperature µ-photoluminescence (LT µ-PL) can be correlated to the hole conductivity qualitatively. Moreover, we worked on optimizing the contact resistivity to our p-doped layers by heavy Mg doping in the p-GaN capping layer in order to achieve an ohmic contact performance.

2. Experimental

Epitaxial growth was carried out in a low pressure MOVPE horizontal reactor using TMGa, TEGa, TMIn, TMAl, Cp_2Mg, SiH_4 and NH_3 as precursors. Firstly, a 3 µm thick high quality GaN layer was grown on c-plane sapphire employing a SiN nanomask layer for defect density reduction [8]. Then, a 200 nm thick SiO_2 layer was deposited on the GaN template by plasma enhanced chemical vapor deposition (PECVD) and removed completely within one quarter of the wafer, patterned into periodic stripes with 10 µm wide masked area and 3 µm wide opening along the crystal directions $\langle 11\bar{2}0\rangle$ and $\langle 10\bar{1}0\rangle$, respectively, within another two quarters of the wafer and patterned into periodic hexagons within the fourth quarter of the wafer via photolithography and dry etching. The structure formed with the epi-mask of the hexagonal pattern is not discussed in this paper. Finally, epitaxial overgrowth was applied on the processed template: On the two quarters of the wafer with the stripe pattern, 3D Si-doped GaN stripes with triangular cross-section and a height of about 8.5 µm were formed. On the semipolar side facets of these stripes, 5 InGaN/GaN quantum wells, a 5 nm thick undoped GaN spacer, 250 nm thick Mg-doped GaN and a thin heavily doped p-GaN capping layer were deposited sequentially to form the complete LED structure. Meanwhile, a c-plane LED structure was grown on the quarter of the wafer without any SiO_2 epi-mask in the same epitaxial run. Following growth, the wafers were annealed in an air atmosphere at 750 °C for 1 min in order to depassivate the Mg acceptors. Imaging SIMS is required to characterize the material composition from an inhomogeneous surface which obviously is the case for the stripe LEDs. The Mg depth profile was measured by imaging SIMS using a finely focused primary ion beam to achieve a lateral resolution of about 150 nm. The sputtering ion beam was oriented in parallel with the GaN-based stripes and with an angle of 45 ° to the sample surface for the two types of stripe LEDs. The EL measurements were done on-wafer with evaporated indium contacts. More details about the fabrication procedure can be found elsewhere [4].

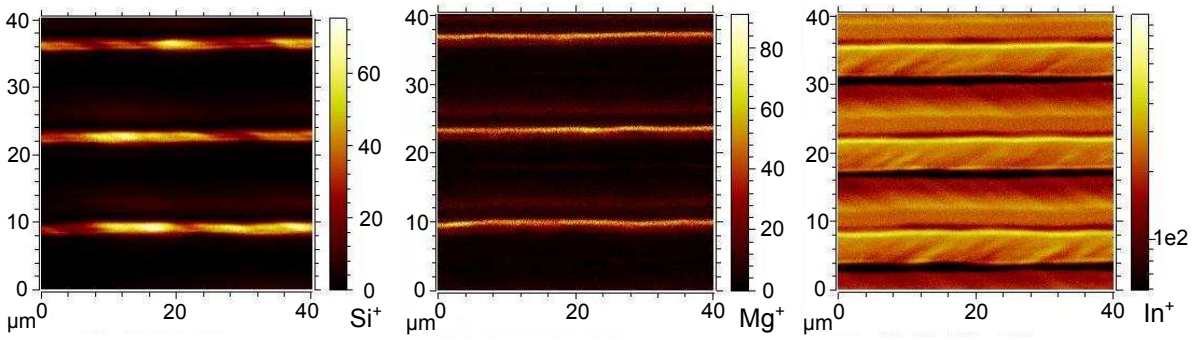

Fig. 1: The SIMS signals of the Si (left), Mg (middle) and In (right) ions integrated over a sputtering depth of 1–2 µm for the stripe LED with the $\{11\bar{2}2\}$ facet ($Cp_2Mg/TMGa = 0.06\,\%$).

3. Results

The chemical Si, Mg and In concentrations of the sample with a molar flow ratio between Cp_2Mg and TMGa ($Cp_2Mg/TMGa$) of 0.06 % during the main p-GaN layer growth were determined by imaging SIMS for the three different structures, c-plane LED and stripe LEDs with the $\{10\bar{1}1\}$ and $\{11\bar{2}2\}$ facets, respectively. The Si, Mg and In signals integrated over a sputtering depth of 1–2 µm are shown in Fig. 1 for the stripe LED with the $\{11\bar{2}2\}$ facet indicating the expected stripe period of 13 µm. Obviously the area with a high Si concentration is the SiO_2 epi-mask between the GaN-based stripes. Within the same area, high Mg and In concentrations are detected, presumably as an artifact of the SIMS measurement. The coexistence of the element Si typically enhances the detected signal intensity of other elements in SIMS measurements. At the stripe tip, a low In concentration is detected opposite to the reported increasing In concentration from the bottom to the tip of the stripes [4]. This is presumably due to the different sputtering behavior there.

The Mg concentration was determined for the stripe LEDs from a rectangular integration area with the size of $1.5 \times 40\,\mu m^2$. The integration window was positioned with the long side parallel to the stripes and in the middle of the stripe facet to avoid the measurement artifacets caused by the SiO_2 epi-mask and the stripe tip. The Mg concentrations in the main p-GaN layer of the stripe LEDs with the $\{10\bar{1}1\}$ and $\{11\bar{2}2\}$ facets and the c-plane LED are $4 \times 10^{19}\,cm^{-3}$, $1.5 \times 10^{19}\,cm^{-3}$ and $1.5 \times 10^{19}\,cm^{-3}$, respectively, for the single wafer with $Cp_2Mg/TMGa = 0.06\,\%$ (Fig. 2). Hence, the Mg incorporation efficiency on the GaN crystal plane $\{10\bar{1}1\}$ is higher than that on $\{11\bar{2}2\}$. The Mg incorporation efficiency is not directly comparable between the planar c-plane and the 3D semipolar structures due to the different surface morphologies.

In order to study the influence of the Mg concentration on the EL performance of the stripe LED with the $\{10\bar{1}1\}$ facet, $Cp_2Mg/TMGa$ was chosen to be 0.04 %, 0.06 %, 0.10 %, 0.15 % and 0.21 % during the main p-GaN layer growth for five samples (samples #1–5). The Mg concentration is expected to depend on the $Cp_2Mg/TMGa$ linearly [9]. The Mg concentrations of samples #1 and #3–5 are estimated to be $3 \times 10^{19}\,cm^{-3}$, $7 \times 10^{19}\,cm^{-3}$, $9 \times 10^{19}\,cm^{-3}$ and $1.3 \times 10^{20}\,cm^{-3}$ based on the Mg concentration of $4 \times 10^{19}\,cm^{-3}$ for sample #2 characterized by imaging SIMS. In order to relate the Mg concentration qualitatively

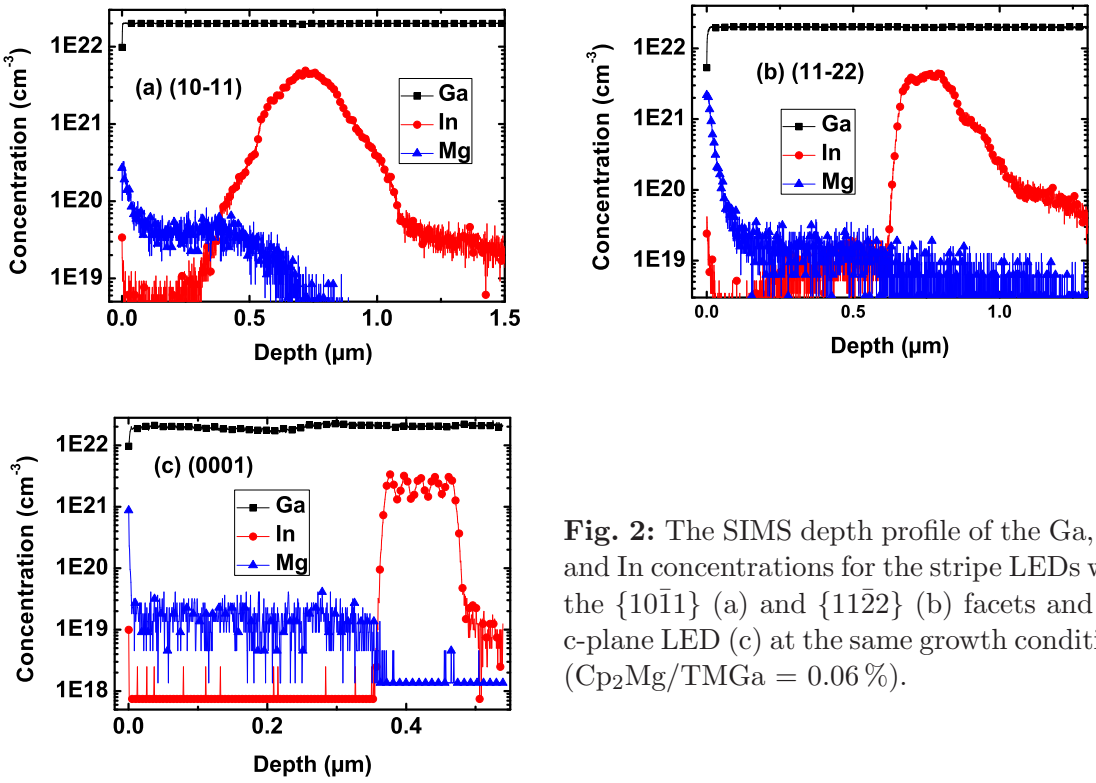

Fig. 2: The SIMS depth profile of the Ga, Mg and In concentrations for the stripe LEDs with the $\{10\bar{1}1\}$ (a) and $\{11\bar{2}2\}$ (b) facets and the c-plane LED (c) at the same growth conditions ($Cp_2Mg/TMGa = 0.06\,\%$).

to the PL spectrum, LT μ-PL was applied by employing a He-Cd laser $\lambda = 325\,\text{nm}$ as the excitation source. The excited area is around the stripe tip with a diameter of 1–2 μm. As shown in Fig. 3, pronounced donor-acceptor-pair (DAP) luminescence at 3.24 eV with characteristic LO-replicas was observed with $Cp_2Mg/TMGa$ of 0.04 % and 0.06 %. With further increasing $Cp_2Mg/TMGa$ of 0.10 % and 0.21 %, the DAP band shifts to a broad band emission at a lower energy presenting the emergence of self-compensation via the MgV_N pair [7, 10] for the stripe LEDs with the $\{10\bar{1}1\}$ facet. In contrary, self-compensation was not observed up to $Cp_2Mg/TMGa$ of 0.21 % for the stripe LEDs with the $\{11\bar{2}2\}$ facet. Thus, the Mg incorporation efficiency on the $\{10\bar{1}1\}$ facet is concluded to be higher than that on the $\{11\bar{2}2\}$ facet, consistent with the SIMS data.

EL is measured for all the five stripe LEDs with the $\{10\bar{1}1\}$ facet. The EL output power is low with a too low Mg concentration of $3 \times 10^{19}\,\text{cm}^{-3}$, probably due to the inferior hole injection efficiency, and stays almost constant with Mg concentration ranging from $4.0 \times 10^{19}\,\text{cm}^{-3}$ to $1.3 \times 10^{20}\,\text{cm}^{-3}$ for the 3D LEDs with the $\{10\bar{1}1\}$ facet (Fig. 4). Obviously, it is not critical to control the Mg doping concentration very accurately to achieve high EL output power. A Mg doping concentration window between $4.0 \times 10^{19}\,\text{cm}^{-3}$ and $1.3 \times 10^{20}\,\text{cm}^{-3}$ could offer good enough hole conductivity aiming at high EL output power. The Mg-related DAP emission shifts from a peak at 3.24 eV with the characteristic LO-replicas to the broad band at a lower energy during the suitable Mg doping concentration window as discussed above. These results show, that the typical change of the line shape of the Mg-related emission allows to recognize a suitable Mg doping concentration for 3D structures.

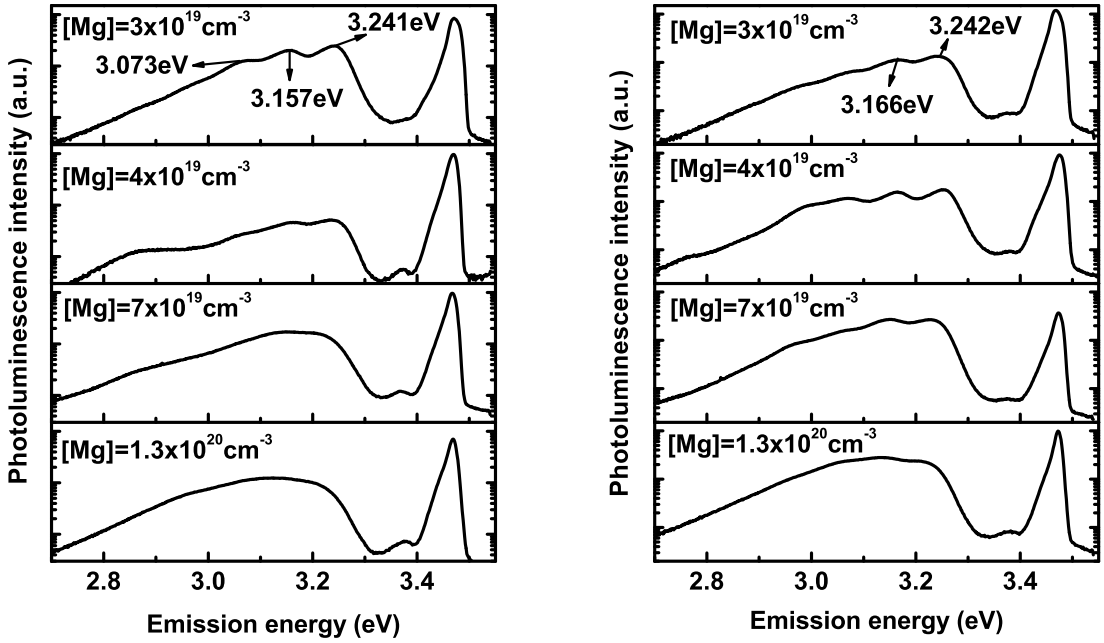

Fig. 3: The LT µ-PL spectra of the stripe LEDs with the $\{10\bar{1}1\}$ (left) and $\{11\bar{2}2\}$ (right) facets varying Cp_2Mg/TMGa during the main p-GaN layer growth. The spectra is normalized to the intensity of the GaN D^OX peak. The excited area is around the stripe tip with a diameter of 1–2 µm.

In order to obtain good ohmic p-contact performance, Cp_2Mg/TMGa was ramped up from 0.06 % for the main p-GaN layer growth to 0.80 %, 1.34 % and 1.60 % during the growth of a thin p-GaN capping layer for three samples. The Mg concentration at the sample surface, in other words, at the interface between the p-type semiconductor and the metal contact, was measured to be about $2 \times 10^{20}\,\mathrm{cm}^{-3}$ for the second sample by SIMS. With a linear extrapolation, the Mg concentration at the sample surface is estimated to be $1.2 \times 10^{20}\,\mathrm{cm}^{-3}$ and $2.4 \times 10^{20}\,\mathrm{cm}^{-3}$ for the first and third samples.

The complete LED device can be modelled as a Schottky diode and a pn-diode connected in series if there is any Schottky barriers between the p-type semiconductor and the metal contact. The relation between the voltage V and the current I is expressed by the equation:

$$V = \sum \frac{n_i kT}{q} \ln\left(\frac{I + I_{si}}{I}\right), i = 1, 2. \tag{1}$$

n, k, T, q and I_s represent the ideality factor, Boltzmann's constant, the absolute temperature, the elemental charge and the saturation current of the diode, respectively. Two items with $i = 1$, 2 stand for the voltage over the pn junction and the Schottky barrier at the p-type contact. Hence, the knee voltage of the complete device is the summation of the knee voltages of the pn junction and the Schottky barrier between the p-type semiconductor and the metal contact.

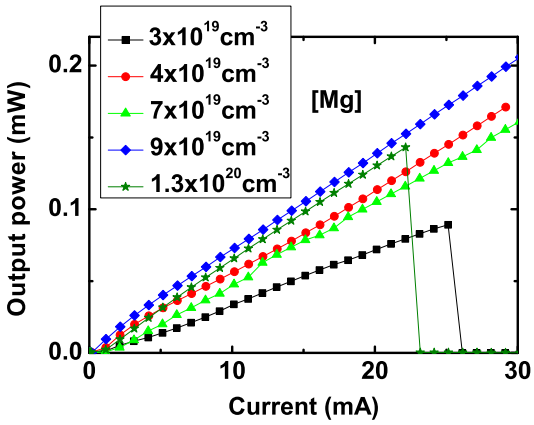

Fig. 4: The EL output power of the stripe LEDs with the $\{10\bar{1}1\}$ facet varying Cp_2Mg/TMGa during the main p-GaN layer growth.

The knee voltage of the LEDs with the $\{10\bar{1}1\}$ facet is determined from their IV curves (Fig. 5 (left)). It drops from 6.3 V to 4.3 V by increasing the Mg concentration from $1.2 \times 10^{20}\,\mathrm{cm}^{-3}$ to $2.0 \times 10^{20}\,\mathrm{cm}^{-3}$ and rises to 5.0 V with an even higher Mg concentration of $2.4 \times 10^{20}\,\mathrm{cm}^{-3}$. Excessive Mg doping is required to produce a deep-level-defect (DLD) band in the p-GaN capping layer and the carriers are transported from the metal contact to the p-GaN capping layer through the DLD band instead of overcoming a Schottky barrier [11]. The low Mg doping level of $1.2 \times 10^{20}\,\mathrm{cm}^{-3}$ results in a Schottky barrier between the semiconductor and the metal contact leading to a high knee voltage. The contact resistance is also higher in this case indicated by the slope of the IV curve after the diode switch-on compared to the other two samples with larger Mg concentrations. Thus, heat is generated due to the poor contact performance during the EL leading to a high junction temperature. As a result, the diode breaks down at a small operating current of 85 mA (Fig. 5 (right)) and the emission efficiency is lower when operated with a cw current compared to a pulsed current (Fig. 6).

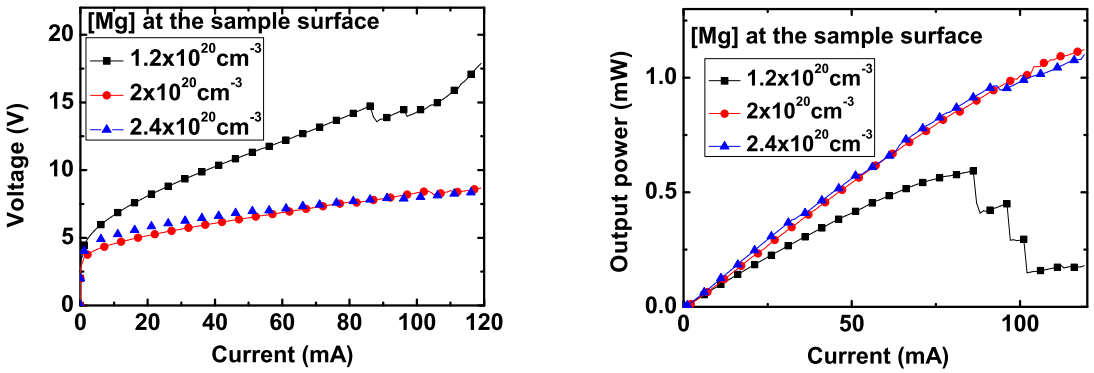

Fig. 5: The IV curve (left) and the output power (right) of the stripe LED with the $\{10\bar{1}1\}$ facet varying the Mg concentration at the interface between the p-type semiconductor and the metal contact.

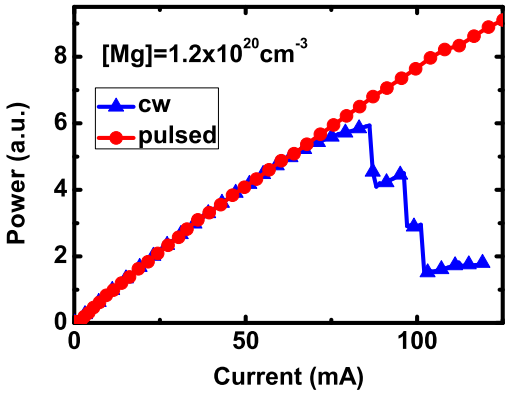

Fig. 6: The EL output power of the stripe LED with the $\{10\bar{1}1\}$ facet and the Mg concentration of $1.2\times10^{20}\,\mathrm{cm}^{-3}$ at the interface between the p-GaN and the contact metal under cw and pulsed currents.

The contact performance is improved by heavier Mg doping with the Mg concentration of $2 \times 10^{20}\,\mathrm{cm}^{-3}$ and deteriorates again slightly with an even higher Mg concentration of $2.4 \times 10^{20}\,\mathrm{cm}^{-3}$, presumably due to the crystal quality degradation with a too high Mg doping level.

Table 1: The knee voltage of the stripe LED with the $\{10\bar{1}1\}$ facet varying the Mg concentration at the interface between the p-type semiconductor and the metal contact.

Mg concentration (cm^{-3})	1.2×10^{20}	2×10^{20}	2.4×10^{20}
knee voltage (V)	6.3	4.3	5.0

4. Summary

Secondary ion mass spectrometry analysis revealed the Mg concentration of the 3D semipolar p-GaN, indicating a higher Mg doping concentration on the $\{10\bar{1}1\}$ facet by a factor of 2.7 compared to the $\{11\bar{2}2\}$ facet under the same growth conditions. The line shape of the Mg-related donor-acceptor-pair (DAP) emission confirmed the same conclusion that the Mg incorporation efficiency is higher on the $\{10\bar{1}1\}$ facet than on the $\{11\bar{2}2\}$ facet. The good range of the hole concentration for high EL output power could be estimated from the line shape of the Mg DAP band as well. The p-type contact performance was improved by excessive Mg doping.

Acknowledgment

I gratefully acknowledge the scientific and technical support from Y. Gao (Evans Analytical Group, USA), S. Bauer (Inst. of Quantum Matter), S. Alam and I. Schwaiger (Inst. of Optoelectronics). This work has been financially supported by the German Federal Ministry of Education and Research (BMBF).

References

[1] T. Langer, A. Kruse, F.A. Ketzer, A. Schwiegel, L. Hoffmann, H. Jönen, H. Bremers, U. Rossow, and A. Hangleiter, "Origin of the green gap: increasing nonradiative recombination in indium-rich GaInN/GaN quantum well structures", *Phys. Status Solidi C*, vol. 8, pp. 2170–2172, 2011.

[2] K. Fujito, K. Kiyomi, T. Mochizuki, H. Oota, H. Namita, S. Nagao, and I. Fujimura, "High-quality nonpolar m-plane GaN substrates grown by HVPE", *Phys. Status Solidi A*, vol. 205, pp. 1056–1059, 2008.

[3] F. Scholz, "Semipolar GaN grown on foreign substrates: a review", *Semicond. Sci. Technol.*, vol. 27, pp. 024002-1–15, 2012.

[4] T. Wunderer *et al.*, "Three-dimensional GaN for semipolar light emitters", *Phys. Status Solidi B*, vol. 248, pp. 549–560, 2011.

[5] H. Amano, M. Kito, K. Hiramatsu, and I. Akasaki, "P-type conduction in Mg-doped GaN treated with low-energy electron beam irradiation (LEEBI)", *Jpn. J. Appl. Phys.*, vol. 28, pp. L2112–L2114, 1989.

[6] S. Nakamura, T. Mukai, M. Senoh, and N. Iwasa, "Thermal annealing effects on p-type Mg-doped GaN films", *Jpn. J. Appl. Phys.*, vol. 31, pp. L139–L142, 1992.

[7] U. Kaufmann, P. Schlotter, H. Obloh, K. Köhler, and M. Maier, "Hole conductivity and compensation in epitaxial GaN:Mg layers", *Phys. Rev. B*, vol. 62, pp. 10867–10872, 2000.

[8] J. Hertkorn, F. Lipski, P. Brückner, T. Wunderer, S.B. Thapa, F. Scholz, A. Chuvilin, U. Kaiser, M. Beer, and J. Zweck, "Process optimization for the effective reduction of threading dislocations in MOVPE grown GaN using in situ deposited SiN_x masks", *J. Cryst. Growth*, vol. 310, pp. 4867–4870, 2008.

[9] H. Amano, M. Kitoh, K. Hiramatsu, and I. Akasaki, "Growth and luminescence properties of Mg-doped GaN prepared by MOVPE", *J. Electrochem. Soc.*, vol. 137, pp. 1639–1641, 1990.

[10] L. Eckey, U.V. Gfug, J. Holst, A. Hoffmann, B. Schineller, K. Heime, M. Heuken, O. Schön, and R. Beccard, "Compensation effects in Mg-doped GaN epilayers", *J. Cryst. Growth*, vol. 189/190, pp. 523–527, 1998.

[11] L.L. Wu, D.G. Zhao, D.S. Jiang, P. Chen, L.C. Le, L. Li, Z.S. Liu, S.M. Zhang, J.J. Zhu, H. Wang, B.S. Zhang, and H. Yang, "Effects of thin heavily Mg-doped GaN capping layer on ohmic contact formation of p-type GaN", *Semicond. Sci. Technol.*, vol. 28, pp. 105020-1–5, 2013.

Galliumnitride Nanostripes with Semipolar Quantum Wells for LED and Laser Applications

Robert A. R. Leute

We present LEDs and asymmetric waveguide structures with embedded nanostripes and semipolar $\{10\bar{1}1\}$ *quantum wells. All samples are based on c-plane GaN/AlGaN templates grown heteroepitaxially on c-plane sapphire substrates by metal organic vapour phase epitaxy. The nanostripes have a periodicity of 250 nm and were achieved by selective area epitaxy with dielectric growth masks structured on full 2-inch wafers. After quantum well growth on the semipolar crystal facets of the nanostripes, they are completely embedded, resulting in a flat c-plane surface. This allows conventional device processing to be applied. Structural, optical, and electrical characterization has been performed.*

1. Introduction

Research in semipolar GaN crystal planes for efficient green light emitters is still ongoing [1, 2]. Best results have been achieved based on free-standing GaN templates and homoepitaxial approaches [3–6]. These commercially available, semipolar GaN quasi-substrates are high in cost and small in size. Consequently, heteroepitaxy of semipolar GaN based on cheap sapphire substrates maintains interest [7]. We pursue one of these heteroepitaxial approaches, i.e. the selective growth of 3D structures with semipolar surfaces which is based on growth in c-direction. Thus, it can be realized on cheap and also large foreign substrates, i.e. sapphire. Already, a high crystal quality has been achieved despite heteroepitaxy [8]. LEDs with semipolar QWs based on micrometer sized 3D structures have been reported [9,10]. Yet, these 3D topologies require specially adapted device processing. Our aim is therefore to maintain a plane surface, where established structuring methods for contacts, resonator formation etc. can be applied. We reduce the size of

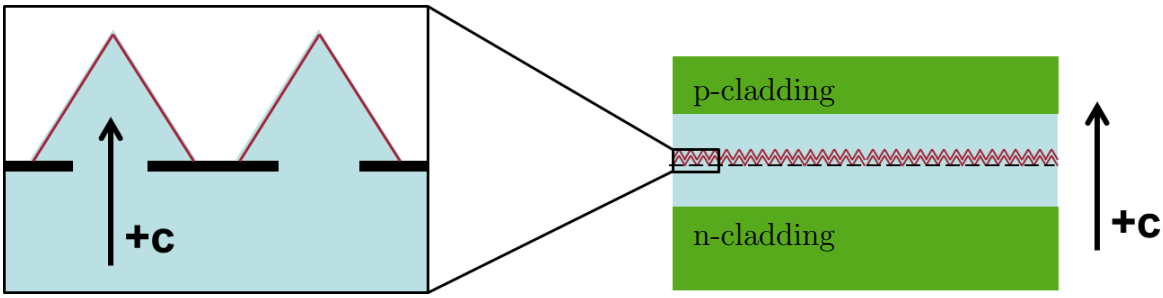

Fig. 1: Reduction of size of 3D GaN will allow embedding of semipolar QWs within conventional c-oriented layers.

the 3D structures in order to use them exclusively within the active region of our aspired devices. This miniaturization allows subsequent planarization (see Fig. 1). All dimensions must be restricted to a few hundred nanometers, beyond the limitations of conventional optical lithography. Previously, we have reported on nanostructuring for selective area epitaxy based on laser interference lithography (LIL) for LED [11] and photonic crystal applications [12]. However, the LIL samples still suffered from mask irregularities and the structured area was limited to some cm^2, which is why an alternative structuring method was used as described in the following.

2. Experimental

The samples are grown in an Aixtron-200/4RF-S HT MOVPE reactor with standard precursors TMAl, TMGa, TMIn and high purity ammonia. Silane and Cp_2Mg are used for n- and p-doping, respectively; Pd diffused hydrogen and high purity nitrogen are used as carrier gases. First, c-oriented GaN/AlGaN templates of about 3.5 µm thickness are grown on c-plane sapphire with conventional growth conditions. An oxygen doped AlN nucleation layer as well as an in-situ deposited SiN interlayer are employed for defect reduction [13]. The top 1.8 µm are silicon-doped to achieve a nominal doping level of $3.5 \times 10^{18} cm^{-3}$. The templates include a 0.4 µm thick $Al_{0.1}Ga_{0.9}N$ as bottom waveguide cladding and are capped with 30 nm GaN. Afterwards, 30 nm SiN_x is deposited by PECVD as growth mask. Upon this dielectric mask, a very thin (below 100 nm) layer of resist is structured by nanoimprint lithography [2]. Dry etching with SF_6, results in stripes aligned parallel to the a-direction of GaN with a period of 250 nm over the full 2-inch wafer. Afterwards, any remaining resist is removed by an O_2-plasma treatment and the samples are cleaned with a mixture of H_2O_2 and H_2SO_4 and an aqueous KOH solution, before being reloaded into the MOVPE reactor. GaN stripes with a triangular cross section and $\{10\bar{1}1\}$ side facets are grown at 950 °C for 110 s with a V/III ratio of 260. An InGaN pre-well of 50 nm thickness with 5% In is deposited on top of the stripes, in order to reduce the strain gradient and increase the confinement. An InGaN quantum well is grown at 750 °C to 770 °C to achieve an emission wavelength of 420 nm to 460 nm. After an undoped spacer, the stripes are embedded with a Mg-doped layer at 1080 °C with a V/III ratio of 1080 resulting in a planar surface. At this point, the structure includes neither an electron blocking layer nor multiple quantum wells common to c-plane LEDs. The fully planarized laser structures were investigated by transmission electron microscopy (TEM) and scanning transmission electron microscopy (STEM) at the central electron microscopy facility of Ulm University for structural defects. The embedding with doped GaN allows electrical pumping of the semipolar QWs. For electrical characterization, the samples were annealed in an ambient atmosphere at 750 °C for 60 s to activate the Mg-acceptors. Indium contacts were evaporated onto the p-side of the LED. The contacts had diameters ranging from 70 µm to 140 µm and were 1 µm thick. Measurements were taken inside an integrating sphere and P-I as well as I-V curves were recorded.

[2] Carried out by J. Harming of the EV Group E. Thallner GmbH

3. Results

We achieved homogeneous growth of sub-micrometer sized stripes aligned along $< 11\bar{2}0 >$ over the complete sample area enabling subsequent embedding. Mg doping enhances the lateral growth [14] and facilitates the planarization of the device. Yet, the stability of the $\{10\bar{1}1\}$ facets [15] requires relatively long overgrowth times (equivalent to 180 nm layer thickness) compared to typical c-plane LED p-type layers.

3.1 Structural analysis

Figure 2 shows both weak-beam dark-field and bright-field TEM images of a sample cross-section from sapphire to surface highlighting threading dislocations (TDs). The effective defect reduction by the in-situ SiN_x interlayer is clearly visible. Only few dislocations penetrate and go on to the surface and we find no indication that new dislocations are created at the interfaces, affecting the semipolar quantum wells. Additionally, almost no

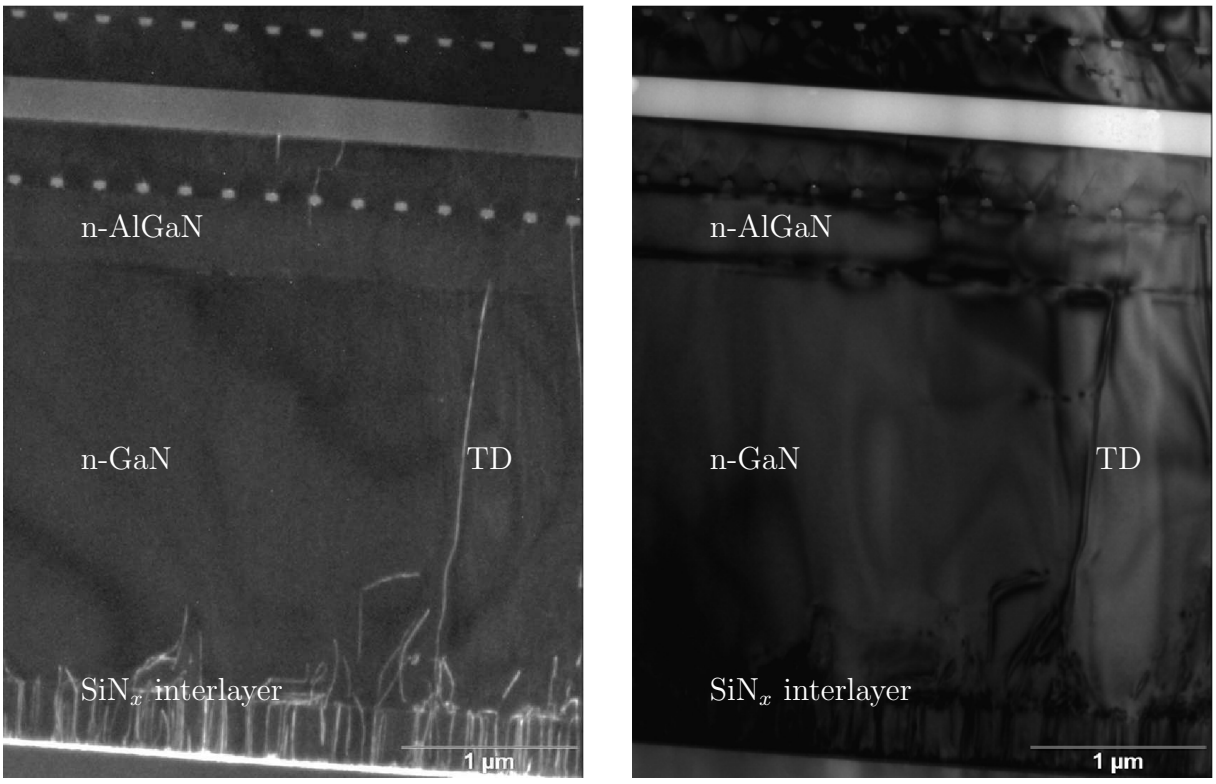

Fig. 2: Weak-beam dark-field (left) and bright-field (right) TEM image. TDs are stopped by the in-situ SiN_x mask. The active zone within the waveguide structure and the semipolar QWs are almost defect-free.

stacking faults (SFs) are found which often affect semipolar QWs. Figure 3 shows a high-angle annular dark field (HAADF)STEM image of the upper region, providing excellent Z-contrast; the AlGaN waveguide cladding is clearly visible and with very few defects present. The SiN_x mask exhibits a homogeneity of a few nanometers. A more detailed look (Fig. 4) shows the homogeneity of the semipolar QW on the stripes. The thickness of

the single QW stays constant and has only slight variation. This is a huge improvement compared to previous results [11] where mask irregularities resulted in distorted quantum wells.

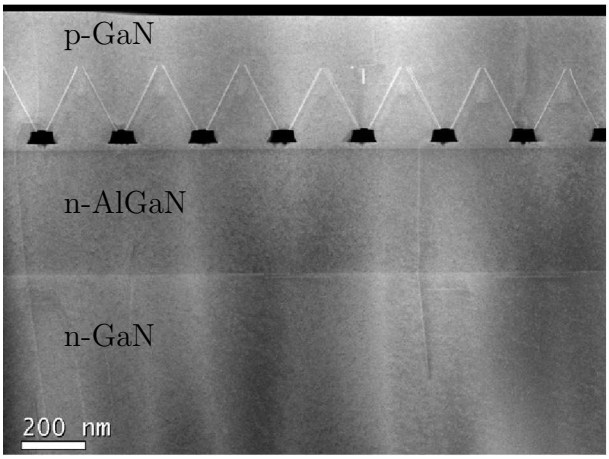

Fig. 3: HAADF STEM image of the waveguide region. Some TDs penetrate, but almost no SFs are found.

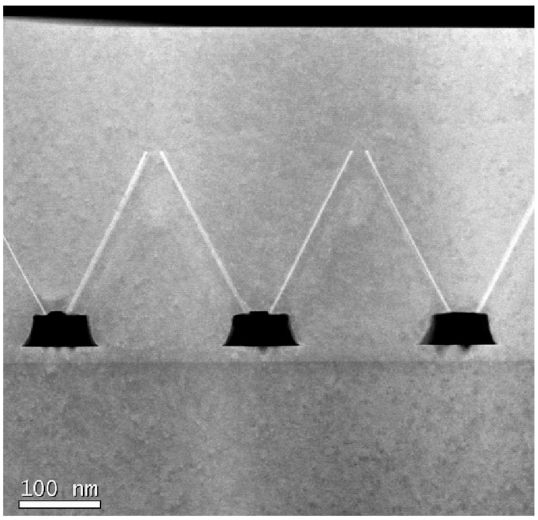

Fig. 4: HAADF STEM image of two triangular stripes. The QWs show very little thickness variance along the facet.

3.2 Electrical characterization

The laser structures include a fully functional p-n junction, so testing in LED mode is easily available. They were activated for 1 minute at 750 °C in ambient atmosphere before In contacts were deposited for on-wafer testing. Figure 5 shows the power-current-voltage characteristics of a laser structure in LED operation under cw-conditions. The emission wavelength is 430 nm with a FWHM of 130 meV (spectra not shown).

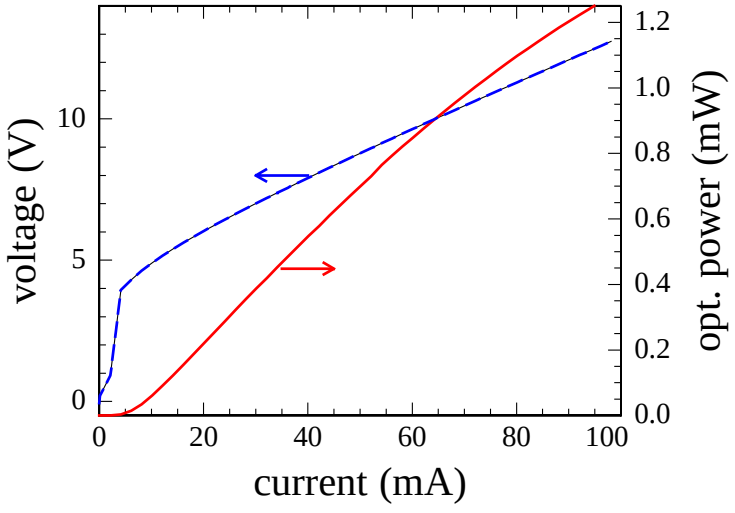

Fig. 5: P-I-V characteristics of laser structure with GaN nanostructures under LED operation.

4. Conclusion

We have fabricated GaN based LEDs with GaN nanostripes and semipolar QWs embedded within a waveguide structure on 2-inch c-oriented sapphire substrates. Analysis by TEM and STEM shows that our nanoimprint structuring results in highly homogeneous and high quality semipolar quantum wells which are completely embedded. On-wafer testing in LED operation produced electroluminescence over 1 mW output power.

Acknowledgment

Technical support by I. Schwaiger, R. Blood and R. Rösch at the Institute of Optoelectronics, Ulm University, S. Grözinger at the Central Electron Microscopy Facility, Ulm University and J. Harming and C. Thanner at the EV Group Erich Thallner GmbH is gratefully acknowledged. We thank D. Heinz for fruitful discussions and J. Wang, T. Meisch, D. Geiger and J. Biskupek for scientific support. This work has been partially financed by the Deutsche Forschungsgemeinschaft within the research group FOR957 PolarCoN.

References

[1] H. Ohta, S.P. DenBaars, and S. Nakamura, "Future of group-III nitride semiconductor green laser diodes", *J. Opt. Soc. Am. B*, vol. 27, pp. B45–B49, 2010.

[2] M.T. Hardy, D.F. Feezell, S.P. DenBaars, and S. Nakamura, "Group III-nitride lasers: a materials perspective", *Materials Today*, vol. 14, pp. 408–415, 2011.

[3] Y. Enya, Y. Yoshizumi, T. Kyono, K. Akita, M. Ueno, M. Adachi, T. Sumitomo, S. Tokuyama, T. Ikegami, K. Katayama, and T. Nakamura, "531 nm green lasing of InGaN based laser diodes on semi-polar $\{20\bar{2}1\}$ free-standing GaN substrates", *Appl. Phys. Express*, vol. 2, pp. 082101-1–3, 2009.

[4] M. Adachi, Y. Yoshizumi, Y. Enya, T. Kyono, T. Sumitomo, S. Tokuyama, S. Takagi, K. Sumiyoshi, N. Saga, T. Ikegami, M. Ueno, K. Katayama, and T. Nakamura, "Low threshold current density InGaN based 520–530 nm green laser diodes on semi-polar $\{20\bar{2}1\}$ free-standing GaN substrates", *Appl. Phys. Express*, vol. 3, pp. 121001-1–3, 2010.

[5] A. Avramescu, T. Lermer, J. Müller, C. Eichler, G. Bruederl, M. Sabathil, S. Lutgen, and U. Strauss, "True green laser diodes at 524 nm with 50 mW continuous wave output power on *c*-plane GaN", *Appl. Phys. Express*, vol. 3, pp. 061003-1–3, 2010.

[6] R.M. Farrell, E.C. Young, F. Wu, S.P. DenBaars, and J.S. Speck, "Materials and growth issues for high-performance nonpolar and semipolar light-emitting devices", *Semicond. Sci. Technol.*, vol. 27, pp. 024001-1–14, 2012.

[7] F. Scholz, "Semipolar GaN grown on foreign substrates: a review", *Semicond. Sci. Technol.*, vol. 27, pp. 024002-1–15, 2012.

[8] T. Wunderer *et al.*, "Three-dimensional GaN for semipolar light emitters", *Phys. Status Solidi B*, vol. 248, pp. 549–560, 2011.

[9] B. Neubert, T. Wunderer, P. Brückner, F. Scholz, M. Feneberg, F. Lipski, M. Schirra, and K. Thonke, "Semipolar GaN/GaInN LEDs with more than 1mW optical output power", *J. Cryst. Growth*, vol. 298, pp. 706–709, 2007.

[10] T. Wunderer, J. Wang, F. Lipski, S. Schwaiger, A. Chuvilin, U. Kaiser, S. Metzner, F. Bertram, J. Christen, S.S. Shirokov, A.E. Yunovich, and F. Scholz, "Semipolar GaInN/GaN light-emitting diodes grown on honeycomb patterned substrates", *Phys. Status Solidi C*, vol. 7, pp. 2140–2143, 2010.

[11] R.A.R. Leute, D. Heinz, J. Wang, F. Lipski, T. Meisch, K. Thonke, J. Thalmair, J. Zweck, and F. Scholz, "GaN based LEDs with semipolar QWs employing embedded sub-micrometer sized selectively grown 3D structures", *J. Cryst. Growth*, vol. 370, pp. 101–104, 2013.

[12] D. Heinz, R.A.R. Leute, S. Kizir, Y. Li, T. Meisch, K. Thonke, and F. Scholz, "Ga(In)N photonic crystal light emitters with semipolar quantum wells", *Jpn. J. Appl. Phys.*, vol. 52, pp. 062101-1–5, 2013.

[13] J. Hertkorn, F. Lipski, P. Brückner, T. Wunderer, S.B. Thapa, F. Scholz, A. Chuvilin, U. Kaiser, M. Beer, and J. Zweck, "Process optimization for the effective reduction of threading dislocations in MOVPE grown GaN using in situ deposited SiN_x masks", *J. Cryst. Growth*, vol. 310, pp. 4867–4870, 2008.

[14] B. Beaumont, S. Haffouz, and P. Gibart, "Magnesium induced changes in the selective growth of GaN by metalorganic vapor phase epitaxy", *Appl. Phys. Lett.*, vol. 72, pp. 921-923, 1998.

[15] Y. Kato, S. Kitamura, K. Hiramatsu, and N. Sawaki, "Selective growth of wurtzite GaN and $Al_xGa_{1-x}N$ on GaN/sapphire substrates by metalorganic vapor phase epitaxy", *J. Cryst. Growth*, vol. 144, pp. 133–140, 1994.

Nitrogen-Polar GaN Nanowires With Coaxial GaInN Quantum Wells

Dominik Heinz

In this work, position-controlled growth of nitrogen-polar Ga(In)N nanowire heterostructures with aspect ratios up to 20 is presented. By using nanoimprint lithography and dry etching techniques for the mask patterning, nanowires with diameters down to about 300 nm are grown by selective area metal organic vapor phase epitaxy. GaInN quantum wells are realized on the side facets of these structures. Additionally, positioning and alignment of individual wires is demonstrated by application of alternating current dielectrophoresis allowing optical investigations on single wires.

1. Introduction

Besides applications of nanowire heterostructures in general lighting [1] and lasing [2], in particular nanotechnology-based solid-state sensing is expected to become one major focus of research in the next decades [3]. Here, new sensing systems may particularly involve interdisciplinary fields of research beyond classical optoelectronics: e.g. sensors for biomolecules [4], liquids and gases [5–7]. Nanowire heterostructures based on III-nitride ternary alloys are expected to be particularly suitable for optical gas sensing applications due to their large and tunable bandgap [6, 7]. The purely optical sensing principle relies on changes in the photoluminescence signal due to the adsorption of oxidative or reductive gas molecules and atoms on the surface of the nanowires. Models based on near-surface band bending due to the altered Fermi-level pinning as well as induced changes in the non-radiative recombination processes are controversially discussed in literature [7].

Particularly, GaN provides chemical inertness as well as good thermal, chemical and mechanical stability enabling applications in harsh environments, e.g. for combustion monitoring [3, 8, 9]. GaN nanowires have been so far predominantly grown by molecular beam epitaxy (MBE) which also allows integration of AlGaN/GaN nanodiscs [7] while coaxial heterostructures are significantly more difficult to be realized. However, particularly coaxial structures are very promising for sensing applications as quantum wells realized on the side facets of nanowires are expected to benefit from the large surface-to-volume ratio.

Recently, research in the selective area growth of nanowires with Ga- as well as N-polarity by metal organic vapor phase epitaxy (MOVPE) has found increasing interest [1, 10]. Particularly, nanoimprint and holographic lithography have enabled a fast and large area patterning and additionally provide a diameter control of the nanowires [11, 12]. For Ga-polar nanowires usually additional semipolar facets develop during growth at the tips of

the wires [1] which seems not to be the case for purely N-polar wires [10]. These additional facets might contribute to the emitted photoluminescence besides the standard m-plane side facets.

In this work, basic studies on the selective area growth of N-polar Ga(In)N nanowires are performed. Characterization of individual wires by micro-photoluminescence spectroscopy, e.g. in different gas ambients, typically requires large distances between the wires or a complete separation of individiual wires due to the limited spatial resolution. Therefore, additionally the application of alternating current (AC) dielectrophoresis as a positioning and alignment method [13] for characterization of individual wires is investigated.

2. Experimental

Position-controlled nitrogen-polar GaN nanowires are realized on structured 2" c-plane sapphire substrates. A 20 nm thick SiO_2 is deposited by plasma enhanced chemical vapor deposition onto the sapphire wafers which serves as a mask material for the selective area growth. Nanoimprint lithography[2] and dry etching is applied in order to create holes with diameters of about 500 nm and 300 nm as well as periods corresponding to 1 µm and 500 nm into the SiO_2 layer, respectively.

Subsequently, in-situ nitridation of the sapphire in ammonia atmosphere at about 1100 °C is performed in order to enforce the N-polar growth by creation of a thin AlN nucleation layer [14]. Nitridation and following selective area epitaxy are carried out in an horizontal flow Aixtron MOVPE reactor using nitrogen and hydrogen as carrier gas, respectively. The development of Ga-polar inversion domains during N-polar GaN growth is a common problem. The polarity of the nanowires is therefore confirmed by wet chemical etching [15] in a hot 5 molar potassium hydroxide solution at 80°C based on the significant difference in etching rates between Ga- and N-polar GaN.

For the positioning of individual nanowires with AC dielectrophoresis a large amount of the wires is separated from the sapphire substrate by scratching them with a TEM-grid and suspending them into isopropanol. Subsequently, the solution is deposited onto a SiO_2 layer on Si with Ti/Au finger structures realized by conventional optical lithography. A voltage of $V = 5\,\mathrm{V}$ with a frequency $f = 10\,\mathrm{kHz}$ is applied at the Ti/Au finger structures in order to position and align the wires at the positions of maximum field strength by AC dielectrophoresis.

3. N-Polar Ga(In)N Nanowires

Generally, vertical growth of GaN nanowires by MOVPE requires very low V/III ratios [1] compared to growth conditions known from planar GaN but also from other three-dimensional structures [16, 17]. However, these growth conditions can be detrimental for selectivity during nucleation. By using a two-step growth mode with a nucleation

[2]Carried out by the EV Group E. Thallner GmbH

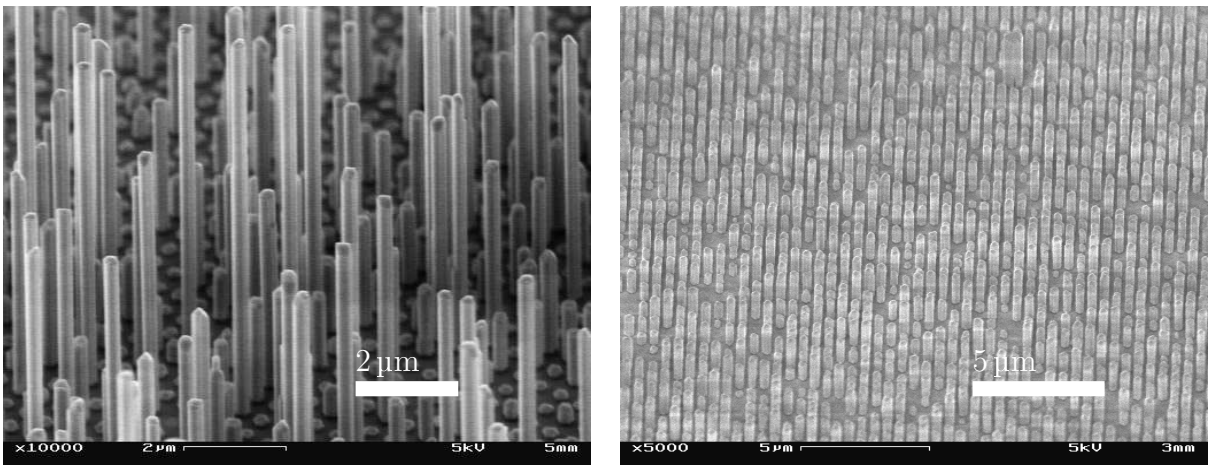

Fig. 1: SEM micrographs of N-polar GaN nanowires selectively grown on a sapphire substrate (left). Improved homogeneity and reduced vertical growth is observed for a reduced silane flow (right).

at high V/III $\approx$ 1000 ratio and reduced temperature in order to fill the mask openings and a subsequent change to lower V/III $\approx$ 60 in order to enhance vertical growth, these two distinct regimes can be combined. Additionally, the introduction of silane has been reported to result in an enhanced vertical growth but may also lead to a passivation during growth [1]. In this work, an additional silane flow is applied in order to enhance the vertical nanowire growth.

A scanning electron micrograph (SEM) of our as-grown nanowires using the two-step growth with silane doping ($n \approx 70\,\mathrm{nmol/min}$) is given in Fig. 1. Nanowires with aspect ratios up to 20 and diameters down to about 300 nm can be realized by using the structured sapphire wafers. In contrast to directly grown nanowires on sapphire, the nanoimprint lithography step enables a much more precise diameter control.

Nucleation conditions have been optimized resulting in an homogeneous filling of all mask openings. However, by changing the growth conditions to enhanced vertical growth homogeneity is reduced which we attribute to a passivation of the nanowires with silicon nitride due to the strong Si-doping. A reduction of the silane flow results in more homogeneous growth and slightly increased lateral growth (Fig. 1, right).

Almost all wires are significantly etched in a hot potassium hydroxide solution which confirmes the predominant N-polarity of the structures. The wires are mainly etched from the top facets, while the $(10\bar{1}0)$ side facets of the rods are surprisingly very stable against the etchant. In areas where growth has stopped after nucleation, the nucleation sites are almost completely removed indicating N-polarity also for the small plateaus.

Coaxial GaInN has been deposited of the side facets of the wires without observing polycrystalline growth on the mask caused by the reduced growth temperatures (Fig. 2). Low temperature integral photoluminescence over a large ensemble of wires shows a dominant contribution of the expected GaInN quantum well luminescence at about 3.15 eV. Spatially and spectrally-resolved investigations on single wires will be presented elsewhere.

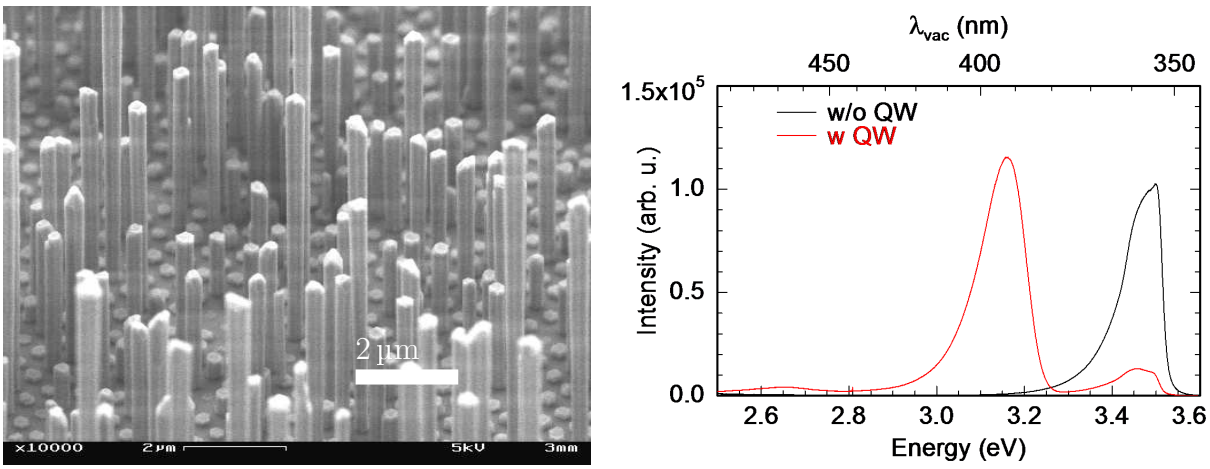

Fig. 2: SEM micrograph of N-polar Ga(In)N nanowires (left) and corresponding integral low temperature ($T \approx 15\,\mathrm{K}$) photoluminescence spectrum of a large amount of wires with and without coaxial GaInN (right).

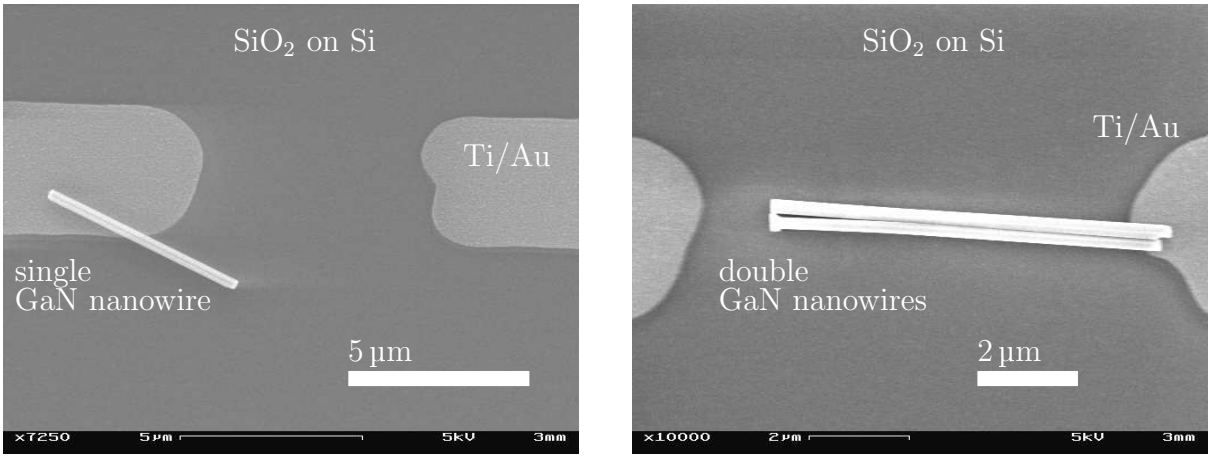

Fig. 3: SEM micrographs of separated GaN nanowires positioned and aligned by AC dielectrophoresis on a SiO_2 layer deposited on Si. Trapped but imprecisely aligned nanowire (left) and properly trapped and aligned double wires (right).

4. Dielectrophoresis

Alternating current dielectrophoresis is a common method for positioning and alignment of small particles as well as nanowires based on different material systems [13]. Typical applications mainly include electrical measurements, but the dielectrophoretic positioning can also be used to simplify the locating and separation of single wires on a large area substrate.

By using AC dielectrophoresis, single GaN nanowires and small ensembles of wires can be positioned and subsequently identified by scanning electron microscopy (SEM). While other groups mainly focus on a high yield rate of trapped nanowires for electrical measurements [13], micro-photoluminescence spectroscopy requires a trapping of individual nanowires in order to allow a modal characterization and sensing on a single wire. There-

fore, a rather low concentration of nanowires in the suspension and a moderate applied voltage is required. Common difficulties include the unintended trapping of several wires and imprecise alignment (Fig. 3). However, also positioned and aligned double nanowire structures might be interesting for future investigations of the coupling behavior of guided modes between two wires.

5. Summary

In this work, the position-controlled growth of Ga(In)N nanowires with high aspect ratios by MOVPE has been investigated. After separation of the wires from the sapphire substrate, dielectrophoresis allows an positioning and alignment of individual wires. This separation allows an individual characterization, e.g. by micro-photoluminescence, but also investigations on the response of single wires to different gas ambients.

Acknowledgment

Technical and scientific support by O. Rettig, G. He, R.A.R. Leute, R. Rösch, F. Huber, J. Jakob, M. Madel, M. Hocker, I. Tischer and K. Thonke is gratefully acknowledged. The authors thank J. Harming and C. Thanner at the EV Group Erich Thallner GmbH for the nanoimprint processing. This work was financially supported by the Baden-Württemberg Stiftung gGmbH within the project "Nitridische Nanosäulen für optisch auslesbare Sensoranwendungen".

References

[1] A. Waag, X. Wang, S. Fündling, J. Ledig, M. Erenburg, R. Neumann, M. Al Suleiman, S. Merzsch, J. Wei, S. Li, H.H. Wehmann, W. Bergbauer, M. Straßburg, A. Trampert, U. Jahn, and H. Riechert, "The nanorod approach: GaN nanoLEDs for solid state lighting", *Phys. Status Solidi C*, vol. 8, pp. 2296–2301, 2011.

[2] J.C. Johnson, H.J. Choi, K.P. Knutsen, R.D. Schaller, P. Yang, and R.J. Saykally, "Single gallium nitride nanowire lasers", *Nat. Mater.*, vol. 1, pp. 106–110, 2002.

[3] N. Miura, P. Elumalai, V.V. Plashnitsa, T. Ueda, R. Wama, and M. Utiyama, *Solid State Gas Sensing*, New York: Springer Science + Business Media, 2009.

[4] G. Zheng, F. Patolsky, Y. Cui, W.U. Wang, and C.M. Lieber, "Multiplexed electrical detection of cancer markers with nanowire sensor arrays", *Nat. Biotechnol.*, vol. 23, pp. 1294–1301, 2005.

[5] Q. Wan, Q.H. Li, Y.J. Chen, T.H. Wang, X.L. He, J.P. Li, and C.L. Lin, "Fabrication and ethanol sensing characteristics of ZnO nanowire gas sensors", *Appl. Phys. Lett.*, vol. 84, pp. 3654–3656, 2004.

[6] W. Lim, J.S. Wright, B.P. Gila, J.L. Johnson, A. Ural, T. Anderson, F. Ren, and S.J. Pearton, "Room temperature hydrogen detection using Pd-coated GaN nanowires", *Appl. Phys. Lett.*, vol. 93, pp. 072109-1–3, 2008.

[7] J. Teubert, P. Becker, F. Furtmayr, and M. Eickhoff, "GaN nanodiscs embedded in nanowires as optochemical transducers", *Nanotechnology*, vol. 22, pp. 275505-1–5, 2011.

[8] J. Sim, K. Kim, S. Song, and J. Kim, "Suspended GaN nanowires as NO2 sensor for high temperature applications", *Analyst*, vol. 138, pp. 2432–2437, 2013.

[9] J. Schalwig, G. Müller, M. Eickhoff, O. Ambacher, and M. Stutzmann, "Group III-nitride-based gas sensors for combustion monitoring", *Mat. Sci. Eng. B*, vol. 93, pp. 207–214, 2002.

[10] X.J. Chen, G. Perillat-Merceroz, D. Sam-Giao, C. Durand, and J. Eymery, "Homoepitaxial growth of catalyst-free GaN wires on N-polar substrates", *Appl. Phys. Lett.*, vol. 97, pp. 151909-1–3, 2010.

[11] S. Keller, C. Schaake, N.A. Fichtenbaum, C.J. Neufeld, Y. Wu, K. McGroddy, A. David, S.P. DenBaars, C. Weisbuch, J.S. Speck, and U.K. Mishra, "Optical and structural properties of GaN nanopillar and nanostripe arrays with embedded InGaN/GaN multi-quantum wells", *J. Appl. Phys.*, vol. 100, pp. 054314-1–7, 2006.

[12] T. Kuykendall, P.J. Pauzauskie, Y. Zhang, J. Goldberger, D. Sirbuly, J. Denlinger, and P. Yang, "Crystallographic alignment of high-density gallium nitride nanowire arrays", *Nat. Mater.*, vol. 3, pp. 524–528, 2004.

[13] T.H. Kim, S.Y. Lee, N.K. Cho, H.K. Seong, H.J. Choi, S.W. Jung, and S.K. Lee, "Dielectrophoretic alignment of gallium nitride nanowires (GaN NWs) for use in device applications", *Nanotechnology*, vol. 17, pp. 3394–3399, 2006.

[14] N. Grandjean, J. Massies, and M. Leroux, "Nitridation of sapphire. Effect on the optical properties of GaN epitaxial overlayers", *Appl. Phys. Lett.*, vol. 69, pp. 2071–2073, 1996.

[15] H.M. Ng, W. Parz, N.G. Weimann, and A. Chowdhury, "Patterning GaN microstructures by polarity-selective chemical etching", *Jpn. J. Appl. Phys.*, vol. 42, pp. L1405–L1407, 2003.

[16] D. Heinz, R.A.R. Leute, S. Kizir, Y. Li, T. Meisch, K. Thonke, and F. Scholz, "Ga(In)N photonic crystal light emitters with semipolar quantum wells", *Jpn. J. Appl. Phys.*, vol. 52, pp. 062101-1–5, 2013.

[17] R. Leute, D. Heinz, J. Wang, F. Lipski, T. Meisch, K. Thonke, J. Thalmair, J. Zweck, and F. Scholz, "GaN based LEDs with semipolar QWs employing embedded sub-micrometer sized selectively grown 3D structures", *J. Cryst. Growth*, vol. 370, pp. 101–104, 2013, 16th International Conference on Metalorganic Vapor Phase Epitaxy.

An In-Situ TEM Study on the Formation of Gold Carbide

Benedikt Westenfelder

In this study, a freestanding graphene membrane sheet serves as a quasi transparent substrate for aberration-corrected high-resolution transmission electron microscopy, as an in-situ heater, and as carbon supplier. The sheet has been previously decorated with gold nanoislands. During electron irradiation at 80 kV and at temperatures of approximately 1000 K, the accumulation of gold atoms has been observed on defective graphene sites or edges as well as at the facets of gold nanocrystals. Both resulted in clustering, forming unusual crystalline structures. Their lattice parameters and surface termination differ significantly from standard gold nanocrystals. We describe the stepwise formation of these little structures starting from irregular periodical arrangements of gold atoms into rectangularly shaped monolayers, then bilayers and entire cuboids of many atomic layers. Our experimental data, supported by electron energy loss spectroscopy and density-functional theory calculations, suggests that isolated gold and carbon atoms form — under conditions of heat and electron irradiation — a novel type of compound crystal, Au-C in zincblende structure.

1. Introduction

In 1900, Mathews & Watters reported about an very explosive gold acetylide Au_2C_2 [1]. The substance has been treated as a 'true' carbide and it was indeed the first time that the existence of gold carbide has been reported. Today, more than hundred years ago, the study of various compounds containing gold carbon bonds is covered by the field of organogold chemistry [2]. However, in comparison to many other pure metal carbides, there is no experimental evidence for a possible inorganic crystalline gold carbon compound and its structural properties [3]. This is not surprising, because bulk gold has almost no solubility for carbon under equilibrium conditions and the only (above mentioned) gold carbide supposed to be crystalline turned out to be extremely unstable [4]. Nowadays, there are several successful approaches in synthesizing carbide cluster ions for late transition metals such as gold [3]. Furthermore, several concepts have been developed in synthesizing, characterizing and understanding metastable carbide crystals regarding those transition metals [5, 6], but still with the exception of gold.

The structural analysis of new materials have undergone a tremendous improvement in the capabilities to explore the atomic configuration by aberration-corrected high-resolution transmission electron microscopy (AC-HRTEM) [7]. Our understanding of carbon systems such as graphene or carbon nanotubes has significantly benefitted from this development.

In-situ experiments enable the study of dynamic phenomena under direct observation of the atomic structure [8] within the range from room temperature up to ca. 2000 K [9]. Therewith, the potential of a free-standing graphene membrane as transparent and heatable substrate has been already demonstrated. Furthermore, this approach could be applied to investigate transformations of carbon adsorbates into graphene with atomic resolution [10]. In the present work, the approach of in-situ heating via electrical biasing the graphene has been applied with focus on gold nanoislands and their interaction with the graphene substrate driven by electron irradiation. The results have been interpreted with the help of density-functional theory (DFT) calculations and provide atomically resolved insights into an experimental (re)discovery of a surprisingly robust gold carbide phase.

2. Experiment

For this work, we prepared free-standing graphene layers with electric contacts in a TEM-compatible geometry. The graphene membrane is heated by Joule heating, and at the same time, electron irradiation during AC-HRTEM imaging drives structural changes and simultaneously allows atomic-level observation. Gold nanoparticles on the graphene sheet serve as a temperature reference, and are also involved in the reactions described below. The experimental concept of the electrically contacted sample cartridge and temperature estimates have been described in more detail previously [9]. In brief, a mechanically exfoliated graphene sheet is transferred onto a Si/SiN membrane structure with open windows and gold contacts, such that an electrically contacted and completely free-standing few-layer graphene substrate in a TEM-compatible geometry is formed. The gold nanoislands have been deposited ex-situ via thermal evaporation onto graphene. In-situ TEM has been performed applying AC-HRTEM combined with local electron energy loss spectroscopy (EELS). Further details are described in ref. [11].

3. Results and Discussion

The diffusion of Au adatoms on the nanoislands is already significant at RT and led to continuous shape changes of the particles upon heating [12]. After exceeding a certain temperature limit, the first almost spherically shaped particles form liquid drops and start to evaporate [13]. In accordance with theoretical predictions and similar experiments, the related melting temperature strongly depends on the particle size [14], and in our case is estimated to be in the range of 800 K to 1300 K for particle diameters in the range of 3 to 20 nm. The observations described in the following occurred at temperatures closely below the melting point of the gold particles (i.e., just before the particles melted upon increasing the heating current).

The diffusion barrier for gold adatoms on graphene is known to be fairly low — theoretically estimated to be 0.05 eV [15] — allowing the gold atoms to diffuse very easily along the surface. This movement is much faster than the average time used for a single frame exposure (0.5 to 1.0 s). For this reason we could only visualize single gold atoms, when they got trapped at grain boundaries, edge reconstructions or vacancies [16]. However, in

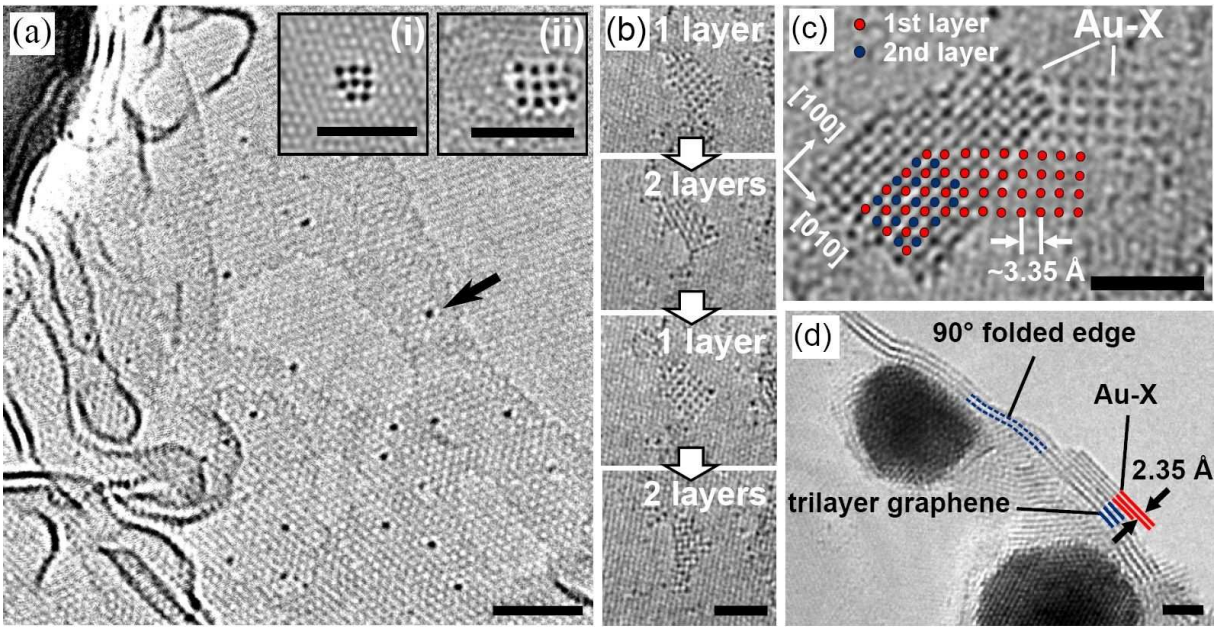

Fig. 1: AC-HRTEM images at 80 keV showing the atomic arrangements of gold atoms explored from tiny clusters towards small crystallites (scale bars are 2 nm). (a) Isolated heavy gold atoms trapped in carbon contamination on graphene, example indicated by an arrow. A larger gold particle is present in the upper left corner. Insets (i,ii) show small clusters that form under irradiation and heat within the carbon contamination layer on top of graphene. (i) Shows one very rare example found to be consistent with the interatomic distance of traditional gold clusters. Here, it has been determined to be 2.6 Å. (ii) Shows one of the frequently observed clusters having a larger spacing of 3.35 Å. (b) A repeated switching between a monolayer and bilayer structure in the same position. (c) A connected single- and double-layer region. The circles illustrate the atoms of the first and the second layer, respectively. (d) A few-layer graphene sheet with edges folded into a 90° angle. This side view enables also occasionally the side view on the Au-X structure (see marked region where 3 folded Au-X layers are found on top of folded 3-layer graphene).

these works there is no consideration of electron irradiation-induced diffusion mechanisms as discussed in Ref. [17, 18]. During the crystallization process of amorphous layers, we found plenty of gold atoms which were trapped at such lattice irregularities (Fig. 1a).

In many cases the adsorbed gold atoms within the carbon adsorbates form little clusters with squarish arrangements (insets of Fig. 1a). However, only one example could be identified with an interatomic spacing close to the bulk value for gold (2.88 Å) and expected for small clusters [19] (see Fig. 1a (i)). Typically, the clusters exhibit a surprisingly large nearest-neighbor atomic distance of 3.35 Å (see Fig. 1a (ii)). We assume that the larger spacing is due to the incorporation of low atomic number species into the 2-D gold lattice. However, those species will not be visible in-between gold atoms under the present imaging conditions, as supported by image simulations [11].

Several smaller regular clusters of Au-X with the 3.35 Å spacing have been observed, but only up to a size of about 30 Au-atoms, whereas larger Au-X clusters form multi-layer structures (Fig. 1b,c). In some cases, we could follow the transitions between single and

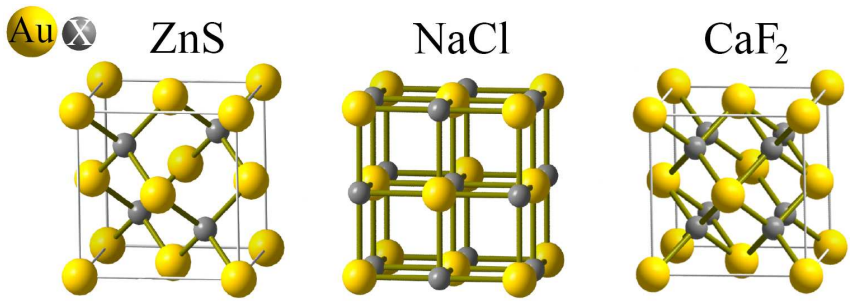

Fig. 2: Possible crystal structures with an unknown element X in the octahedral or in the tetrahedral voids of the gold fcc lattice.

double layers directly in real time (Fig. 1b). Fig. 1c shows a different example, where only a part of the structure is a single layer and the other part is a double or triple layer.

A side-view of the structure could be obtained for a cluster that had formed on the curved edge of a (partly broken) few-layer graphene substrate (Fig. 1d). Broken edges of freestanding graphene and few-layer graphene tend to curl up and show the typical van der Waals distance of 3.35 Å between the layers [20, 21]. A distance of 2.35 Å could be measured between the first and the second layer of our Au-X structure as marked in Fig. 1d. Considering that the atoms in the second layer are placed above the gaps of the first layer atoms (as shown in the plan-view in Fig. 1c), we obtain the same Au-Au spacing of 3.35 Å as between atoms inside a layer. Several times we observed tiny single-layers along with several larger, multi-layer structures [11]. Remarkably, the 3-D objects form precise cuboid shapes, as evidenced by their constant thickness (same contrast throughout the rectangle-shaped projection).

From these findings we can establish the structure of the Au-X lattice unambiguously. The gold atoms of these 3D nanocrystals exhibit a face-centered cubic (fcc) lattice structure with a corresponding lattice parameter of $\sqrt{2} \cdot (3.35 \pm 0.10)$ Å (a precise estimate was obtained from the fast Fourier transformation (FFT) taking the underlying graphene lattice as a calibration reference [11]). Bulk gold also has a fcc structure but with a smaller lattice parameter of $\sqrt{2} \cdot 2.88$ Å.

Considering the silicon nitride layer of the sample carrier, contamination induced during the graphene sheet transfer and/or adsorbed water from the surrounding regions of the sample carrier, several lighter elements like silicon, nitrogen or carbon could come into question. Finally, three different crystal structures are compatible to the observed fcc lattice for the incorporation of a second element: These are the zincblende (ZnS), the rock-salt (NaCl) and the fluorite structure (CaF_2) as illustrated in Fig. 2.

In order to determine the second element, local EELS was carried out in the TEM using a small beam diameter (5 nm). Multiple spectra with different energy ranges were acquired on a Au-X cube to consider the energy windows of the absorption edges of the above mentioned elements (Fig. 3). The presence of the elements carbon (Fig. 3a) and gold (Fig. 3b) is indicated by the clear signals of the carbon K absorption edge at 284 eV and the gold M_5 edge at 2206 eV. Silicon (Fig. 3c), nitrogen, and oxygen (Fig. 3d) as constituents can be excluded as the local EELS signals do not show any corresponding

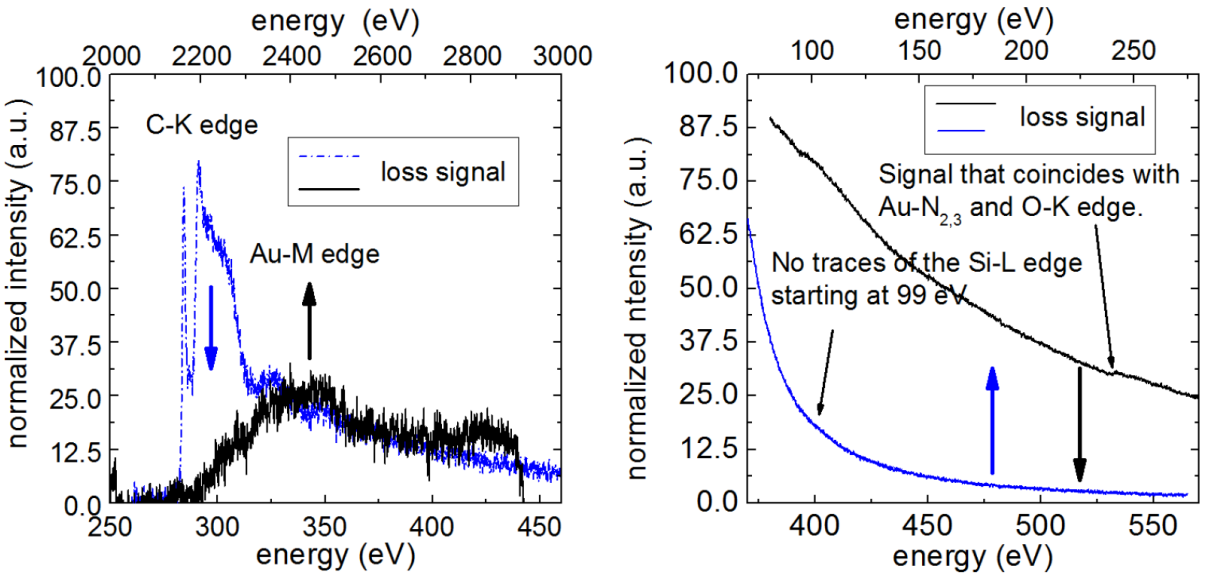

Fig. 3: Local EELS spectra acquired from Au-X on top of graphene. (a) Background-corrected energy loss of the carbon K edge at 284 eV and the gold M_5 edge at 2206 eV. (b) EELS spectrum obtained within energy range from 80 to 280 eV showing no signal of Si at 99 eV and within energy range from 370 to 570 eV. The signal at around 535 eV could caused by gold ($M_{4,5}$ edge) or oxygen (K edge).

absorption edges. The small signal at around 540 eV originates most probably from gold ($N_{2,3}$ edge). Energetically, it would also fit to the oxygen K edge. However, this signal is too weak (only 0.1 % above background) and therefore it would only correspond to a handful of atoms [22]. Although the detection of carbon appears to be trivial, because the Au-X cuboid is directly located on top of the multilayer graphene substrate, the exclusion of all other reasonable elements justifies the conclusion that carbon and must be the only constituent element in addition to gold.

In order to help identifying possible candidate compounds, we have performed DFT calculations. Clearly, only the small elements from the second row of the periodic table (C, N, O) provide a reasonable lattice match, while e.g. any theoretically considered silicon compound would result in a much larger lattice parameter than observed in the experiment. This also fits to the above mentioned EELS spectra showing silicon not to be locally present. Indeed, the smallest lattice parameter deviation Δ is achieved for the NaCl structures of AuC, AuN and AuO. However, DFT calculations combined with the generalized gradient approximation (GGA) tend to yield larger values compared to those observed in the experiments [23, 24], i.e. our calculated DFT-GGA value for gold is about 2.4% larger than the experimentally estimated one. If we treat this difference as a systematic error, we obtain the best agreement for the ZnS structure of AuC.

For all structures, we also determined the cohesive energies, i.e. the compound formation energies with respect to the most stable elemental structure. All calculated cohesive energies are positive. This means that the considered compounds are not thermodynamically stable. For gold carbide, the corresponding energies with respect to bulk gold and graphite indicate that it is most stable in the ZnS structure [11]. The endothermic character of its

formation explains why there are so few reports on gold carbide. As already mentioned, it was identified a long time ago, and turned out to be explosive under rapid heating and ignites at temperatures above 180 ° [1]. Its structure has not been determined yet. Note, however, that here it is assumed that AuC is not formed from graphite but rather from the hydrocarbon deposits or defects on graphene. Under electron irradiation, both could be considered as permanent source of atomic carbon.

As a further experimental fact, we observed flat crystals and cuboids with a size not larger than 20 nm and an explicit (100) surface termination. For this reason we also compared the surface energies of thin AuC films with ZnS and NaCl structure. For all calculated surface orientations, we did not find any significant surface relaxation. In case of the ZnS structure, we obtained in agreement with the experiment that the formation of a (100) surface termination should be clearly favored versus the (110) and (111) surfaces. Furthermore, our calculation shows that surfaces terminated with gold should be energetically preferred. Moreover, the calculated electronic structure of a small AuC cluster adsorbed on graphene is only slightly modified compared to the one of the isolated AuC cluster. This indicates that AuC is weakly interacting with the graphene substrate and retains its properties upon adsorption on graphene. We find that AuC is metallic, similar as the stable compound tungsten carbide, WC, whose properties we determined as a reference [11].

4. Conclusion

In summary, we presented atomically resolved *in-situ* TEM studies of the heat- and irradiation induced formation of novel gold structures on graphene. We found periodic arrangements of individual gold atoms in form of rectangularly shaped atomic monolayers and bilayers as well as entire cuboids of many atomic layers. Both the DFT calculations and EELS analysis provide clear evidence for a crystalline compound formation between gold and carbon in a zincblende structure. On the theoretical side, they are predicted to be metallic and exhibit a bulk modulus of 141 GPa. Other properties of this exciting new material remain to be explored.

Acknowledgment

We thank our collaborators Jannik C. Meyer from the group of Physics of Nanostructured Materials at the University of Vienna, Axel Groß and Xiaohang Lin from the Institute of Theoretical Chemistry at the University of Ulm and Johannes Biskupek from the Electron Microscopy Group of Materials Science at the University of Ulm for their collaboration with respect to the scientific discussion, microscope operation and DFT calculations.

References

[1] J.A. Mathews and L.L. Watters, "The carbide of gold.", *J. Am. Chem. Soc.*, vol. 22, pp. 108–111, 1900.

[2] R. Parish, "Organogold chemistry: I. structure and synthesis", *Gold Bulletin*, vol. 30, pp. 3–12, 1997.

[3] Y. Cohen, V. Bernshtein, E. Armon, A. Bekkerman, and E. Kolodney, "Formation and emission of gold and silver carbide cluster ions in a single C60 surface impact at keV energies: Experiment and calculations", *J. Chem. Phys.*, vol. 134, pp. 124701 -1–11, 2011.

[4] H. Okamoto and T. Massalski, "The Au-C (gold-carbon) system", *Bulletin of Alloy Phase Diagrams*, vol. 5, pp. 378–379, 1984.

[5] N. Seriani, F. Mittendorfer, and G. Kresse, "Carbon in palladium catalysts: a metastable carbide", *J. Chem. Phys.*, vol. 132, pp. 024711-1–8, 2010.

[6] J. Nishijo, C. Okabe, O. Oishi, and N. Nishi, "Synthesis, structures and magnetic properties of carbon-encapsulated nanoparticles via thermal decomposition of metal acetylide", *Carbon*, vol. 44, pp. 2943–2949, 2006.

[7] J.W. Menter, "The direct study by electron microscopy of crystal lattices and their imperfections", *Proc. R. Soc. Lond.* , vol. 236, pp. 119–135, 1956.

[8] F.M. Ross, "In situ Transmission electron microscopy", in *Science of Microscopy*, P.W. Hawkes and J.C.H. Spence (Eds.), pp. 445–534, Springer New York, 2007.

[9] B. Westenfelder, J.C. Meyer, J. Biskupek, G. Algara-Siller, L.G. Lechner, J. Kusterer, U. Kaiser, C.E. Krill III, E. Kohn, and F. Scholz, "Graphene-based sample supports for in situ high-resolution TEM electrical investigations", *J. Phys. D: Appl. Phys.*, vol. 44, pp. 055502-1–7, 2011.

[10] B. Westenfelder, J.C. Meyer, J. Biskupek, S. Kurasch, F. Scholz, C.E. Krill III, and U. Kaiser, "Transformations of carbon adsorbates on graphene substrates under extreme heat", *Nano Letters*, vol. 11, pp. 5123–5127, 2011.

[11] B. Westenfelder, J. Biskupek, J.C. Meyer, S. Kurasch, X. Lin, F. Scholz, A. Groß and U. Kaiser, "Bottom-up formation of robust gold carbide", *to be submitted*, 2014.

[12] E. Sutter, P. Sutter, and Y. Zhu, "Assembly and interaction of Au/C core-shell nanostructures: in situ observation in the transmission electron microscope", *Nano Lett.*, vol. 5, pp. 2092–2096, 2005.

[13] A.S. Barnard, N.P. Young, A.I. Kirkland, M.A. van Huis, and H. Xu, "Nanogold: a quantitative phase map", *ACS Nano*, vol. 3, pp. 1431–1436, 2009.

[14] P. Buffat and J.P. Borel, "Size effect on the melting temperature of gold particles", *Phys. Rev. A*, vol. 13, pp. 2287–2298, 2000.

[15] P. Jensen, X. Blase, and P. Ordejón, "First principles study of gold adsorption and diffusion on graphite", *Surface Science*, vol. 564, pp. 173–178, 2004.

[16] O. Cretu, A.V. Krasheninnikov, J.A. Rodríguez-Manzo, L. Sun, R.M. Nieminen, and F. Banhart, "Migration and localization of metal atoms on strained graphene", *Phys. Rev. Lett.*, vol. 105, pp. 196102-1–4, 2010.

[17] K. Urban and A. Seeger, "Radiation-induced diffusion of point-defects during low-temperature electron irradiation", *Phil. Mag.*, vol. 30, pp. 1478–6435, 1974.

[18] F. Banhart, "Irradiation effects in carbon nanostructures", *Rep. Prog. Phys.*, vol. 62, pp. 1181–1221, 1999.

[19] J. Wang, G. Wang, and J. Zhao, "Density-functional study of Au_n (n = 2–20) clusters: lowest-energy structures and electronic properties", *Phys. Rev. B*, vol. 66, pp. 035418-1–6, 2002.

[20] J.C. Meyer, A.K. Geim, M.I. Katsnelson, K.S. Novoselov, D. Obergfell, S. Roth, C.O. Girit, and A. Zettl, "On the roughness of single- and bi-layer graphene membranes", *Solid State Commun.*, vol. 143, pp. 101–109, 2007.

[21] J.C. Meyer, A.K. Geim, M.I. Katsnelson, T.J. Booth, K.S. Novoselov, and S. Roth, "The structure of suspended graphene sheets", *Nature*, vol. 446, pp. 60–63, 2007.

[22] K. Suenaga, Y. Iizumi, and T. Okazaki, "Single atom spectroscopy with reduced delocalization effect using a 30 kV-STEM", *Eur. Phys. J. Appl. Phys.*, vol. 54, pp. 33508-1–4, 2011.

[23] M. Lischka and A. Groß, "Hydrogen adsorption on an open metal surface: H_2/Pd(210)", *Phys. Rev. B*, vol. 65, pp. 075420-1–8, 2002.

[24] M. Lischka, C. Mosch, and A. Groß, "Tuning catalytic properties of bimetallic surfaces: oxygen adsorption on pseudomorphic Pt/Ru overlayers", *Electrochimica Acta*, vol. 52, pp. 2219–2228, 2007.

Frequency Doubled High-Power Semiconductor Disk Lasers for Projection and Ion-Trapping Applications

Alexander Hein

We present optically pumped semiconductor disk lasers (OPSDLs) emitting in the 900–1100 nm band which are frequency doubled to access the visible spectrum. In particular, we focus on presenting the design, fabrication, and specific characteristics. Fundamental outputs exceeding 25 W and visible radiation with powers greater than 11 W are achieved. The blue and green emission at wavelengths around 450–470 and 520–540 nm yield advantageous gamuts for projection applications. Moreover, other accessible wavelengths in this spectral region, e.g. 493 nm, single frequency operation, and the good beam quality of these devices enable optical ion trapping experiments.

1. Introduction

Optically pumped semiconductor disk lasers, also called vertical-external-cavity surface-emitting lasers (VECSELs), are a relatively novel class of semiconductor lasers which combine high output powers and excellent beam qualities [1, 2]. The basic principle of a semiconductor disk laser is illustrated in Fig. 1. The semiconductor disk, which is mounted on a heat spreader and a heat sink, forms a stable resonator together with the external concave mirror. Optical pumping of the semiconductor disk is provided by a pump laser system equipped with fiber coupled broad-area edge-emitting laser diodes. More complex cavities with additional external mirrors, miniaturized systems, as well as multiple-chip resonators have been realized [3]. The easily accessible external resonator and high intra-cavity field intensities make OPSDLs highly suitable for the generation of higher harmonics. Combining epitaxial structures from the well established AlGaAs-GaAs-InGaAs material system and second-harmonic (SH) generation, wavelengths in the visible spectrum starting from blue [4,5], green [4,6] to yellow [7] with high optical outputs can be addressed. Frequency-quadrupled systems reaching into the UV for environmental sensing, chemical detection, and lidar application, as well as for high-resolution spectroscopy [8, 9] and ion cooling [10] were also demonstrated and attract more and more interest.

Moreover, semiconductor disk lasers have not only unsurpassed freedom in the choice of the emission wavelength. Since design and material composition of the epitaxial structure can be widely varied and drawing on the fact that absorption in the semiconductor material above the band gap is extremely high and not limited to a very narrow band, optical pumping is not limited to discrete wavelengths [11], and the spectral requirements for the pump sources are drastically reduced as compared to diode-pumped solid-state lasers.

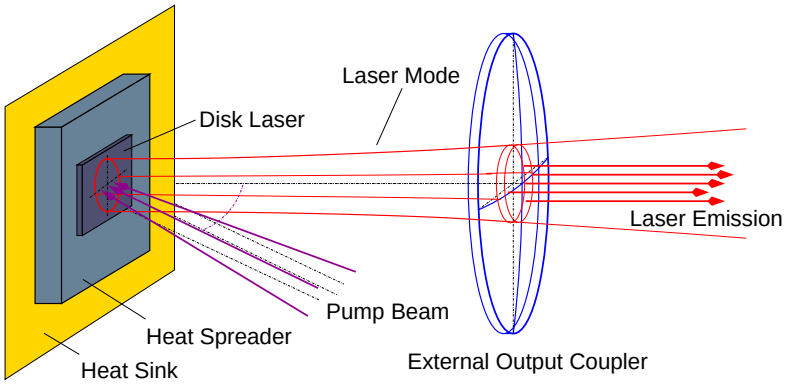

Fig. 1: Schematic illustration of a semiconductor disk laser. The stable hemispheric laser resonator consisting of the semiconductor disk and an external concave mirror provides fundamental transverse-mode operation.

Being able to tailor the wavelength, these devices are suited as illumination sources in stereoscopic 3D-projection [12] since the required channel separation can be achieved without sacrificing the optimum gamuts. Here, especially the green spectral region (520–540 nm) is of interest, but also the blue and red bands can be realized with OPSDL technology [3]. Furthermore, the cyan emission around 493 nm enables optical trapping of Ba-ions since this laser line is on resonance with the atomic transition. The presented work is focused on the design, fabrication and respective characteristics of 520 and 493 nm emitting VECSELs.

2. Design and Fabrication

2.1 Layer design

Key elements in the layer design are a dielectric anti-reflection (AR) coating, a resonant periodic gain (RPG) structure, and a rear distributed Bragg reflector (DBR). The layer structure is depicted in more detail in Fig. 2. For the DBR an alternating stack of 56 $Al_{0.15}Ga_{0.85}As$/AlAs layers was chosen. With this material configuration, the DBR provides a high reflectivity for the emission wavelength ($R > 99.9\,\%$) but is non-absorbing for the pump wavelength of 804 nm. The absorption of the pump radiation only takes place in the gain region while all other layers are optically transparent.

Due to the transparency of the DBR and a Ti/Au metalization which terminates the semiconductor layer structure, the pump light is reflected back into the active region, thus, providing a resonant pumping condition. There is decay originating from absorption in the GaAs capping layer and the Ti layer, hence, these layers should be kept rather thin. An alternative approach to the metal reflector is to utilize a double-band DBR, providing high reflectivities for both the emission and the pump wavelength [5, 13]. Targeting wavelengths beyond 1 µm, such structures with two highly reflecting bands will result in an increased thermal impedance and demand a more complex epitaxial growth [14]. As illustrated on the right hand side of Fig. 2, the semiconductor surface is located in a

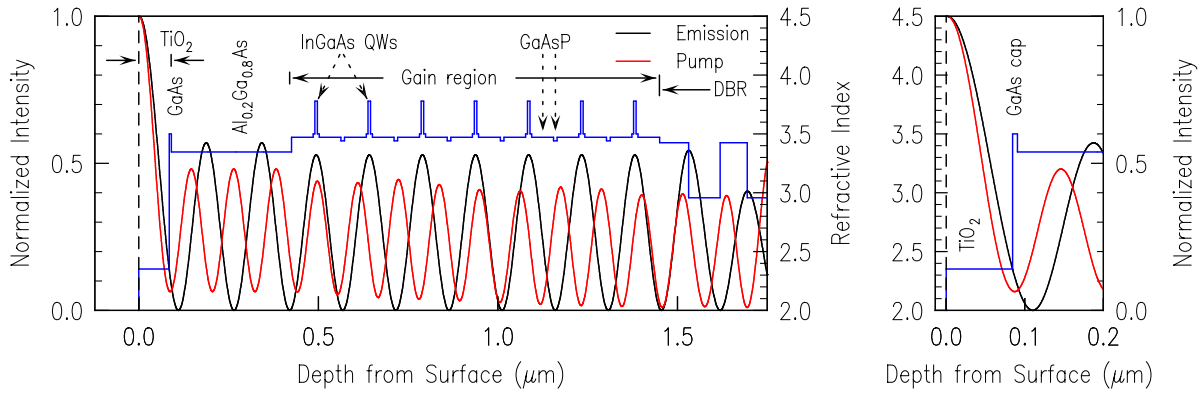

Fig. 2: Layer structure of a device designed for an emission wavelength of 1040 nm. The Bragg reflector is indicated with the first couple of mirror pairs. The interface semiconductor/dielectric is shown in more detail. The node position of the field intensity for the two respective wavelengths is located at the semiconductor/dielectric interface where absorption is reduced to a minimum.

node of the electric-field intensity of the standing-wave patterns. Due to surface states inside the band gap, the semiconductor surface would exhibit high optical absorption for the pump light and also for the laser light ($\lambda < 1\,\mu$m) at this position. Our approach to circumvent the high absorption is a quarter-wavelength dielectric surface coating on the semiconductor surface [15]. For one, the layer serves as an AR-coating for the pump wavelength and passivates the surface, on the other hand the interface absorption is minimized by relocating the antinode. Spectral characteristics of a device designed for 1040 nm emission are summarized in Fig. 3. Due to the separation of the excitonic dip and the subcavity resonance in the reflectivity spectra [6] by varying the angle of incidence, the spectral behavior can be fully analyzed. The photoluminescence (PL) measurements provide the optimum operating temperature when the PL of the QWs has the best overlap with the subcavity resonance.

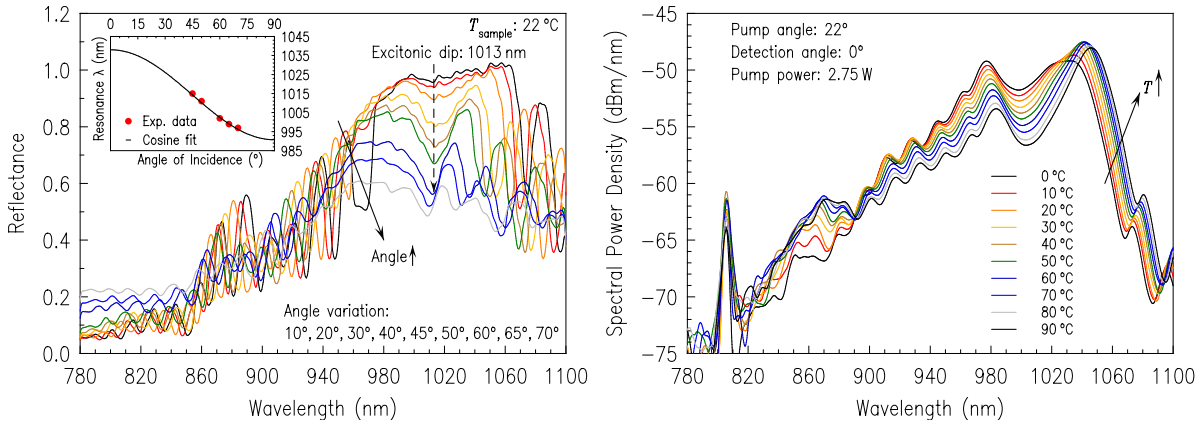

Fig. 3: Angle resolved reflectivity spectra (left) and temperature dependent surface photoluminescence (right).

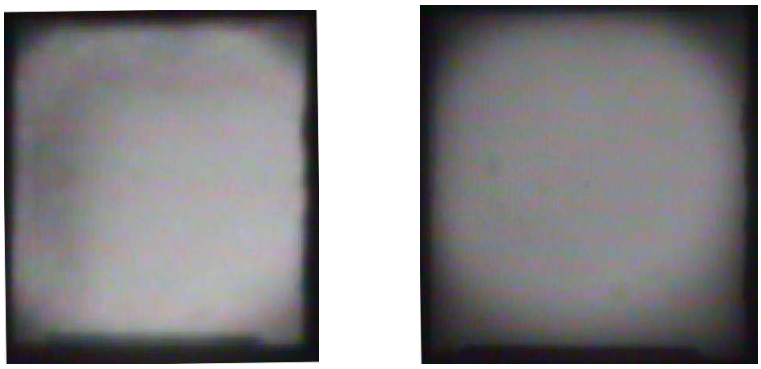

Fig. 4: Locally resolved photoluminescence of a 1.5 mm×1.8 mm disk laser before (left) and after (right) operation, where possible crystal defects could be visualized as dark lines or a dark cross-hatch pattern.

A further and probably most important point that has to be addressed is the strain in the semiconductor structure. Incorporating indium into the QWs results in pseudomorphic growth of the crystal lattice which is more and more compressively strained. Although strained QWs show clear advantages in gain characteristics [16], relaxations of these layers result in line defects of the crystal structure. Compensation of the compressive strain from the InGaAs QWs was realized by tensilely strained GaAsP barriers. In order not to create a strong strain gradient at the well/barrier interface a step of pure GaAs was introduced as a mediator. The structural quality of the devices can be easily assessed by local photoluminescence where the full chip area is excited with the pump laser. Figure 4 shows a locally resolved photoluminescence picture of a device before and after operation at an output power in excess of 20 W that has no defect dislocations at all. Efficient and long-living semiconductor disk lasers should be completely free of these line defects.

2.2 Mounting and processing

The devices were grown in reverse order – RPG first, DBR last – by solid-source molecular beam epitaxy (MBE) on (100)-oriented GaAs substrates and soldered upside-down onto heat spreaders and heat sinks with indium. The soldering happens in an inert nitrogen atmosphere where formic acid is added temporarily as a suitable flux for indium. Afterwards, the substrate is removed by wet-chemical etching leaving only the epitaxially grown layer stack [17]. Precise etching control is achieved with a sequence of etch stop layers (AlAs/GaAs/AlAs) with high selectivities for the respective etchants. On the left hand side of Fig. 5 a scanning electron microscope (SEM) image of an upside-down mounted device with substrate is shown. In operation, the generated heat is spread by the chemically vapor deposited (CVD) diamond and transfered to the heat sink. Alternatively, optically transparent diamond with high thermal conductivity can be used to remove the heat from the front side of the as-grown disk lasers [7]. The right part of Fig. 5 shows a processed chip with the substrate and etch stop layers fully removed exposing the capping layer. The dielectric coating is applied in the final step.

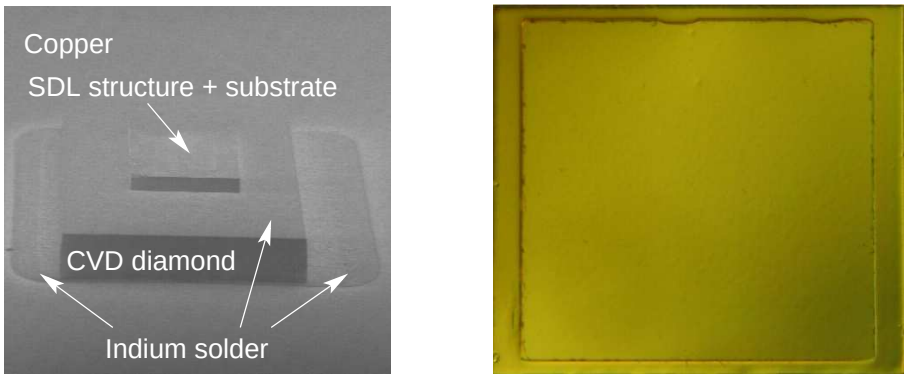

Fig. 5: SEM image of an upside-down soldered SDL structure with substrate on a diamond heat spreader and copper heat sink (left) and the surface photograph of a fully processed laser chip after substrate removal (right).

3. Characterization

3.1 Fundamental regime

The devices were tested in a straight cavity with a curved output coupler having a radius of curvature of -150 mm. The SDL structure was pumped by a fiber coupled module with an emission around 804 nm into a spot of approximately 500 μm diameter confirmed by measuring the illuminated area. The pump light was incident at an angle of 22° to the chip surface normal giving a slight ellipticity. The temperature was controlled with a commercial thermoelectric Peltier cooler. The Peltier element in turn was contact cooled via a copper mount with running water. At a heat sink temperature of 17 °C, more than 25 W of output power were generated in transverse multi-mode operation with a slope efficiency close to 50 % as depicted in Fig. 6. The devices are capable of operating at heat sink temperatures of 90 °C with optical outputs of up to 3.5 W and slope efficiencies of 25 % [19]. Throughout the whole operation range, we observed an almost constant absorptance of 91 % of the pump power. This high degree of absorptance underlines the importance of the dielectric surface coating and the metal reflector completing the DBR in order to increase the overall efficiency. The overall efficiency (incident power-to-output power) for optical outputs around 20 W was 40–43 %. The increase of the wavelength with absorbed pump power was 0.13 nm/W indicating good heat conduction, and the total wavelength shift was approximately 7 nm from threshold to power saturation as indicated by the spectra in the inset.

3.2 Second-harmonic regime

The external cavity of OPSDLs allows efficient intra-cavity SH generation due to high field intensities inside the resonator. Figure 7 shows the cavity setup of a folded resonator with nonlinear crystal and birefringent quartz filter plate (BRF) [6] tilted to the Brewster angle for linear polarization. This resonator configuration with the folding mirror located

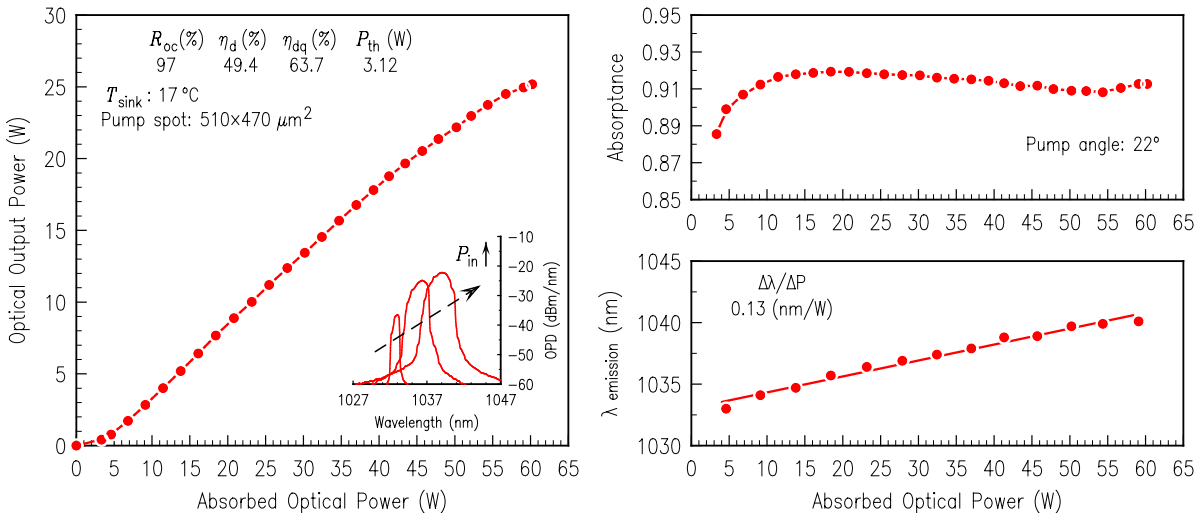

Fig. 6: Output power characteristics of a semiconductor disk laser designed for an emission at 1040 nm. The pumped spot size was $510 \times 470\,\mu m^2$. The device was operated with an output coupler reflectivity of 97 %.

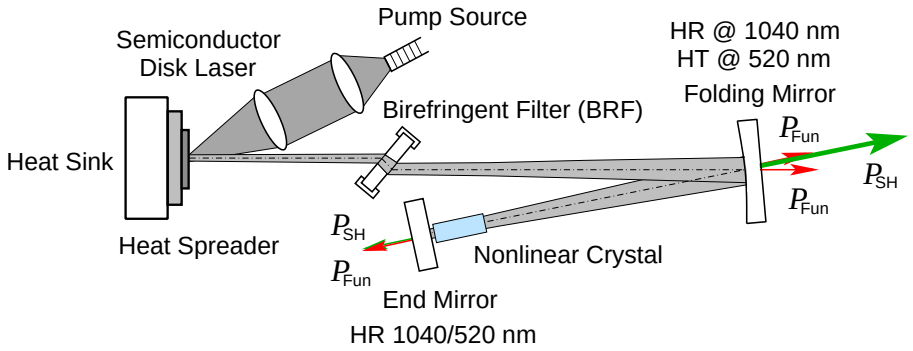

Fig. 7: Schematic setup of a folded V-type cavity for second-harmonic generation. Wavelength and polarization control are realized by the use of a birefringent quartz filter plate tilted to the Brewster angle.

further away from the disk laser than twice the focal length of the mirror yields a strong reduction of the beam waist in the nonlinear crystal in order to achieve higher intensities.

3.3 Green-emitting OPSDLs for stereo projection

Using the cavity setup illustrated in Fig. 7, we have obtained an output power in excess of 11 W and conversion efficiencies of 23 % at a wavelength of 519 nm. The output characteristic is provided in Fig. 8. The frequency conversion was realized by type-I critical phase-matching. The nonlinear 11 mm-long lithium triborate (LBO) crystal was stabilized to a temperature of 40 °C while the heat-sink temperature was 17 °C. Control and narrowing of the emission wavelength was realized by rotating a 2 mm-thick BRF plate.

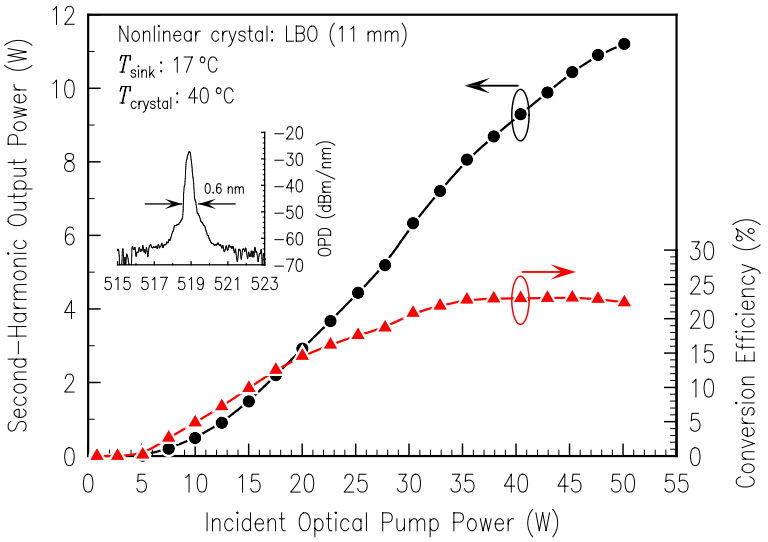

Fig. 8: Output power characteristic and emission spectrum of the second-harmonic emission of a frequency-doubled semiconductor disk laser at 519 nm. A maximum output power of 11.2 W and a conversion efficiency of 23 % with respect to the incident pump power were achieved.

3.4 Cyan-emitting OPSDLs for ion trapping

For off-resonance trapping of the Ba-ion an emission wavelength of 493.3 nm is desirable, which is a couple of 100 GHz detuned with respect to the $6S_{1/2}$-$6P_{1/2}$ transition, as indicated in Fig. 9. This optical trap prevents the longitudinal micro-motion of the 138Ba-ion while the transverse micro-motion is foreclosed by a Paul trap. To address this, OPSDLs with a fundamental emission around 986.6 nm are required and should deliver watt-level power in the second-harmonic regime at a good beam quality. Further, the linewidth should be restricted to smaller values than 1 GHz and the source must operate on a single longitudinal mode. OPSDL devices intrinsically show narrow linewidth behavior of the individual peaks capable of delivering widths in the kHz-range. However, due to relatively long resonators and the consequent small mode spacing, typically pm-range, true single-frequency operation demands additional elements for frequency stabilization, or an active stabilization of the cavity is required [9]. We modified an OPSDL structure that was originally designed for an emission at 976 nm with a thicker dielectric coating to red-shift the emission. Fig. 10 shows the second-harmonic output characteristics of this device. It should be noted that here the device was directly mounted on a gold-platted copper heat sink, and no CVD diamond heat spreader was used. Detuning the laser from its optimum wavelength of 979.5 nm to the trap wavelength of 986.6 nm with a 4 mm thick BRF resulted in a power penalty for the SH of about 1.3 W. After insertion of an uncoated yttrium aluminum garnet (YAG) etalon to obtain single-frequency operation, the SH output power further dropped to roughly 500 mW. The corresponding spectra are depicted in the top-right part of Fig. 10. The poor conversion efficiency of about 2.5 % is a result of detuning the fundamental laser line by more than 7 nm from optimal conditions and insufficient thermal management.

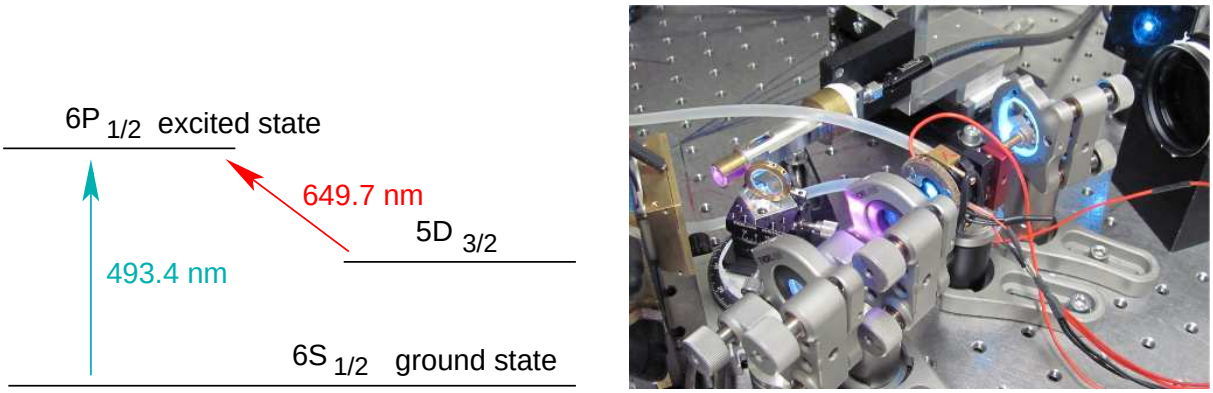

Fig. 9: Laser transitions for the 138Ba ion (left). V-type cavity arrangement for a frequency doubled OPSDL with two concave external mirrors incorporating a BRF, a solid YAG etalon, and a nonlinear crystal with temperature stabilization to generate single-frequency emission at 493.3 nm (right).

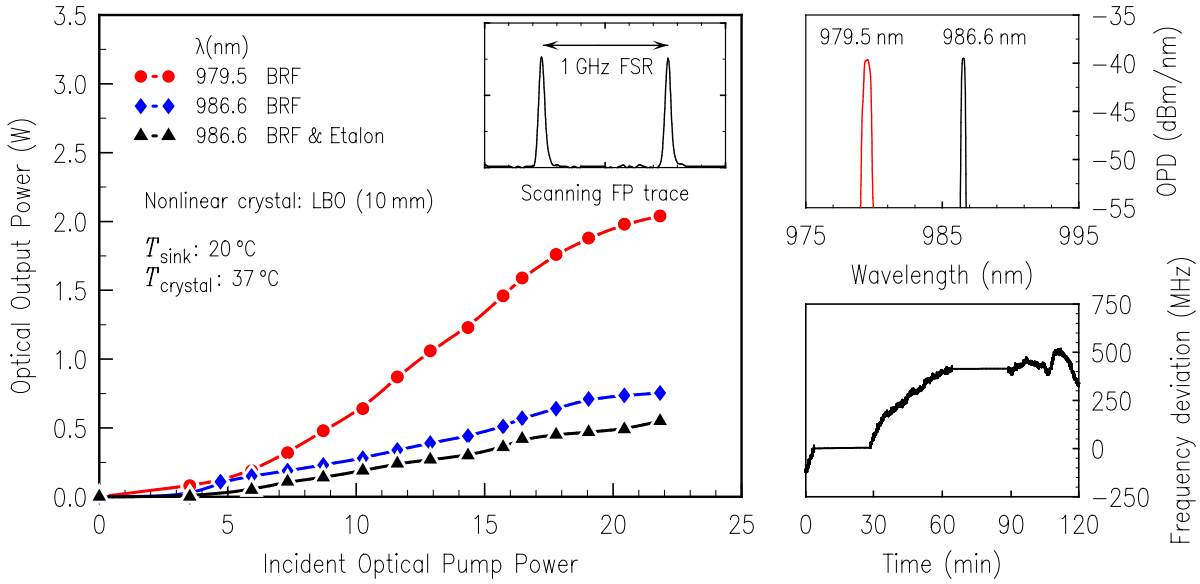

Fig. 10: Left: Frequency doubled output of the ion trap OPSDL. The inset shows the frequency spectrum obtained with a scanning Fabry–Pérot interferometer confirming single-frequency operation and linewidth of approximately 40 MHz. Right: Optical spectra (top) and frequency behavior over time (bottom).

Single-frequency operation was analyzed with a scanning Fabry–Pérot interferometer having a FSR of 1 GHz as indicated in the inset. Even though the setup was not shielded from external disturbances we observed single-frequency operation throughout the whole operation range with a linewidth of approximately 40 MHz. The linewidth could be reduced to 25 MHz by decresing the water throughput for cooling. Further, the frequency deviation from the reference value of 303.6448 THz on a time scale of two hours was only slightly more than 500 MHz, and thus, well within the experiment-required specifications.

4. Conclusion

We demonstrated frequency doubled optically pumped semiconductor disk lasers that are highly suitable for projection applications and off-resonance trapping of ions. Our results and works published by other groups with further frequency conversion show that this type of lasers with its unmatched flexibility in addressing wavelengths from the UV to the mid IR and its tuning abilities can become a well-established technology in a large variety of laser-based optical systems.

Acknowledgment

The assistance of Susanne Menzel and Rudolf Rösch with growth and device processing as well as of Andreas Ziegler with various measurements is gratefully acknowledged.

References

[1] M. Kuznetsov, F. Hakimi, R. Sprague, and A. Mooradian, "Design and characteristics of high-power (>0.5-W CW) diode-pumped vertical-external-cavity surface-emitting semiconductor lasers with circular TEM_{00} beams," *IEEE J. Select. Topics Quantum Electron.* vol. 5, no. 3, pp. 561–573, 1999.

[2] O.G. Okhotnikov (Ed.), *Semiconductor Disk Lasers – Physics and Technology*, Wiley-VCH, Weinheim, 2010.

[3] S. Calvez, J.E. Hastie, M. Guina, O.G. Okhotnikov, and M.D. Dawson, "Semiconductor disk lasers for the generation of visible and ultraviolet radiation," *Laser and Photon. Rev.* vol. 3 no. 5, pp. 407–434, 2009.

[4] L.E. Hunziker, C. Ihli, and D.S. Steingrube, "Miniaturization and power scaling of fundamental mode optically pumped semiconductor lasers," *IEEE J. Select. Topics Quantum Electron.* vol. 13, no. 3, pp. 610–618, 2007.

[5] A. Hein, F. Demaria, A. Kern, S. Menzel, F. Rinaldi, R. Rösch, and P. Unger, "Efficient 460-nm second-harmonic generation with optically pumped semiconductor disk lasers," *IEEE Photon. Technol. Lett.* vol. 23, no. 3, pp. 179–181, 2011.

[6] A. Hein, S. Menzel, and P. Unger, "High-power high-efficiency optically pumped semiconductor disk lasers in the green spectral region with a broad tuning range," *Appl. Phys. Lett.* vol. 101, pp. 111109-1–4, 2012.

[7] W.J. Alford, G.J. Fetzer, R.J. Epstein, Sandalphon, N. Van Lieu, S. Ranta, M. Tavast, T. Leinonen, and M. Guina, "Optically pumped semiconductor lasers for precision spectroscopic applications," *IEEE J. Quantum Electron.* vol. 49, no. 8, pp. 719–727, 2013.

[8] Y. Kaneda, M. Fallahi, J. Hader, J.V. Moloney, S.W. Koch, B. Kunert, and W. Stolz, "Continuous-wave single-frequency 295 nm laser source by a frequency-quadrupled optically pumped semiconductor laser," *Opt. Lett.* vol. 34, no. 22, pp. 3511–3513, 2009.

[9] J. Paul, Y. Kaneda, T.L. Wang, C. Lytle, J.V. Moloney, and R.J. Jones, "Doppler-free spectroscopy of mercury at 253.7 nm using a high-power, frequency-quadrupled, optically pumped external-cavity semiconductor laser," *Opt. Lett.* vol. 36, no. 1, pp. 61–63, 2011.

[10] S. Ranta, M. Tavast, T. Leinonen, R. Epstein, and M. Guina, "Narrow linewidth 1118/559 nm VECSEL based on strain compensated GaInAs/GaAs quantum wells for laser cooling of Mg-ions," *Opt. Mater. Exp.* vol. 2, no. 8, pp. 1011–1019, 2012.

[11] S. Haupt, M. Furitsch, H.H. Lindberg, I. Pietzonka, U. Strauß, and G. Bacher, "Analysis of the pump wavelength dependence of a 1060-nm VECSEL," *IEEE Photon. Technol. Lett.* vol 24, no. 5, pp. 341–343, 2012.

[12] H. Jorke, A. Simon, and M. Fritz, "Advanced stereo projection using interference filters," *J. Soc. Inf. Disp.* vol. 17, no. 5, pp. 407–410, 2009.

[13] K.-S. Kim, J. Yoo, Kim, G., S. Lee, S. Cho, J. Kim, T. Kim, and Y. Park, "Enhancement of pumping efficiency in a vertical-external-cavity surface-emitting laser," *IEEE Photon. Technol. Lett.* vol. 19, no. 23, pp. 1925–1927, 2007.

[14] L. Fan, C. Hessenius, M. Fallahi, J. Hader, H. Li, J.V. Moloney, W. Stolz, S.W. Koch, J.T. Murray, and R. Bedford, "Highly strained InGaAs/GaAs multiwatt vertical-external-cavity surface-emitting laser emitting around 1170 nm," *Appl. Phys. Lett.* vol. 91, pp. 131114-1–3, 2007.

[15] F. Demaria, S. Lorch, S. Menzel, M.C. Riedl, F. Rinaldi, R. Rösch, and P. Unger, "Design of highly efficient high-power optically pumped semiconductor disk lasers," *IEEE J. Select. Topics Quantum Electron.* vol. 15, no. 3, pp. 973–977, 2009.

[16] L.A. Coldren and S. Corzine, *Diode Lasers and Photonic Intergrated Circuits*, John Wiley & Sons Inc., New York, 1995.

[17] E. Gerster, I. Ecker, S. Lorch, C. Hahn, S. Menzel, and P. Unger, "Orange-emitting frequency-doubled GaAsSb/GaAs semiconductor disk laser," *J. Appl. Phys.* vol. 94, no. 12, pp. 7397–7401, 2003.

[18] B. Heinen, T.-L. Wang, M. Sparenberg, A. Weber, B. Kunert, J. Hader, S.W. Koch, J.V. Moloney, M. Koch, and W. Stolz, "106 W continuous-wave output power from vertical-external-cavity surface-emitting laser," *Electron. Lett.* vol. 48, no. 9, pp. 516–517, 2012.

[19] P. Unger, A. Hein, F. Demaria, M. Susanne, M. Rampp, and A. Ziegler, "Design of high-efficiency semiconductor disk lasers," Proc. SPIE 8606, pp. 860602-1–8, 2013.

Ph.D. Thesis

1. Hendrik Roscher,
   Surface-Mount Vertical-Cavity Laser Diodes for Cost-Sensitive High-Speed Applications,
   Nov. 2013.

Diploma and Master Theses

1. SK. Shaid-Ur Rahman,
   Optimization of Optoelectronic Device Structures on Freestanding Galliumnitride Templates,
   Master Thesis, January 2013.

2. Sareh Esmaeily Sabet Roudsari,
   Optimization of a Reactive Ion Etching Processs for Silicon using SF_6,
   Master Thesis, March 2013

3. Jose Antonio Martos Calahorro,
   Optical Manipulation of Microparticles With Integrated Bottom-Emitting VCSEL Arrays,
   Master Thesis, March 2013.

4. Ashkan Moradabadi,
   Characterization of Edge-Emitting Semiconductor Diode Lasers,
   Master Thesis, March 2013.

5. Sebastian Griffel,
   Herstellung und Charakterisierung integrierbarer Vertikallaserdiodenarrays,
   Master Thesis, March 2013.

6. Philipp Schustek,
   Untersuchungen zur Herstellung von semipolaren GaN-Quasisubstraten,
   Diploma Thesis, July 2013.

7. Sabine Schörner,
   Optische und elektrische Messungen an semipolaren LEDs auf strukturiertem Saphir,
   Master Thesis, September 2013.

8. Md. Saiful Alam,
   InGaN/GaN Based Semipolar Green Light Emitting Diodes,
   Master Thesis, November 2013.

9. Guanbai He,
   Growth Studies on N-polar GaN Nanowires,
   Master Thesis, October 2013.

10. Maryam Alimoradi Jazi,
    Investigation of (20-21) GaN Epitaxially Grown on (22-43) Patterned Sapphire Substrates,
    Master Thesis, November 2013.

11. Huiying Huang,
Fabrication and Characterization of a Wavelength-Tunable Current-Injection Quantum Photon Emitter,
Master Thesis, November 2013.

Bachelor Thesis

1. Mustafa Kazu,
   Charakterisierung von Laserdioden und Cs-Gaszellen für miniaturisierte Atomuhren,
   March 2013.

Talks and Conference Contributions

[1] A. Bergmann, A. Hein, and R. Michalzik, "Vertical-cavity surface-emitting laser arrays for miniaturized integrated optical lattice modules", *Conf. on Lasers and Electro-Optics Europe, CLEO/Europe 2013*, Munich, Germany, May 2013.

[2] A. Bergmann, J.A. Martos Calahorro, A. Hein, D. Wahl, and R. Michalzik, "Miniaturized sorting by optical lattices based on integrated vertical-cavity laser diodes", *2nd EOS Conference on Optofluidics, EOSOF 2013*, Munich, Germany, May 2013.

[3] M. Caliebe, T. Meisch, S. Lazarev, S. Bauer, and F. Scholz, "Crystal quality improvement of MOVPE grown semipolar GaN on prestructured sapphire substrates", poster at *15th European Workshop on Metalorganic Vapour Phase Epitaxy, EWMOVPE XV*, Aachen, Germany, June 2013.

[4] M. Caliebe, T. Meisch, B. Neuschl, K. Thonke, and F. Scholz, "Crystal quality improvement of MOVPE grown semipolar GaN on prestructured sapphire substrates", poster at *10th International Conference on Nitride Semiconductors, ICNS*, Washington, D.C., USA, Aug. 2013.

[5] M. Caliebe, T. Meisch, Z. Cheng, B. Neuschl, S. Bauer, J. Helbing, K. Thonke, Y. Han, S. Lazarev, S. Bauer, and F. Scholz, "Investigations about SiN interlayers in $(11\bar{2}2)$ GaN layers grown on patterned substrates", *PolarCon Summerschool*, Wernigerode, Germany, Sept. 2013.

[6] M. Caliebe, T. Meisch, Z. Cheng, and F. Scholz, "Influence of sapphire miscut on $(11\bar{2}2)$ oriented GaN grown by MOVPE on pre-structured sapphire substrates", *28th DGKK Workshop on Epitaxy of III-V-Semiconductors*, Ilmenau, Germany, Dec. 2013.

[7] A. Hein, S. Menzel, A. Ziegler, R. Rösch, and P. Unger "Frequency doubled high-power semiconductor disk lasers for stereo projection and ion traps", *SPIE Optics + Photonics 2013, Photonic Fiber and Crystal Devices: Advances in Materials and Innovations in Device Applications VII*, San Diego, CA, USA, Aug. 2013.

[8] A. Hein, "Optically pumped semiconductor disk lasers: design, growth, characterization and potential applications" seminar talk, *Physics and Astronomy Department, University of Southampton*, Southampton, United Kingdom, Nov. 2013.

[9] D. Heinz, M. Fikry, G. He, I. Tischer, M. Madel, K. Thonke, and F. Scholz, "Realization of nitrogen-polar GaN structures and layers by MOVPE", poster at *15th European Workshop on Metalorganic Vapour Phase Epitaxy, EWMOVPE XV*, Aachen, Germany, June 2013.

[10] D. Heinz, M. Fikry, T. Meisch, M. Madel, S. Bauer, F. Huber, M. Hocker, I. Tischer, M. Frey, B. Neuschl, K. Thonke, and F. Scholz, "Growth of GaN micro- and nanostructures for sensor applications", poster at *Forschungstag BW-Stiftung*, Stuttgart, Germany, July 2013.

[11] D. Heinz, M. Fikry, T. Aschenbrenner, M. Schowalter, T. Meisch, M. Madel, F. Huber, M. Hocker, M. Frey, I. Tischer, B. Neuschl, T. Mehrtens, K. Müller, A. Rosenauer, D. Hommel, K. Thonke, and F. Scholz, "GaN nanotubes with coaxial GaInN quantum wells", *10th International Conference on Nitride Semiconductors, ICNS*, Washington, D.C., USA, Aug. 2013.

[12] D. Heinz, F. Huber, M. Madel, M. Fikry, I. Tischer, M. Frey, S. Bauer, J. Jakob, K. Thonke, and F. Scholz, "Coaxial Ga(In)N heterostructures grown on ZnO nanowires", *SemiconNano*, Lake Arrowhead, CA, USA, Oct. 2013.

[13] D. Heinz, M. Fikry, T. Aschenbrenner, M. Schowalter, T. Meisch, M. Madel, F. Huber, M. Hocker, I. Tischer, T. Mehrtens, K. Müller, G. He, M. Frey, J. Jakob, B. Neuschl, D. Hommel, A. Rosenauer, K. Thonke, and F. Scholz, "Ga(In)N micro- and nanostructures for optical gas sensing", poster at *Statusworkshop Kompetenznetz "Funktionelle Nanostrukturen"*, Bad Herrenalb, Germany, Oct. 2013.

[14] D. Heinz, G. He, O. Rettig, R.A.R. Leute, M. Madel, F. Huber, M. Hocker, I. Tischer, B. Neuschl, K. Thonke, and F. Scholz, "Investigations of N-polar GaN micro- and nanostructures grown by MOVPE", *28th DGKK Workshop on Epitaxy of III-V-Semiconductors*, Ilmenau, Germany, Dec. 2013.

[15] N.I. Khan, A. Bergmann, and R. Michalzik, "Fabrication of integration-capable surface-relief VCSEL arrays for miniaturized optical manipulation of microparticles", *2nd Int. Conf. on Advances in Electr. Engin., ICAEE*, Dhaka, Bangladesh, Dec. 2013.

[16] R.A.R. Leute, J. Wang, T. Meisch, and F. Scholz, "Growth studies on submicrometer-sized GaN stripes with semipolar QWs", *DPG Spring Meeting*, Regensburg, Germany, Mar. 2013.

[17] R.A.R. Leute, T. Meisch, J. Wang, J. Biskupek, U. Kaiser, M. Müller, P. Veit, F. Bertram, J. Christen, and F. Scholz, "GaN laser structure with semipolar quantum wells and embedded nanostripes", *10th Conf. on Lasers and Electro-Optics Pacific Rim (CLEO-PR)*, Kyoto, Japan, June 2013.

[18] R.A.R. Leute, D. Heinz, J. Wang, T. Meisch, and F. Scholz, "Nanolithographic patterning for selective area epitaxy of gallium nitride", *DGKK Workshop Epitaxie von III/V-Halbleitern*, Ilmenau, Germany, Dec. 2013.

[19] T. Meisch, S. Schörner, J. Wang, K. Thonke, and F. Scholz, "InGaN quantum wells grown on 2" semipolar GaN", *DPG Spring Meeting*, Regensburg, Germany, Mar. 2013.

[20] T. Meisch and F. Scholz, "MOVPE growth of semipolar $(20\bar{2}1)$ GaN on $(22\bar{4}3)$ 2" patterned sapphire substrates", poster at *15th European Workshop on Metalorganic Vapour Phase Epitaxy, EWMOVPE XV*, Aachen, Germany, June 2013.

[21] T. Meisch and F. Scholz, "$(20\bar{2}1)$ GaN grown on 2" patterned sapphire substrates", poster at *10th International Conference on Nitride Semiconductors, ICNS*, Washington, D.C., USA, Aug. 2013.

[22] T. Meisch, F. Scholz, J. Wang, S. Schörner, B. Neuschl, S. Bauer, K. Thonke, H. Bremers, and A. Hangleiter, "InGaN quantum wells grown on 2" GaN – a comparison between (0001), $(10\bar{1}1)$ and $(11\bar{2}2)$ GaN", *10th International Conference on Nitride Semiconductors, ICNS*, Washington, D.C., USA, Aug. 2013.

[23] R. Michalzik, "Bidirectional optical transmission over multimode fibers" (in German), Working Group *Optical Communications* within the Photonics BW Association, Stuttgart, Germany, Feb. 2013.

[24] R. Michalzik, M.J. Miah, A. Al-Samaneh, and D. Wahl, "Dynamic characteristics of inverted grating relief VCSELs for Cs-based microscale atomic clocks", *Conf. on Lasers and Electro-Optics Europe, CLEO/Europe 2013*, Munich, Germany, May 2013.

[25] F. Scholz, T. Meisch, S. Schwaiger, S. Schörner, M. Caliebe, P. Schustek, S. Metzner, F. Bertram, T. Hempel, J. Christen, I. Tischer, K. Thonke, S. Lazarev, S. Bauer, T. Baumbach, J. Thalmair, and J. Zweck, "Semipolar GaN-based optoelectronic structures on large area substrates" (invited), *SPIE Photonics West*, San Francisco, CA, USA, Feb. 2013.

[26] F. Scholz, "Semipolar nitride structures: more efficient LEDs?", seminar talk, *Universität Paderborn*, Paderborn, Germany, July 2013.

[27] F. Scholz, T. Meisch, M. Caliebe, M. Klein, S. Schörner, B. Neuschl, K. Thonke, S. Bauer, S. Lazarev, T. Baumbach, L. Kirste, Y. Han, and C. Humphreys, "Semipolar GaInN-GaN hetero structures on large area substrates", *17th International Conference on Crystal Growth and Epitaxy, ICCGE*, Warsaw, Poland, Aug. 2013.

[28] F. Scholz, "Semipolar nitride structures: more efficient LEDs?", seminar talk, *IFW Dresden*, Dresden, Germany, Aug. 2013.

[29] F. Scholz, T. Meisch, M. Caliebe, S. Schwaiger, S. Metzner, F. Bertram, J. Christen, I. Tischer, B. Neuschl, K. Thonke, S. Lazarev, S. Bauer, T. Baumbach, H. Bremers, and A. Hangleiter, "Semipolar GaN-based optoelectronic structures on large area substrates" (invited), *International Conference and Exhibition on Lasers, Optics and Photonics, Optics-2013*, San Antonio, Texas, USA, Oct. 2013.

[30] F. Scholz, "Solid State Lighting – LEDs statt Glühbirnen: Wie funktioniert's?", *Tag der offenen Tür*, University Ulm, Germany, Nov. 2013.

[31] P. Unger, A. Hein, F. Demaria, S. Menzel, M. Rampp, and A. Ziegler "Design of high-efficiency semiconductor disk lasers" (invited tutorial), *SPIE Photonics West 2013, Vertical-External-Cavity Surface-Emitting Lasers (VECSELs) III*, San Francisco, CA, USA, Feb. 2013.

[32] J. Wang, M. Hocker, R.A.R. Leute, and F. Scholz, "InGaN/GaN based semipolar light emitting diodes", *DPG Spring Meeting*, Regensburg, Germany, Mar. 2013.

[33] J. Wang, B. Neuschl, T. Meisch, K. Thonke, and F. Scholz, "Optical absorption of c-plane and semipolar InGaN/GaN quantum wells", poster at *10th International Conference on Nitride Semiconductors, ICNS*, Washington, D.C., USA, Aug. 2013.

[34] B. Westenfelder, F. Eder, J. Kotakoski, T. Amender, J. Biskupek, S. Kurasch, F. Scholz, J.C. Meyer, and U. Kaiser, "Combining high-resolution TEM on graphene with in-situ Hall measurements", poster at *Graphene Week*, Chemnitz, Germany, June 2013.

[35] S. Bauer, B. Neuschl, I. Tischer, M. Frey, M. Hocker, R.A.R. Leute, S.S.U. Rahman, M. Klein, F. Scholz, and K. Thonke, "Microphotoluminescence studies on the effect of V-pits and the surface orientation on the indium incorporation within InGaN quantum wells on free standing polar GaN", poster at *DPG Spring Meeting*, Regensburg, Germany, Mar. 2013.

[36] S. Bauer, S. Lazarev, T. Meisch, M. Bauer, M. Barchuk, I. Tischer, T. Baumbach, V. Holy, and F. Scholz, "3D reciprocal space mapping of diffuse scattering for the study of stacking faults in semi-polar GaN layers grown from sidewalls of r-patterned sapphire substrate", poster at *15th European Workshop on Metalorganic Vapour Phase Epitaxy, EWMOVPE XV*, Aachen, Germany, June 2013.

[37] E.R. Buss, U. Rossow, H. Bremers, T. Meisch, F. Scholz, and A. Hangleiter, "Growth and characterization of $Al_{1-x}In_xN$ on different non-, and semipolar GaN surface orientations", poster at *15th European Workshop on Metalorganic Vapour Phase Epitaxy, EWMOVPE XV*, Aachen, Germany, June 2013.

[38] E.R. Buss, U. Rossow, H. Bremers, T. Meisch, F. Scholz, and A. Hangleiter, "$Al_{1-x}In_xN$ on non- and semipolar GaN", *10th International Conference on Nitride Semiconductors, ICNS*, Washington, D.C., USA, Aug. 2013.

[39] Y. Han, M. Caliebe, T. Meisch, M. Pristovsek, M. Kappers, F. Scholz, and C. Humphreys, "Structural characterisation of semi-polar GaN templates grown on prestructures r-plane sapphire substrates", poster at *15th European Workshop on Metalorganic Vapour Phase Epitaxy, EWMOVPE XV*, Aachen, Germany, June 2013.

[40] C. Hein, A. Kraus, H. Bremers, U. Rossow, K. Forghani, F. Scholz, and A. Hangleiter, "MBE growth and characterization of AlN and $Al_xGa_{1-x}N$ with various x", *DPG Spring Meeting*, Regensburg, Germany, Mar. 2013.

[41] M. Hocker, I. Tischer, K. Thonke, J. Wang, R.A.R. Leute, F. Scholz, J. Biskupek, W. van Mierlo, and U. Kaiser, "Enhanced stacking fault induced indium diffusion on semipolar gallium nitride based ridges", *DPG Spring Meeting*, Regensburg, Germany, Mar. 2013.

[42] M. Lohr, R. Schregle, I. Pietzonka, M. Strassburg, R.A.R. Leute, F. Scholz, K. Müller, A. Rosenauer, and J. Zweck, "Quantification of internal electric fields in InGaN/GaN quantum wells by differential phase contrast microscopy", poster at *DPG Spring Meeting*, Regensburg, Germany, Mar. 2013.

[43] S. Metzner, F. Bertram, T. Hempel, T. Meisch, S. Schwaiger, F. Scholz, and J. Christen, "Correlation of microscopic optical properties and defect structures of semipolar GaN on pre-patterned sapphire substrates by cathodoluminescence", *DPG Spring Meeting*, Regensburg, Germany, Mar. 2013.

[44] A. Molitor, P. Debernardi, S. Hartmann, R. Michalzik, and W. Elsäßer, "Spatially resolved Stokes parameters of small-area vertical-cavity surface-emitting lasers", *European Semiconductor Laser Workshop*, Bristol, United Kingdom, Sept. 2013.

[45] N. Passilly, R. Boudot, R. Chutani, C. Gorecki, A. Al-Samaneh, D. Wahl, and R. Michalzik, "Developments of miniature atomic clocks based on coherent population trapping, VCSELs and MEMS: technology of fabrication and laser source requirements", *2nd European Workshop on VeCSELs*, Montpellier, France, Oct. 2013.

[46] L. Schade, T. Wernicke, K. Forghani, J. Rass, S. Ploch, L. Kirste, M. Weyers, M. Kneissl, F. Scholz, and U. Schwarz, "Defects of polar, semipolar and nonpolar (In)GaN – a comparison", *DPG Spring Meeting*, Regensburg, Germany, Mar. 2013.

[47] I. Tischer, M. Hocker, M. Frey, R.A.R. Leute, F. Scholz, W. van Mierlo, J. Biskupek, U. Kaiser, and K. Thonke, "Investigation of defect related luminescence features in semipolar AlGaN layers on GaN", poster at *DPG Spring Meeting*, Regensburg, Germany, Mar. 2013.

[48] K. Thonke, I. Tischer, M. Hocker, M. Frey, and F. Scholz, "Identification of defects in semipolar GaN and (Al,Ga,In) by cathodoluminescence spectroscopy" (invited), *DPG Spring Meeting*, Regensburg, Germany, Mar. 2013.

Publications

[1] A. Bergmann, A. Hein, and R. Michalzik, "Vertical-cavity surface-emitting laser arrays for miniaturized integrated optical lattice modules", in Online Digest *Conf. on Lasers and Electro-Optics Europe, CLEO/Europe 2013*, paper CB-8.6-THU, one page. Munich, Germany, May 2013.

[2] A. Bergmann, J.A. Martos Calahorro, A. Hein, D. Wahl, and R. Michalzik, "Miniaturized sorting by optical lattices based on integrated vertical-cavity laser diodes", in Proc. (CD ROM) *2nd EOS Conference on Optofluidics, EOSOF 2013*, paper 1569714187, two pages. Munich, Germany, May 2013.

[3] M. Caliebe, T. Meisch, B. Neuschl, S. Bauer, J. Helbing, D. Beck, K. Thonke, M. Klein, D. Heinz, and F. Scholz, "Improvements of MOVPE grown $(11\bar{2}2)$ oriented GaN on pre-structured sapphire substrates using a SiN_x interlayer and HVPE overgrowth", *Phys. Status Solidi C*, 2013, DOI: 10.1002/pssc.201300527.

[4] M. Fikry, Z. Ren, M. Madel, I. Tischer, K. Thonke, and F. Scholz, "Coaxial InGaN epitaxy around GaN micro-tubes: tracing the signs", *J. Cryst. Growth*, vol. 370, pp. 319–322, 2013.

[5] A. Gadallah and R. Michalzik, "Densely packed 2-D matrix-addressable vertical-cavity surface-emitting laser arrays", in L.M. El Nadi (Ed.), *Modern Trends in Physics Research*, pp. 197–202. World Scientific Publishing Co., Conference Proceedings, vol. 9910, 2013, DOI: 10.1142/9789814504898_0029.

[6] A. Hein, S. Menzel, A. Ziegler, R. Rösch, and P. Unger, "Frequency doubled high-power semiconductor disk lasers for stereo projection and ion traps", Proc. SPIE, vol. 8847, pp. 88470J-1–8, 2013.

[7] D. Heinz, R. Leute, S. Kizir, Y. Li, T. Meisch, K. Thonke, and F. Scholz, "Ga(In)N photonic crystal light emitters with semipolar quantum wells", *Jpn. J. Appl. Phys.*, vol. 52, pp. 062101-1–5, 2013.

[8] A. Kern, A. Al-Samaneh, D. Wahl, and R. Michalzik, "Monolithic VCSEL–PIN photodiode integration for bidirectional optical data transmission", *IEEE J. Select. Topics Quantum Electron.*, vol. 19, 6100313, 13 pages, 2013.

[9] N.I. Khan, A. Bergmann, and R. Michalzik, "Fabrication of integration-capable surface-relief VCSEL arrays for miniaturized optical manipulation of microparticles", in Proc. *2nd Int. Conf. on Advances in Electr. Engin., ICAEE*, pp. 368–373. Dhaka, Bangladesh, Dec. 2013.

[10] M. Klein and F. Scholz, "Molybdenum as local growth inhibitor in ammonia based epitaxy processes", *Phys. Status Solidi C*, vol. 10, pp. 396–399, 2013.

[11] R.A.R. Leute, T. Meisch, J. Wang, J. Biskupek, U. Kaiser, M. Müller, P. Veit, F. Bertram, J. Christen, and F. Scholz, "GaN laser structure with semipolar quantum

wells and embedded nanostripes", in Proc. *10th Conf. on Lasers and Electro-Optics Pacific Rim (CLEO-PR)*, paper WH3-4, 2 pages, June 2013.

[12] R.A.R. Leute, D. Heinz, J. Wang, F. Lipski, T. Meisch, K. Thonke, J. Thalmair, J. Zweck, and F. Scholz, "GaN based LEDs with semipolar QWs employing embedded sub-micrometer sized selectively grown 3D structures", *J. Cryst. Growth*, vol. 370, pp. 101–104, 2013.

[13] M.J. Miah, A. Al-Samaneh, D. Wahl, and R. Michalzik, "Dynamic characteristics of inverted grating relief VCSELs for Cs-based microscale atomic clocks", in Online Digest *Conf. on Lasers and Electro-Optics Europe, CLEO/Europe 2013*, paper CB-8.4-THU, one page. Munich, Germany, May 2013.

[14] M.J. Miah, A. Al-Samaneh, A. Kern, D. Wahl, P. Debernardi, and R. Michalzik, "Fabrication and characterization of low-threshold polarization-stable VCSELs for Cs-based miniaturized atomic clocks", *IEEE J. Select. Topics Quantum Electron.*, vol. 19, 1701410, 10 pages, 2013 (error in the caption of Fig. 6: 20°C must be 80°C).

[15] R. Michalzik (Ed.), *VCSELs — Fundamentals, Technology and Applications of Vertical-Cavity Surface-Emitting Lasers*, Springer Series in Optical Sciences, vol. 166. Berlin: Springer-Verlag, 2013.

[16] R. Michalzik, "VCSELs: A Research Review", Chap. 1 in *VCSELs — Fundamentals, Technology and Applications of Vertical-Cavity Surface-Emitting Lasers*, R. Michalzik (Ed.), Springer Series in Optical Sciences, vol. 166, pp. 3–18. Berlin: Springer-Verlag, 2013.

[17] R. Michalzik, "VCSEL Fundamentals", Chap. 2 in *VCSELs — Fundamentals, Technology and Applications of Vertical-Cavity Surface-Emitting Lasers*, R. Michalzik (Ed.), Springer Series in Optical Sciences, vol. 166, pp. 19–75. Berlin: Springer-Verlag, 2013.

[18] R. Michalzik and T. Mappes, "Microfluidic integrated system for marker-free cell analysis and sorting" (in German), *Photonics BW Newsletter*, no. 1, pp. 14–17, June 2013.

[19] J.M. Ostermann and R. Michalzik, "Polarization Control of VCSELs", Chap. 5 in *VCSELs — Fundamentals, Technology and Applications of Vertical-Cavity Surface-Emitting Lasers*, R. Michalzik (Ed.), Springer Series in Optical Sciences, vol. 166, pp. 147–179. Berlin: Springer-Verlag, 2013.

[20] H. Roscher and R. Michalzik, "Fabrication-efficient flip-chip-bondable 850-nm VCSELs with an X-shaped vertical cavity", *IEEE J. Select. Topics Quantum Electron.*, vol. 19, 1700810, 10 pages, 2013.

[21] F. Scholz, K. Forghani, M. Klein, O. Klein, U. Kaiser, B. Neuschl, I. Tischer, M. Feneberg, K. Thonke, S. Lazarev, S. Bauer, and T. Baumbach, "Studies on defect reduction in AlGaN hetero-structures", *Jpn. J. Appl. Phys.*, vol. 52, pp. 08JJ07-1–4, 2013.

[22] P. Unger, A. Hein, F. Demaria, S. Menzel, M. Rampp, and A. Ziegler "Design of high-efficiency semiconductor disk lasers", Proc. SPIE, vol. 8606, pp. 860602-1–8, 2013.

[23] J. Wang, D. Zhang, R. Leute, T. Meisch, D. Heinz, I. Tischer, M. Hocker, K. Thonke, and F. Scholz, "InGaN/GaN based semipolar green converters", *J. Cryst. Growth*, vol. 370, pp. 120–123, 2013.

[24] P. Debernardi, W. Schwarz, and R. Michalzik, "Optical modal features of a VECSEL-based optofluidic device for microparticle sensing", *IEEE J. Quantum Electron.*, vol. 49, pp. 301–308, 2013.

[25] F. Gruet, A. Al-Samaneh, E. Kroemer, L. Bimboes, D. Miletic, C. Affolderbach, D. Wahl, R. Boudot, G. Mileti, and R. Michalzik, "Metrological characterization of custom-designed 894.6 nm VCSELs for miniature atomic clocks", *Opt. Express*, vol. 21, pp. 5781–5792, 2013.

[26] S. Lazarev, M. Barchuk, S. Bauer, K. Forghani, V. Holý, F. Scholz, and T. Baumbach, "Study of threading dislocation density reduction in AlGaN epilayers by Monte Carlo simulation of high-resolution reciprocal-space maps of a two-layer system", *J. Appl. Cryst.*, vol. 46, pp. 120–127, 2013.

[27] S. Lazarev, S. Bauer, K. Forghani, M. Barchuk, F. Scholz, and T. Baumbach, "High resolution synchroton X-ray studies of phase separation phenomena and the scaling law for the threading dislocation densities reduction in high quality AlGaN heterostructure", *J. Cryst. Growth*, vol. 370, pp. 51–56, 2013.

[28] S. Lazarev, S. Bauer, T. Meisch, M. Bauer, I. Tischer, M. Barchuk, K. Thonke, T. Baumbach, V. Holy, and F. Scholz, "3D reciprocal space mapping of diffuse scattering for the study of stacking faults in semipolar $(11\bar{2}2)$ GaN layers grown from the sidewall of an r-patterned sapphire substrate", *J. Appl. Cryst.*, vol. 46, pp. 1425–1433, 2013.

[29] N. Passilly, R. Boudot, R. Chutani, C. Gorecki, A. Al-Samaneh, D. Wahl, and R. Michalzik, "Developments of miniature atomic clocks based on coherent population trapping, VCSELs and MEMS: technology of fabrication and laser source requirements", in Proc. *2nd European Workshop on VeCSELs*, p. 51. Montpellier, France, Oct. 2013.

[30] T. Passow, R. Gutt, M. Kunzer, W. Pletschen, L. Kirste, K. Forghani, F. Scholz, K. Köhler, and J. Wagner, "High power efficiency AlGaN-based ultraviolet light-emitting diodes", *Jpn. J. Appl. Phys.*, vol. 52, pp. 08JG16-1–4, 2013.

[31] C. Pietzka, J. Scharpf, M. Fikry, D. Heinz, K. Forghani, T. Meisch, T. Diemant, R.J. Behm, J. Bernhard, J. Biskupek, U. Kaiser, F. Scholz, and E. Kohn, "Analysis of diamond surface channel field-effect transistors with AlN passivation layers", *J. Appl. Phys.*, vol. 114, pp. 114503-1–5, 2013.

[32] I. Tischer, M. Hocker, M. Fikry, M. Madel, M. Schied, Z. Ren, F. Scholz, and K. Thonke, "Optical properties of ZnO/GaN/InGaN core-shell nanorods", *Jpn. J. Appl. Phys.*, vol. 52, pp. 075201-1–5, 2013.

Ulm University | Institute of Optoelectronics | Annual Report 2013

ulm university universität ulm

Ulm University
Institute of Optoelectronics
Albert-Einstein-Allee 45
89081 Ulm | Germany